1-30-2013

Terrestrial and extraterrestrial radiation sources that move faster than light

Andrea Caroline Schmidt Zweifel

Andrea Caroline Schmidt Zweifel

Candidate

Mathematics

Department

This thesis is approved, and it is acceptable in quality and form for publication:

Approved by the Thesis Committee:

Prof. Terry Loring , Chairperson

Prof. Jens Lorenz

Dr. Klaus Heinemann

Terrestrial and Extraterrestrial Radiation Sources that Move Faster than Light

by

Andrea Caroline Schmidt Zweifel

B.S., Mathematics, University of New Mexico, 2006

THESIS

Submitted in Partial Fulfillment of the

Requirements for the Degree of

Master of Science
Mathematics

The University of New Mexico

Albuquerque, New Mexico

December, 2012

Dedication

This work is dedicated to my children, Marie and Richard, without whose loyalty, support and unwavering belief in my strength and persistence I might not have arrived at my destination.

The works of the Lord are great, sought out of all them that have pleasure therein. (Psalm 111)

Acknowledgments

I would like to thank my mentor and supervisor at Los Alamos National Laboratory, Dr. John Singleton, who has supported me for many years with his kindness, patience and wisdom, whilst always allowing me to choose my own path. Without his inspiration and innate enthusiasm for our research I would not have hurdled the obstacles in the completion of this work. I will always be deeply grateful for all that he has taught and given me.

My heartfelt thanks go to the distinguished faculty members who served on my thesis commitee: Professors Terry Loring and Jens Lorenz and Dr. Klaus Heinemann. As commitee chair, Prof. Loring stepped in and provided guidance and encouragement during a difficult time. I much appreciate his patience, humor and professional, as well as emotional, support. Dr. Klaus Heinemann generously shared his extensive knowledge of Mathematical Physics, contributing paragraphs to Chapters 3 and 5 while insisting on – much needed – mathematical rigor. Prof. Lorenz, who graciously agreed to join the committee on very short notice, provided valuable comments and advice.

In my daily work I have been blessed with a group of friendly, cheerful and outstandingly knowledgable colleagues. Special thanks to Joe Fasel for his mentorship, advice and insistence on sound programing habits, and to John Middleditch for teaching me the way of the stars. Collective and individual acknowledgements are also due to my external collaborators Houshang and Arzhang Ardavan and my coworkers at UNM and Los Alamos National Laboratory, David Bizzozero, Frank Krawczyk, Quinn Marksteiner, Bill Romero, Pinaki Sengupta, Tony Tomei and James Wigger. I stand on the shoulders of giants and it is their invaluable advice and expertise that has made this research possible.

Special thanks to my parents and my brother Martin and his family for their good-natured forbearance with the long process of researching and writing this work, and for their pride in the finished product. And to Jürgen, who was, for many years, my travelling companion on this journey, and who remains a friend and confidant. I am also deeply grateful to my friends, Janine Tulenko and Ted Mockler, who aided this work by offering advice, providing meals and watching my children. Better friends cannot be found. Lastly, I offer my regards and blessings to all those who supported me in any way during the completion of this work.

Terrestrial and Extraterrestrial Radiation Sources that Move Faster than Light

by

Andrea Caroline Schmidt Zweifel

B.S., Mathematics, University of New Mexico, 2006

M.S., Mathematics, University of New Mexico, 2012

Abstract

Maxwell's equations establish that patterns of electric charges and currents can be animated to travel faster than the speed of light *in vacuo* and that these superluminal distribution patterns emit tightly focused packets of electromagnetic radiation that are fundamentally different from the emissions by previously known terrestrial radiation sources. Novel antennae that employ extended distributions of polarization currents moving faster than light have proven to be effective emitters of electromagnetic radiation and are currently tested for applications in radar and low-power, secure communications technologies.

Here, we we study the emission of a localized charge in constant superluminal rotation. We set out by applying basic methods introduced by Huyghens and Fresnel to gain phase information and find that radiation sources that travel not only faster than light, but are also subject to acceleration, possess a two-sheeted envelope and a cusp – a region of intense concentration of energy. Moreover, careful analysis of the relationship between emission and observation time reveals that this need not be monotonic and one-to-one, as multiple retarded times – or even extended periods of

source time – can contribute to a single instant of reception. Finding solutions to this unusual temporal relation enables us to "measure" the intriguing electromagnetic effects that occur on the cusp and within the envelope of the emitted wave fronts quantitatively. Finally, we proceed to calculate the more sophisticated electromagnetic potentials and fields for these locations, thereby introducing amplitude in addition to phase information. Since integral solutions to Maxwell's equations, traditionally used in the context of stationary or subluminally moving sources, may be problematic when applied to faster-than-light charges due to the presence of multiple or extended retarded times, we will derive and visualize what constitutes the main, substantive part of the present work: The correct *formulae* for the Liénard-Wiechert potentials and fields of a point charge travelling arbitrarily fast along a given trajectory.

Numerical evaluation of these expressions shows that this radiation field has the following intrinsic characteristics: (i) it is sharply focused along a rigidly rotating spiral-shaped beam that embodies the cusp of the envelope of the emitted wave fronts, (ii) it consists of either one or three concurrent polarization modes (depending on the relative positions of the observer and the cusp) that constitute contributions to the field from differing retarded times, (iii) it is highly elliptically polarized, (iv) the position angle of each of its linearly polarized modes swings across the beam by as much as 180^o, and (v) the position angles of two of its modes remain approximately orthogonal throughout their excursion across the beam.

In an appendix, we compare these findings to the radiation emitted by pulsars, rapidly rotating, highly magnetized neutron stars, and find that virtually all of the enigmatic features of pulsar radiation - the polarization properties, image structure, apparent radiation temperature and peak spectral frequencies - can be explained using a single, elegant model with few input parameters and no external assumptions. Hence, superluminal emission is almost certainly not only a human artifact, but an

important and likely ubiquitous process in the observable universe that may represent significant amendments to standard models of many astronomical objects.

Most calculations in Chapters 4, 5 and the Appendix are of a formal nature only. Rigor can, however, be achieved rather easily in future studies by means of the theory of distributions as outlined in the final part of Chapter 5.

Contents

Chapter 1

Sources that Travel Faster than their Emitted Waves – An Introduction

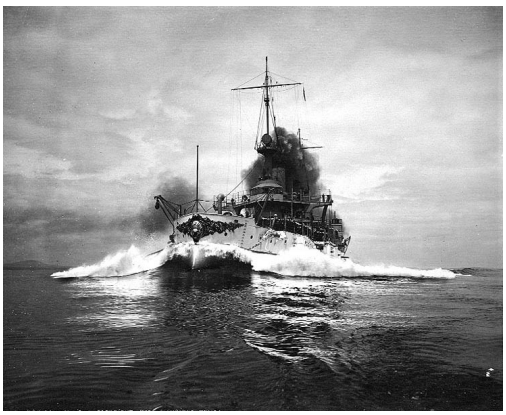

Figure 1.1: Bow wave of the USS Connecticut, on her speed trials in 1906 or 1907.

This thesis concerns sources of water, sound, and electromagnetic waves that move faster than the emitted waves themselves. We discuss the mathematical treatment of such sources, the unique features of their emission, and practical implementations and applications, on the Earth as well as in the universe.

1.1 Constant Motion

A source that moves uniformly through a homogeneous medium emits directed waves if the velocity of the source exceeds the speed of the waves themselves [1]. This general property of sources that travel faster than their own waves was likely first studied in hydrodynamics, since a ship that glides across the sea faster than the wave propagation speed – about $2.5 \times \sqrt{l}$ knots, where l is the waterline length of the vessel in meters [2] – excites easily observable directed surface waves (Fig. 1.1).

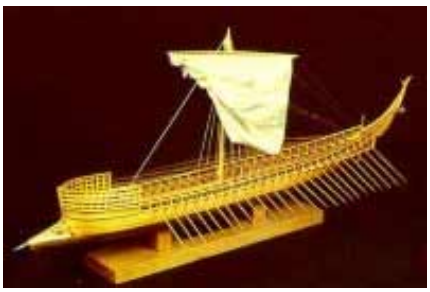

Figure 1.2: Model of a penteconter, a galley with one row of oars on each side.

That ancient seafaring nations were well aware of bow waves, wakes, and their effects on the speed of a boat, is evidenced by numerous historical accounts dating back as far as Homer's *Iliad*, whose written version is usually dated to around the eighth century BC:

> And Apollo, that worketh afar, sent them a favouring wind, and they set up the mast and spread the white sail. So the wind filled the belly of the sail, and the dark wave sang loudly about the stern of the ship, as she went, and she sped over the wave, accomplishing her way [3].

A ship travelling swiftly creates a bow wave which it has to climb, expending considerable energy which would be better spent to increase the vessel's speed. The longer a ship is, the faster it can travel before being hampered by this effect, but long ships were difficult to construct with the limited technology available [4]. Through a process of trial and error, the monoreme – a galley with one row of oars on each side – reached the peak of its development in the penteconter, about 38 meters long, with 25 oarsmen on each side. It is generally assumed that Odysseus' "black ship," the fastest military vessel of its day (Fig. 1.2), was a penteconter [4], whose swift journey

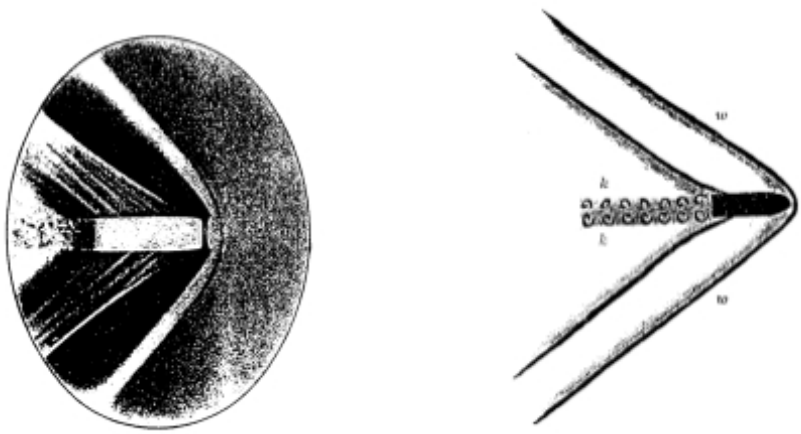

Figure 1.3: Left: Schlieren photograph by Ernst Mach depicting a projectile in supersonic flight. Right: Mach's schematic representation of the same projectile. *ww* denotes the bow wave, *kk* the wake with its turbulences [6].

"across the wine-dark" Ionian sea to the island of Ithaca is described in the *Odyssey*:

> And as upon a plain four harnessed stallions spring forward all together at the crack of whip, and lifting high their feet speed swiftly on their way; even so the ship's stern lifted, while in her wake followed a huge upheaving wave of the resounding sea [5].

It is perhaps not surprising that the Austrian physicist Ernst Mach (1838-1916) immediately recognized the similarity between the ballistic shock waves captured by his schlieren photographs [1] and the bow wave of a moving ship when he investigated the sound waves generated by a projectile moving through the air at supersonic speed (Fig. 1.3):

[1]Schlieren photography is a visual process that is used to photograph the flow of fluids of varying densites. The basic optical schlieren system uses light from a single collimated source shining on, or from behind, a target object. Variations in the refractive index caused by density gradients in the fluid distort the collimated light beam. The distortion creates a spatial variation in the intensity of the light, which can be visualized directly with a shadowgraph system.

> Wenn ich nicht sagen würde, was das Bild vorstellt, so könnten Sie wohl glauben, dass es das Bild ist eines rasch auf dem Wasser dahinfahrenden Bootes, aus der Vogelperspective aufgenommen. Vorn sehen Sie die Bugwelle ww, hinter dem Körper eine Erscheinung kk, welche dem Kielwasser mit seinen Wirbeln sehr ähnlich sieht. In der That ist der helle, hyperbelähnliche Bogen am Scheitel des Projectils eine Luftverdichtungswelle, die ganz analog ist der Bugwelle eines Schiffes, nur dass erstere keine Oberflächenwelle ist. Sie entsteht im Luftraume und umgibt das Projectil glockenförmig von allen Seiten [6]. [2]

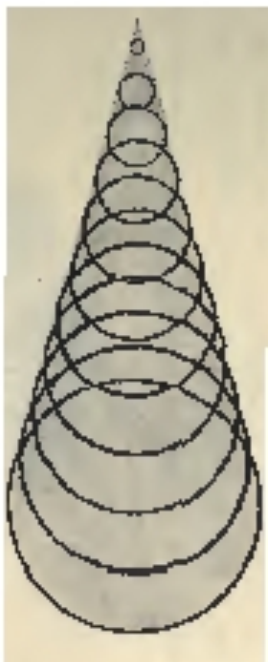

Figure 1.4: Sketch by Ernst Mach depicting Huyghens wavelets that combine to form the envelope of the "Mach cone" [6].

Ernst Mach, a polymath within science and, in his time, a leading authority in philosophy, physiology and physics, was the first to study projectiles in flight systematically, using various high speed diagnostic methods [7]. In collaboration with Peter Salcher (1848-1928), a professor of physics and mechanics at the Royal and Imperial Naval Academy at Fiume, he took successful photographs of projectiles travelling faster than sound, establishing that bow waves precede any body in supersonic motion. Letters exchanged weekly between Salcher and Mach reveal that the latter recognized the head wave at once as the envelope of disturbances originating from the projectile;

[2] "If I did not say what the picture represents you might believe it to be the picture of a boat that glides rapidly on the water, taken from bird's-eye view. In front the bow wave ww can be seen, behind the body an appearance kk that is rather similar to the wake with its turbulences. In fact, the light, hyperbola-shaped bow at the apex of the projectile is an air-compression wave, which is very analogous to the bow wave of a ship, just that the former is not a surface wave. It is formed in air space and surrounds the projectile like a bell from all sides."

a shock front created by a source that exceeds the speed of its own waves [8, 9].

> So wie nun ein langsam bewegtes Boot keine Bugwelle zeigt, und so wie diese erst dann auftritt, wenn das Boot sich mit einer Geschwindigkeit bewegt, die grösser ist als die Fortpflanzungsgeschwindigkeit der Wasserwellen, so kann man auch vor dem Projektil keine Verdichtungswelle sehen, so lange die Projektilgeschwindigkeit kleiner ist als die Fortpflanzungsgeschwindigkeit des Schalles. Erreicht und übersteigt aber die Projektilgeschwindigkeit diesen Wert, so nimmt die Kopfwelle, wie wir sie nennen wollen, zusehends an Mächtigkeit zu, und zugleich wird dieselbe immer gestreckter, d. h. der Winkel der Contouren der Welle mit der Flugrichtung wird immer kleiner, gerade so wie beim Wachsen der Bootgeschwindigkeit etwas Ähnliches geschieht. In der Tat kann man nach einem in der dargelegten Weise gewonnenen Momentbild die Projektilgeschwindigkeit ungefähr abschätzen [6]. [3]

In his compilation of public lectures, *Populärwissenschaftliche Vorlesungen*, Mach visualizes the sound waves emitted by a body in supersonic flight by using the Huyghens-Fresnel principle (Fig. 1.4), which recognizes that every point on a propagating wave front is a source of spherical waves in its own right. Huyghens wavelets, expanding with the velocity of sound c_S, are centered on successive positions of the body at chosen time intervals (Fig. 1.5 left). If the projectile moves faster than sound (Fig. 1.5 right), they represent a conical shock wave front with the line of flight as axis and half angle α given by $\sin\alpha = c_S/v = 1/M$, where v is the speed of the

[3] Just as a slowly moving boat does not show a bow wave, and just as this wave only manifests itself when the boat moves at a velocity greater than the propagation speed of water waves, one cannot see a compression wave ahead of the projectile as long as the velocity of the projectile is less than the propagation speed of sound. If the speed of the projectile reaches or exceeds this value, however, the head wave, as we like to call it, increases steadily in magnitude, and, at the same time, is elongated, which is to say that the angle of the contours of the wave with the flight path decreases, just as something similar happens when the speed of the boat increases. In fact, from a picture taken in the manner described above, one is able to roughly estimate the speed of the projectile.

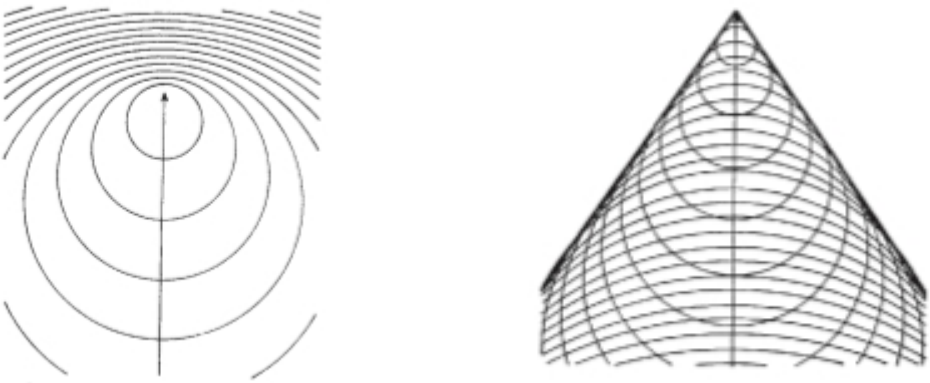

Figure 1.5: Left: Huyghen's wavelets emitted by a source moving along a rectilinear path with constant subsonic speed, $M = 0.8$. Since the source is moving, the center of each new wavefront is slightly displaced to the top. As a result, the wavefronts begin to "bunch up" ahead of the source and are spread further apart behind it. This is known as the "Doppler effect," first explained in 1842 by Christian Doppler. Right: The same source moving with constant supersonic speed, $M = 1.6$. Since the source is moving faster than the sound waves it creates, it leads the advancing wavefront and will pass by a stationary observer before he hears the sound it creates. Notice the formation of the Mach cone, the angle of which depends on the ratio of source speed to sound speed alone. [10]

object and M a dimensionless constant named "Mach number" in honor of Ernst Mach [9].

Mach's discovery of the bow shock that precedes a projectile in supersonic flight did not only lay the foundation for modern aerodynamics, but also shed light on two unsolved ballistics problems of the day [9]. During the Franco-Prussian war of 1870-1871, it was found that the new French Chassepôt high-speed bullets caused big crater-shaped wounds. The French were suspected of using explosive projectiles and, therefore, of violating the International Treaty of Petersburg, which prohibited the use of explosive ammunition. Mach put an end to the controversy by giving the complete and correct explanation: The extensive injuries were, in fact, caused by the high-pressure air between the bullet's bow wave and the bullet itself.

Perhaps more importantly for our purposes, Mach's observations explained why artillerists could hear two bangs downrange from a marksman when high-speed projectiles were fired, but only one from low-speed bullets. It was realized that, in

addition to the explosion from the muzzle, an observer downrange would experience the arrival of a shock wave front. The precise nature of this "sonic boom," however, was not thoroughly investigated until the early 1950's and the testing of the first supersonic airplanes.[4]

Although sources that travel faster than their emitted waves have been studied extensively in hydrodynamics and acoustics, the same cannot be said for electrodynamics, where the publication of Einstein's special theory of relativity [11] put an abrupt end to early research. Scientific investigation of the electromagnetic field generated by a charged particle that moves faster than light began with a largely ignored article by physicist and mathematician Oliver Heaviside in 1887 [12] and is the subject of of several papers written by Sommerfeld in 1904 and early 1905 [13]. In his *Electrical Papers* [12], Heaviside describes the optical analogue to the "Mach cone" as follows:

> Returning to the case of a charge q at a point moving through a dielectric, if the speed of motion exceeds that of light, the disturbances are wholly

[4] On a historical note that may resonate with many scientists today, we add that Ernst Mach remained a life long socialist, advocate for the working class and peace activist [7]. It is unfortunate that his seminal research ultimately led to to the development of more refined weapons, an irony which was not lost on the eminent Austrian scientist. Hence he prefaces his lecture *Über Erscheinungen an fliegenden Projektilen* with the following words:

> Die Menschen fühlen sich heutzutage verpflichtet, zuweilen für recht fragwürdige Ziele und Ideale sich gegenseitig in kürzester Zeit möglichst viele Löcher in den Leib zu schiessen. Und ein anderes Ideal, welches zu den vorgenannten meist in schärfstem Gegensatze steht, gebietet ihnen zugleich, diese Löcher von kleinstem Kaliber herzustellen, und die hergestellten möglichst rasch wieder zu stopfen und zu heilen [6].
>
> (Humans nowadays feel compelled, sometimes for rather dubious goals and ideals, to shoot, within the shortest time, as many holes into each other's body as possible. And another ideal, which is most often in stark contrast to the one previously mentioned, demands that they simulataneously produce these holes with the smallest caliber possible, and to mend and heal the ones produced as swiftly as possible.)

> left behind the charge, and are confined within a cone, AqB. The charge is at the apex, moving from left to right along Cq. The semi-angle, θ, of the cone, or the angle AqC, is given by $\sin\theta = c/u$, where c is the speed of light, and u that of the charge [12]. [5]

The publication of the special theory of relativity in June 1905 [11], however, discouraged further work as one of its tenets is, of course, that any known particle that has a charge also has a rest mass and is so barred from moving faster than light. Moreover, no source that moves faster than the wave speed can be pointlike, for this results in magnetic fields of infinite strength [6] on the envelope of the emitted wave fronts [14].

However, while relativity holds that the speed of light *in vacuo* is a universal constant (c), the speed at which electromagnetic waves propagate in a material may be significantly less: In water, for instance, they move at a mere $0.75c$ [15]. Whenever the velocity $v = \beta c$ of a charged particle, most commonly an electron, exceeds c/n, where n is the refractive index of the medium and β denotes, analogous to the Mach number, the dimensionless entity v/c, this particle emits Čerenkov radiation [15], so named after its discoverer Pavel Alekseyevich Čerenkov (1904-1990).

In 1934, while working under S. I. Vavilov, Čerenkov observed bright ciruleanblue light emanating from a bottle of water that was subject to radioactive bombardment [16]; a discovery which proved to be of great consequence for subsequent

[5] The original document denotes the speed of light as v rather than the customary constant c. The denomination c, for the latin *celeritas* – swiftness – was first introduced in 1856, when Wilhelm Eduard Weber and Rudolf Kohlrausch used it for a constant later shown to equal $\sqrt{2}$ times the speed of light *in vacuo*. In 1894 Paul Drude redefined c, giving it its modern meaning. Einstein used V in his original German-language papers on special relativity in 1905, but in 1907 he switched to c, which by then had become the standard symbol.

[6] As will be shown in coming sections, it is mathematically more accurate to describe the strength of the magnetic fields on the envelope as "undefined" rather than "infinite."

experimental work in nuclear physics and the study of various cosmic phenomena [15].

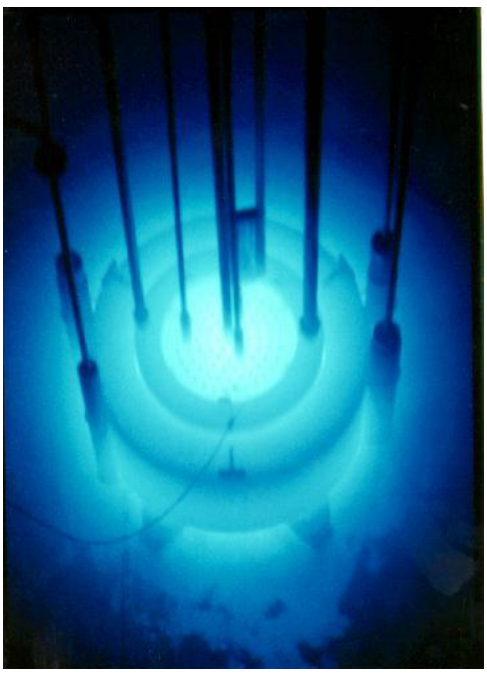

Figure 1.6: Blue Čerenkov light emanating from the reactor of a nuclear power plant.

As the Huyghens constructions of Figure 1.7 show, Čerenkov radiation is very similar in nature to the generation of a bow wave: Radiation emitted by an excited atom S travelling along the x-axis will form a coherent wavefront – the Čerenkov envelope – at a specific angle [15]. This caustic constitutes the surface of of a cone whose axis coincides with the particle's trajectory and whose aperture is given by

$$\theta = \cos^{-1}\frac{\left(\frac{c}{n}t\right)}{\beta ct} = \cos^{-1}\frac{1}{\beta n}, \quad \beta > \frac{1}{n}; \quad (1.1)$$

hence, the higher the source speed, the narrower the cone. For a "true" superluminal source, *e.g.,* a source of electromagnetic radiation that is moving faster than the speed of light *in vacuo*, thereby giving rise to so-called "vacuum Čerenkov radiation," expression (1.1) reduces to $\theta = \cos^{-1}(1/\beta)$ since $n = 1$. [7]

Moreover, Figure 1.7 illustrates a general and rather remarkable aspect of radiation emitted by sources that exceed their own wave speed: The relation between retarded (source) and reception times need not be monotonic and one-to-one. Multiple retarded times can contribute to a single instant of reception, which is to say that several wave fronts with differing emission times can pass through a single observation point simultaneously. An observer situated outside the Čerenkov envelope cannot see the source since none of the advancing waves have reached him yet, whereas one

[7] The first demonstration that our faster-than-light technology demonstrators function as true superluminal sources involved the detection of vacuum Čerenkov radiation emitted at an angle that depends on the speed of the source alone (Fig. 1.12) [17, 18].

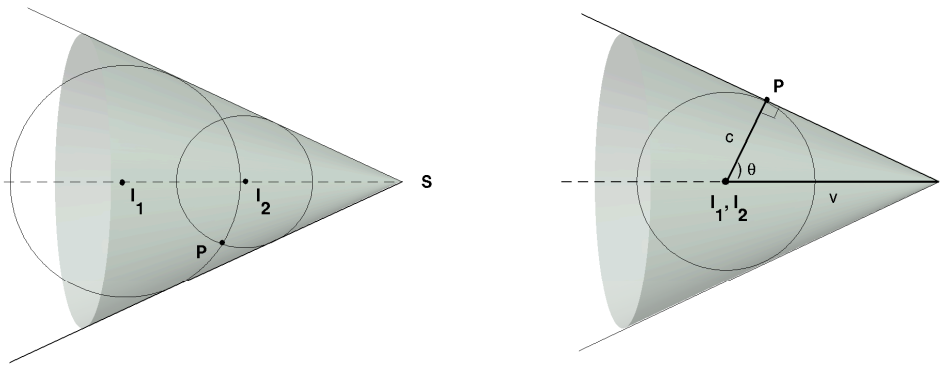

Figure 1.7: Huyghens wavelets (light curves) and their envelope for a superluminal source moving at a constant velocity along a rectilinear trajectory. Left: An observer (P) inside the Čerenkov envelope samples two images of the source (I_1, I_2), one to his left and one to his right. Right: On the envelope of the wave fronts, two contributions from the source's history coalesce and an observer will see one image of the source only. Nothing is seen outside the envelope.

within it samples two distinct images from the source's history (Fig. 1.7 left). [8] On the envelope of the wavefronts two contributions from the source's history coalesce and one sole image is received (Fig. 1.7 right).

[8] Readers of a sci-fi bent will be amused to learn that this effect is known as the "Picard Maneuver" among followers of the American television series "Star Trek" and denotes a battle tactic invented by Starfleet Captain Jean-Luc Picard. In 2355, Picard was in command of the USS Stargazer when it was attacked by an unknown alien vessel, later determined to be of Ferengi origin. During the engagement which came to be known as the "Battle of Maxia," the Stargazer, which was holding station several million kilometers away from its adversary, suddenly accelerated to warp 9 (1516 times the speed of light) directly towards the Ferengi ship. Because the enemy vessel was only equipped with light speed sensors, the ship's crew had no way of knowing that the Stargazer had changed position until it was too late. When the light from the moved vessel reached the Ferengi ship's sensors, wavefronts from its previous position were still arriving and, alas, the Ferengi saw two images of the Stargazer concurrently. The Picard Maneuver later became required reading at Starfleet Academy.

1.2 On Acceleration and "Sonic Booms"

On October 14, 1947 engineers on the ground at Muroc field in the Mojave desert heard test pilot Chuck Yeager drawl deadpan on the radio, "Say, Ridley... make another note, will ya? ...there's somethin' wrong with this ol' machometer ..." (faint chuckle) "...it's gone kinda screwy on me..." – code that the famed pilot had "broken the sound barrier" and his aeroplane – an X-1 built by the Bell Aircraft Corporation under an Army contract – had gone supersonic [19]. And, at that very moment, a monumental "boom" rocked over the quonset-style hangars and the single concrete runway, just as predicted by physicists and aeronautics engineers many years before. [9]

Ever since the end of the second world war, the American and British Air Forces had engaged in a furious race to achieve Mach 1 first; however, pilots reported that the controls would lock or "freeze" or even alter their normal function [19] when their 'planes approached the speed of sound in dives . In 1946, Geoffrey de Havilland, son of the famous British aircraft designer and builder, tried to take one of his father's DH 108 Swallows supersonic. The plane started buffeting and then disintegrated, killing the pilot and leading aeronautics engineers to speculate that the shock waves became so severe and unpredictable that no aircraft could withstand them. Talk about "the sonic wall" and "the sound barrier" emerged, implying that

Figure 1.8: Chuck Yeager in front of his Bell X-1, named "Glamorous Glennis" in honor of his wife.

[9] In 1944, at the height of the Second World War, Theodore von Kármán, at the time an aerodynamicist at the California Institute of Technology in Pasadena, observed that when an entire aircraft, not just the air accelerating over the thickest part of the wing, went supersonic, shock waves would be sent to the ground. He theorized that people nearby would hear and feel the passing of that pressure pulse [20].

the speed of sound was a physical boundary, absolute and not to be "broken" or "pierced" by pilots.

On September 6, 1948, John Derry became – quite serendipitously – "the first Briton to pass the speed of sound and live to tell about it," [10] and while Yeager's tremendous achievment had become "a piece of thunder with no reverberation" due to the highly classified nature of the Air Force project, the "historic feat" of the "fine-looking" young British pilot immediately captured the immagination of the public and was rewarded with the "coveted R. Ae. C. Gold Medal." [11] As a result, entire families flocked to events such as Britain's annual Farnborough Air Show to witness novel airplanes dive through the sound barrier, generating shock waves that "sounded like cannon fire" and " – palpable as ocean breakers – crashed against the crowd's bodies and ears [21]."

It was not until these public demonstrations of the "sonic boom" that physicists began to engage in an open discussion of the acoustic phenomena that accompany the dive of an aircraft to attain supersonic speed. In a letter to *Nature*, T. Gold pointed out that a shock will reach a stationary observer when the wavelets emanating from successive elements of the path of the source (*e.g.,* the aircraft) superpose at the observer [23]. Hence a spectator will experience an earshattering thunderclap from every occasion on which the aircraft is travelling towards him at the speed of sound and with zero acceleration, which happens whenever $-\mathrm{d}r/\mathrm{d}t = c_S$, where r is the scalar (retarded) distance of the aircraft from the observer. P. Rothwell [24] added that in the case of a body which accelerates and then decelerates through the speed of sound, the shock wave departs radically from the single conical surface depicted

[10] It is widely believed that de Havilland passed Mach 1 before the remnants of his plane crashed into the Thames estuary [21].

[11] In a cruel twist of fate, John Derry died four years, to a day, after passing the speed of sound in what became known as "The Farnborough Tragedy." His plane, the first prototye de Havilland 110 supersonic fighter, disintegrated during the S.B.A.C. Show at Farnborough, killing the young pilot, his co-pilot and 29 spectators [22].

by Mach and becomes a two-sheeted meniscus symmetrical about the line of flight as shown in Figure 1.9. Here, the duration of supersonic flight is 16 seconds and the Mach numbers are shown at the respective positions of the body at second intervals. Using Huyghens constructs and schlieren photographs, G. M. Lilley *et al.* [10] showed that, for a source moving along a straight path at a speed which increases (Fig. 1.10 left) or increases and then decreases (Fig. 1.10 right) through the speed of sound, two curved wave fronts emerge, joined at their outer extremities by cusps. These wave bundles, which eventually move ahead of the retarded source as the aircraft slows down to subsonic speeds, cause loud bangs as they pass the observer.

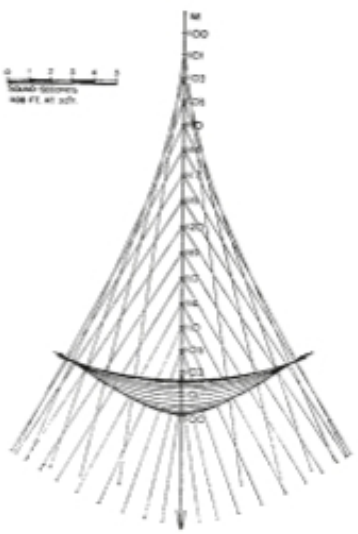

Figure 1.9: Shock wave formed by a body moving in a straight line at a speed which increases and then decreases through the speed of sound [24].

Meanwhile, eminent Hungarian physicist Theodore von Kármán [25] as well as Jakob Ackeret in Zürich [26] and Maurice Roy in Paris [27] suggested that the booms are due to the piling up of sound impulses – such as engine noise – emitted during the periods in which the flying body passes through the sound barrier. If the airplane is moving toward a stationary observer, these impulses will reach him over a shorter time span than that over which they were emitted. [12] Hence, extended periods of source time can contribute to a single instant of reception, which is to say that several wave fronts with differing emission times can pass through a distant observation point simultaneously. This is known as *tem-*

[12] This becomes evident if one considers that all sound emitted from a source moving exactly with sound velocity straight toward the observer would reach the latter in one short moment; namely when the sound source arrived at the location of the observer. The reason is that sound and sound source would be travelling at the same speed.

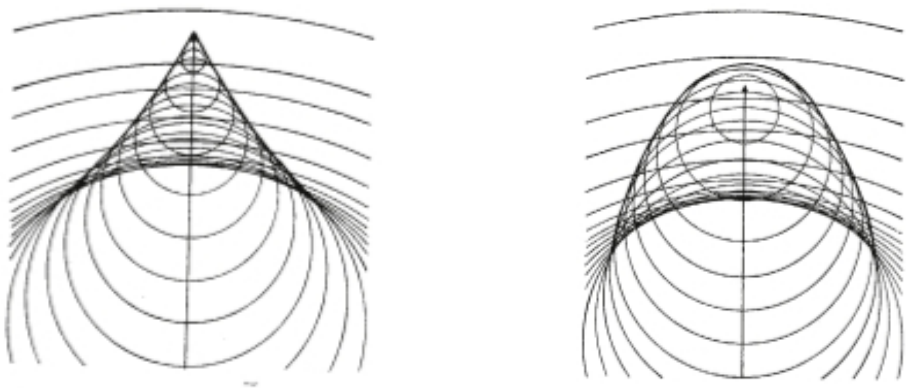

Figure 1.10: Left: Huygen's wavelets emitted by a source accelerating along a straight line from subsonic to supersonic speed. Right: The same source accelerating from subsonic to supersonic speed and then retarding to subsonic speed [10].

poral focusing or focusing in time, *i.e.,* the concentration of energy carried by the waves in the time domain. In other words, in the aircraft's frame of reference, low energy sound is excited over an extended time frame, all of which arrives at a distant location instantaneously, creating a large and concentrated "boom." As a former Concorde pilot puts it, "You don't actually hear anything on board. All we see is the pressure wave moving down the aeroplane – it gives an indication on the instruments. And that's what we see of Mach 1. But we don't hear the sonic boom or anything like that. That's rather like the wake of a ship – it's behind us [28]."

1.3 Faster than Light

It was not until the early 1970s that eminent Soviet physicists B. M. Bolotovskii and V. L. Ginzburg [14, 29] pointed out that, while special relativity precludes massive particles from moving faster than light, patterns or disturbances caused by the relative motion of individual charged particles – *e.g.,* polarization currents – are not restricted to subluminal speeds. Polarization **P**, formally defined as the dipole mo-

ment per unit volume, results from the displacement of positive and negative charges in opposite directions. A polarization current occurs when a polarized region moves or changes with time t. As will be shown below, the polarization current density is $\partial\mathbf{P}/\partial t$ and has the same dimensions as a conventional current density of electrons. The term was introduced by Maxwell as a correction to Ampère's equation of induction to ensure conservation of charge [30]. If polarization currents oscillate or accelerate, they will emit electromagnetic radiation, just as accelerated or oscillating currents of electrons do. However, unlike electrons, which possess rest mass and are therefore limited to speeds less than c, the speed of light, a polarization current may travel arbitrarily fast as the displacement of its constituent elements is minimal; while the radiation source travels faster than c, the individual massive particles' speeds are allowed to remain subluminal [17, 18, 31, 32].

1.3.1 Maxwell's Equations: A Tale of Two Fields

Maxwell's equations – named after the Scottish physicist and mathematician James Clerk Maxwell (1831-1879) – represent the most elegant and concise way to state the fundamentals of electricity and magnetism. They describe the electric and magnetic fields arising from varying distributions of electric charges and currents, and how those fields change with time. Maxwell's own contribution is just the last term of the last equation, but realizing the necessity of that term had dramatic consequences. It made evident for the first time that varying electric and magnetic fields could feed off each other and hence propagate indefinitely through space, far from the varying charges and currents where they originated. His new term (he called it the *displacement current*) freed the fields to move through space in a self-sustaining fashion, and even predicted their velocity, which is the speed of light [30, 33].

The four equations for the electric and magnetic field intensities $\mathbf{E}$ and $\mathbf{H}$ as well

as the electric displacement $\mathbf{D}$ and magnetic induction $\mathbf{B}$ are given by (SI units)

$$\nabla \cdot \mathbf{D} = \rho, \tag{1.2}$$

$$\nabla \cdot \mathbf{B} = 0, \tag{1.3}$$

$$\nabla \times \mathbf{E} = -\frac{\partial \mathbf{B}}{\partial t}, \tag{1.4}$$

$$\nabla \times \mathbf{H} = \mathbf{J} + \frac{\partial \mathbf{D}}{\partial t}, \tag{1.5}$$

where ρ and $\mathbf{J}$ denote the free electric charge density and free current density, respectively. In an insulating, uniform, isotropic medium they are zero while $\mathbf{B}$ and $\mathbf{H}$, and $\mathbf{D}$ and $\mathbf{E}$ are connected as follows:

$$\mathbf{B} = \mu \mathbf{H}, \tag{1.6}$$

$$\mathbf{D} = \varepsilon_0 \mathbf{E} + \mathbf{P} = \varepsilon \mathbf{E}. \tag{1.7}$$

Here, μ and ε – both constants [13] – are the magnetic permeability and electric permittivity, respectively; ε_0 is known as the permittivity of free space. (1.4) and (1.5) reduce to

$$\nabla \times \mathbf{E} = -\frac{\partial \mathbf{B}}{\partial t} = -\mu \frac{\partial \mathbf{H}}{\partial t}, \tag{1.8}$$

$$\nabla \times \mathbf{H} = \frac{\partial \mathbf{D}}{\partial t} = \varepsilon \frac{\partial \mathbf{E}}{\partial t}. \tag{1.9}$$

Taking the curl on both sides of (1.4) and utilizing (1.6) gives

$$\nabla \times \nabla \times \mathbf{E} = \nabla(\nabla \cdot \mathbf{E}) - \nabla \cdot (\nabla \mathbf{E}) = -\nabla \times \frac{\partial \mathbf{B}}{\partial t} \tag{1.10}$$

$$\equiv -\frac{\partial}{\partial t}(\nabla \times \mathbf{B}) \tag{1.11}$$

$$\equiv -\mu \frac{\partial}{\partial t}(\nabla \times \mathbf{H}) \tag{1.12}$$

We take the partial derivative with respect to time on both sides of (1.9), which gives

$$\frac{\partial}{\partial t}(\nabla \times \mathbf{H}) = \varepsilon \frac{\partial^2}{\partial t^2} \mathbf{E}, \tag{1.13}$$

[13] In an inhomogeneous, non-isotropic medium, μ and ϵ will be position-dependent tensors.

and, combining (1.12) and (1.13), find that

$$\nabla(\nabla \cdot \mathbf{E}) - \nabla \cdot (\nabla \mathbf{E}) = -\mu\varepsilon \frac{\partial^2}{\partial t^2}\mathbf{E}. \tag{1.14}$$

Hence,

$$\nabla^2 \mathbf{E} - \mu\varepsilon \frac{\partial^2}{\partial t^2}\mathbf{E} - \nabla(\nabla \cdot \mathbf{E}) = 0. \tag{1.15}$$

Since $\nabla \cdot \mathbf{D} = \nabla \cdot \varepsilon \mathbf{E} = 0$ (1.7) when $\rho = 0$ (1.2), this results in the three dimensional wave equation[14]

$$\nabla^2 \mathbf{E} - \mu\varepsilon \frac{\partial^2}{\partial t^2}\mathbf{E} = 0 \tag{1.16}$$

This shows that the electic field $\mathbf{E}$ propagates with wavelike motion and velocity $v = (\varepsilon\mu)^{-1/2}$. A similar method can be used to show that

$$\nabla^2 \mathbf{H} - \mu\varepsilon \frac{\partial^2}{\partial t^2}\mathbf{H} = 0. \tag{1.17}$$

In a vacuum, $\varepsilon \to \varepsilon_0$ and $\mu \to \mu_0$, the permittivity and permeability of free space, leading to $c = (\varepsilon_0\mu_0)^{-1/2}$. This latter result enabled Maxwell to relate the units of magnetism and electrostatics and show the true nature of electromagnetic radiation.

1.3.2 Ampère's Missing Term

As shown above, a polarization current can be described by Maxwell's IV equation (1.5)

$$\nabla \times \mathbf{H} = \mathbf{J} + \frac{\partial \mathbf{D}}{\partial t},$$

where the displacement field $\mathbf{D}$ is defined as

$$\mathbf{D} = \varepsilon_0 \mathbf{E} + \mathbf{P}$$

[14] (1.16) and (1.17) are often refered to as the "electromagnetic wave equations" in textbooks and the pertinent literature.

(1.7). We note that (1.5) is invariant under Lorentz transformations [33] and therefore relativistic. Taking the time derivative on both sides of (1.7) and substituting the resulting equation into (1.5) we find that

$$\nabla \times \mathbf{H} - \varepsilon_0 \frac{\partial \mathbf{E}}{\partial t} = \mathbf{J} + \frac{\partial \mathbf{P}}{\partial t}, \tag{1.18}$$

in which the polarization current $\partial \mathbf{P}/\partial t$ contributes to the fields in just the same way as the current $\mathbf{J}$ of free charges; however, as it is not carried by massive particles, it is not limited to subluminal speeds. Although capable of moving faster than light, such a source distribution does not violate special relativity as it cannot be used to transmit a signal superluminally; the emitted radiation (as any other) travels *at* the speed of light.

Figure 1.11: "The Mexican Wave" as it surges through a stadium.

Polarization currents may be compared to the "Mexican Wave," or *La Ola* (Fig. 1.11), which surges through the rows of spectators in a stadium as those in one section leap to their feet with their arms up, and then sit down again as the next section rises to repeat the motion [34]. An observer will see a wave of standing spectators that travels rapidly through the crowd, a rotating pattern whose speed is only limited by the accuracy of timing and whose constituent particles never move away from their seats.

As will be shown in subsequent sections, extended sources of electromagnetic radiation whose distribution patterns move faster than light *in vacuo* have been realized in the laboratory on numerous occasions. In experiments carried out in Russia, the United Kingdom, and the USA, polarization currents travelling at up to

20 times the speed of light (and, hence, "hyperluminally") have been shown to emit tightly-focused pulses of radiation [1, 14, 17, 18, 35–40].

Furthermore, as will be seen through the remainder of this work, and especially in Appendix A, superluminal polarization currents are almost certain to be responsible for the extreme properties of the electromagnetic radiation received from astronomical objects such as pulsars and magnetars (rapidly spinning, highly magnetized neutron stars), gamma-ray bursts (short-lived bursts of gamma-ray photons) and quasars (starlike objects that emit electromagnetic energy, including radio waves and visible light). Hence, as suggested by Bolotovskii and Ginzburg in 1972 [14], superluminal emission appeqars to be an important and ubiquitous process in the observable universe that may demand significant amendments to standard models of many astronomical objects.

1.4 Practical Superluminal Antennae

In 2003, John Singleton of the Physics Department of Oxford University, his postdoctoral student, Arzhang Ardavan, and Houshang Ardavan of the University of Cambridge, built the first man-made superluminal light source (Fig. 1.12 left). The device was based on the latter's theoretical work in pulsar astronomy and the acoustic phenomena effected by rotating helicopter blades and constitutes, in effect, the first ground-based simulation of a rotating neutron star. The 2-meter-long device was mounted on a scissor lift and tested on a runway at Turweston Aerodrome in Northhampton after airtraffic had shut down for the night. The construction of the "polarization synchrotron," as the machine was called, soon led to numerous articles in the scientific [41–49] and popular press, many of which were neither particularly flattering nor scientifically accurate. "Money Spinner or Loopy Idea?" Edwin Cartlidge asked, somewhat ominously, in *Science* [50], while Martin Durrani of

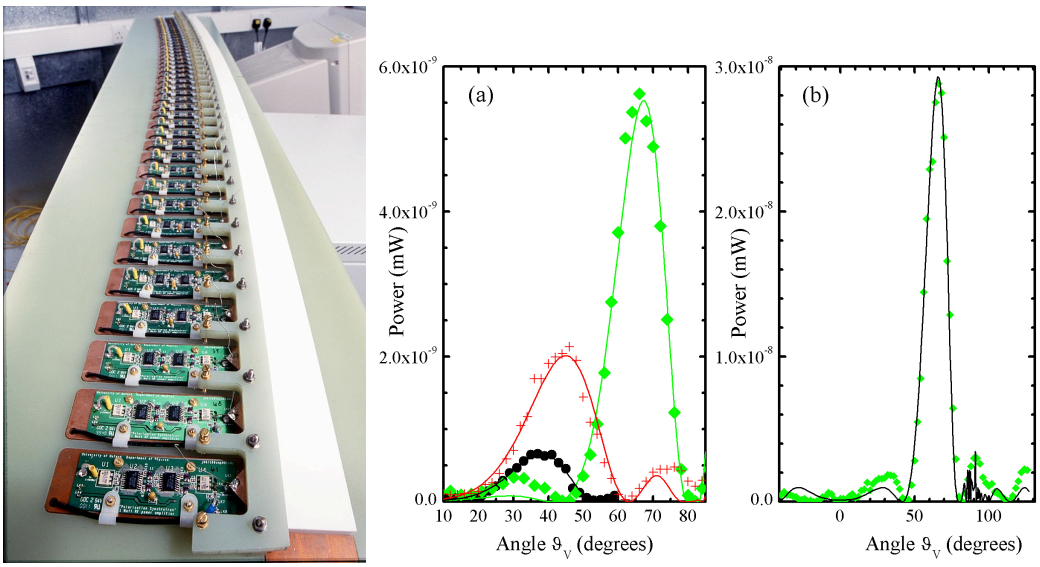

Figure 1.12: Left: Practical superluminal light source. A curved strip of dielectric material is placed between a continuous ground plate and an array of metal electrodes, each of which is connected to an individual amplifier. By turning the amplifiers on and off in sequence one can generate a polarized region that moves along the dielectric at arbitrarily high speeds. The voltage V_j applied to the jth electrode is of the form $V_j = V_0 \cos[m\omega(j\Delta t - t)] \cos(\Omega t)$, where ω and Ω are angular frequencies and m is a positive integer. The source speed v is determined by the phase difference between the oscillations of neighboring electrodes; given the dimensions of the electrodes of the experimental machine, a superluminal speed $v > c$ is obtained for $\Delta t < 148.8ps$. Right: Since the source is traveling faster than the speed of light *in vacuo*, it emits "vacuum Čerenkov radiation" at an angle that depends on the speed of the source alone: The higher the source speed, the narrower the cone.

Physics World [51] stated the obvious by noting that the "revolutionary device polarizes opinions." Anthony Hewish, who shared the 1974 Nobel Prize in physics for the discovery of pulsars, declared the device "a waste of tax-payers' money [52]," claiming cantankerously that the physics "is nonsense" and "simply wrong... The radiation from such a device must be conventional." John Hannay, a theoretical physicist at Bristol University, even believed that he had "come up with a three-line proof which shows beyond doubt that Dr Ardavan's mathematics must be flawed [52]."

The vitriolic press notwithstanding, subsequent experimental and theoretical

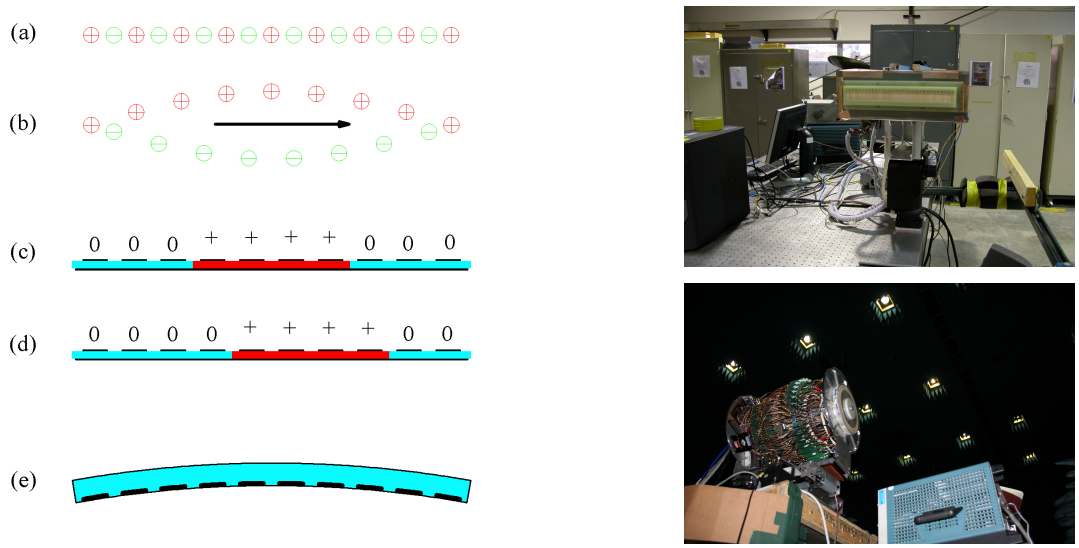

Figure 1.13: Left: Experimental animation of a superluminal polarization current. (a) A simplified dielectric solid containing negative (⊖) and positive (⊕) ions. In (b), a spatially-varying electric field has been applied, causing the positive and negative ions to move in opposite directions; a finite polarization **P** has therefore been induced. If the field is made to move along the direction of the arrow, the polarized region moves with it. (c) Schematic side view of a practical superluminal source, showing metal electrodes above a strip of dielectric (shaded region) and a ground plate below it. "0" indicates that there is no voltage on that particular upper electrode; the symbol + indicates that a positive voltage is applied. The voltage on the electrodes produces a finite polarization of the dielectric (red shading). (d) By switching the voltages on the electrodes on and off, the polarized region can be made to move along the dielectric. (e) Top view, showing the curvature of the dielectric. Right: Practical superluminal light sources built at Los Alamos National Laboratory between 2007 and 2010.

work conducted at Los Alamos National Laboratory and in the UK demonstrated unambiguously that polarization currents can indeed be animated to travel faster than the speed of light *in vacuo*, thereby opening a promising and largely unexplored field in Electrodynamics (Fig. 1.12 right). In parallel, a team under A. V. Bessarab used the ISKRA-5 laser at Sarov to demonstrate emission by superluminal polarization currents, veryifing the fundamental physics involved [38].

Between 2007 and 2011, four second-generation practical superluminal sources were designed, constructed and tested in Los Alamos [35, 36]. Whilst the competing

Russian group demonstrated the feasability of superluminal emission using polarization shock waves in a plasma generated by a photolytically pumped iodine gas laser, the operating principle of the machines in Los Alamos, as well as their British predecessor, is based on electrostatic control and animation of the polarization current; a technique far more amenable for useful and controllable devices. The left-hand panel of Figure 1.13 shows the basic principle: A series of electrodes is placed on one side of a dielectric – a polarizable medium such as alumina – mounted on a ground plate. The application of voltages to the electrodes creates a polarized region underneath; this can then be moved by switching the voltages on the electrodes on and off. The voltage V_j applied to the jth electrode is of the form

$$V_j = V_0 \cos[m\omega(j\Delta t - t)] \cos(\Omega t), \tag{1.19}$$

where ω and Ω are angular frequencies and m is a positive integer. The first cosine gives rise to the polarization-current wave that propagates along the dielectric and the second to a modulation of this wave. The source speed v is determined by the phase difference between the oscillations of neighboring electrodes: Given the sizes of practical devices ($\sim 0.1 - 1$m), superluminal speeds can be readily achieved using switching speeds in the MHz to GHz range (timings $\sim 10 - 10^2$ picoseconds).

The two superluminal light sources shown in Fig. 1.13 (right) have been tested in anechoic chambers and outdoor ranges at Los Alamos as well as Sandia National Laboratories. The linear accelerator, shown in the top right-hand panel of Figure 1.13 and in Figure 1.14, has generated superluminal polarization currents that move at up to 20 times the speed of light and emit coherent beams of radiation [35].

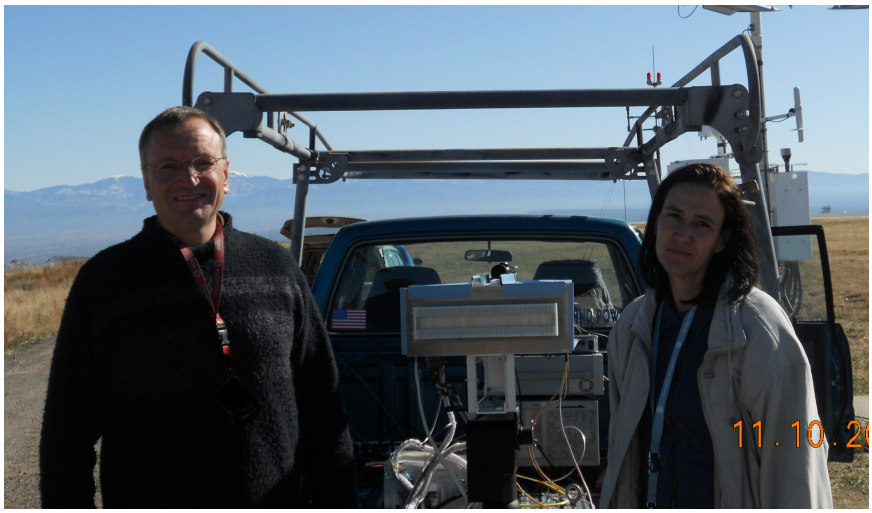

Figure 1.14: John Singleton and Andrea Schmidt at Los Alamos Airport in November 2011, after the first data transmission by a superluminal antenna (center). Herbert Howells' *Magnificat* as well as excerpts from Louis Vierne's *Sanctus* and *Agnus Dei* were broadcast across roughly 500 meters of airstrip.

1.5 Some Organizational Remarks

The remainder of the present thesis is organized as follows: In Chapter 2 we will use basic methods introduced by Huyghens and Fresnel to study point charges, *e.g.,* polarization-current elements of infinitesimal volume, that travel faster than light in a vacuum. In order to facilitate the later discussion, we will investigate the conceptually more transparent case of a point source subject to rectilinear acceleration first and then move on to more complex source paths and geometries. Chapters 3 and 4 are concerned with the calculation of the potentials and radiation fields emitted by such charges, thus adding amplitude to the phase information gained in the previous sections. In Chapter 3 we rederive the fundamental causal solution to the scalar wave equation and argue that integral solutions to Maxwell's equations, derived in the context of stationary or subluminally moving sources, may not always be appropriate in treating faster-than-light charges. Chapter 4 contains the main, substantive point of

the current work: The correct expressions for the Liénard-Wiechert potentials and fields of a point charge travelling arbitrarily fast along a given trajectory are derived and numerically evaluated. Chapter 5 gives a brief summary and outlines future work and, finally, in an appendix, we compare the findings of the previous chapters to the radiation emitted by pulsars.

Chapter 2

Mathematical Treatment I: A Huyghens Analysis

As pointed out in Section 1.1, a source that travels faster than light must be volume-distributed since the electric and magnetic fields due to a point charge moving at superluminal velocities become infinitely strong as they approach the envelope of the emitted wave fronts from the inside [14, 53] and are undefined on the caustic itself. However, the fields generated by extended superluminal sources can be built up from the superposition of the fields of their constituent volume elements, which are essentially point-like. Doing so makes the singularities vanish, provided that the surface – or volume – density of the source, as the case may be, remain finite [53]. This was shown exhaustively by the eccentric British mathematician G. A. Schott, one of the last 'respectable' scientists to oppose the quantum formalism introduced by Niels Bohr. While Schott recognizes that "useful physical theories such as the "*Relatiftheorie*"[1] of Lorentz and Einstein are incompatible" with particle velocities greater than that of light, he considers the limitation to the subluminal regime as "undesirable from the standpoint of complete mathematical generality" [53].

[1] Theory of Special Relativity

Furthermore, as will be discussed in detail in Sections 2.1 – 2.3 below, the radiation field of an extended superluminal source as observed at a given distant point P is dominated by cusp emission, emission from those of its volume elements that approach P, along the radiation direction, with the speed of light and no acceleration at the retarded time. These elements comprise a filamentary part of the source, a threadlike structure whose constituents are all situated at the same optical distance from the observer (see [31, 32, 54–57] and Chapter 3). In consequence, the radiation field of a volume-distributed source in the far zone shares all the intrinsic qualities of that emitted by a point charge, which makes the investigation of the latter not only a necessary prerequisite for the calculation of the radiation received from extended faster-than-light sources, but a tool in its own right for studying the fundamental physics involved in the superluminal emission process.

In the sections to follow we shall study point sources travelling faster than light using the Huyghens constructs introduced briefly in Chapter 1. In particular, we will analyze the relationship between emission and observation time (Sections 2.1 and 2.2), which need not be monotonic and one-to-one: As with sound waves, multiple retarded times – or even extended periods of source time – can contribute to a single instant of reception. We will show that radiation sources that travel not only faster than light, but are also subject to linear acceleration, possess a two-sheeted Čerenkov envelope and a cusp – a region of intense concentration of radiation – where these two sheets meet tangentially. The chapter concludes with a description of the electromagnetic effects associated with the unusual temporal relation between source and observer (Section 2.3), especially those that occur at or near the cusp of the emitted wavefronts, and attemps to quantify them using a "measure" that we christen the "temporal focusing factor."

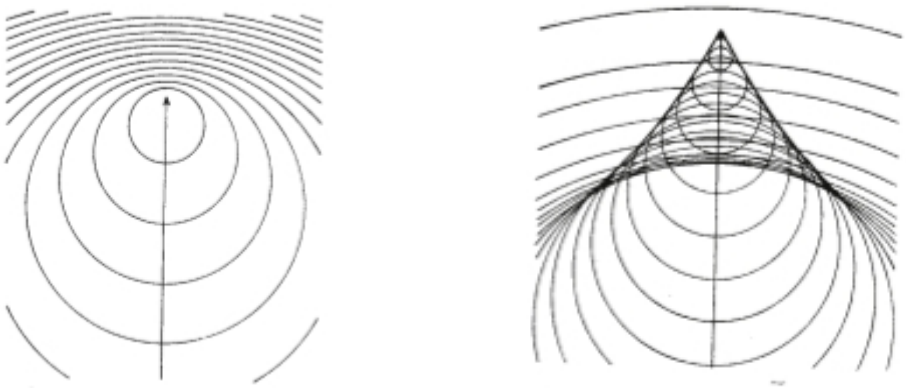

Figure 2.1: Wave fronts emanating from a point charge that travels with constant acceleration parallel to the z-axis of a Cartesian coordinate system. The velocity of the source in the left-hand panel remains below that of light, while the charge to the right accelerates through the "light barrier." (After [10].)

2.1 Point-Charges Subject to Linear Acceleration: (More than) an Introductory Case

The emission of sound waves by a supersonic source in rectilinear acceleration has already been covered in brief in Section 1.2. The analogous case of the superluminal emission process is rather simple in its caustic geometry and conceptually transparent. Hence, it will serve here as a prelude to the analysis of the more complex source paths and geometries which will follow later in this chapter. [2]

Take a point source that travels with constant acceleration a along the z-axis of a Cartesian coordinate system as shown in Figure 2.1, *i.e.,* whose path $\mathbf{x}(t)$ is given by

$$x = \text{const}, \quad y = \text{const}, \quad z = \tilde{z} + ut + \frac{1}{2}at^2, \tag{2.1}$$

where $\tilde{z}$ and u are its position and speed at time $t = 0$, respectively. The wave fronts

[2] The discussions below and in Section 2.2 are much indebted to [53] and Appendix D of [58].

that are emitted by this source in an empty and unbounded space are described by

$$|\mathbf{x}_P - \mathbf{x}(t)| = c(t_P - t), \tag{2.2}$$

where the constant c denotes the wave speed and the space-time of observation points is given by $(\mathbf{x}_P, t_P) = (x_P, y_P, z_P, t_P)$. Inserting Eq. (2.1) into Eq. (2.2) and squaring the resulting expression, we find that the square of the retarded distance R from the source to an observer is

$$\begin{aligned} R^2(t) &\equiv (x_P - x)^2 + (y_P - y)^2 + (z_P - \tilde{z} - ut - \frac{1}{2}at^2)^2 \\ &= c^2(t_P - t)^2. \end{aligned} \tag{2.3}$$

Hence, a retarded time t for observation time t_P must satisfy

$$t_p = t + R(t)/c. \tag{2.4}$$

Characteristic Equation (2.4) simply expresses the fact that the emitted wavefronts travel the distance R at velocity c – the speed of light. If t_P is taken as a variable parameter, the expression describes a family of expanding concentric spheres, namely the successive *loci* of the particular wave emitted at position (x, y, z) and time t . If, on the other hand, one lets t vary, the equation denotes a family of spheres whose centers lie on the path of the charge, *i.e.,* the positions at a given time t_P of all the waves emitted up to that time. As long as the velocity of the charge is less than c, every wave contains all subsequent ones, as is shown in Figure 2.1 (left); in acoustics and radar this is known as the Doppler effect. If the charge travels faster than light, however, and "outruns" the waves that it emits, some of the wavefronts intersect to form an envelope as illustrated in Figure 2.1 (right). If both t_P and t are allowed to vary, the characteristic equation denotes a doubly infinite system of spheres, namely all the positions of all the waves emitted by the source [53].

Returning to Eq. (2.3), we introduce the natural length scale $l = c^2/a$, which allows us to express the equation in terms of the dimensionless entities $\beta = (u+at)/c$

and $\beta_P = (u + at_P)/c$, electromagnetic analogues to the Mach number that denote the scaled values of emission and observation time, respectively, and write

$$\begin{aligned} g(\beta) \equiv \frac{1}{4}\beta^4 - \beta^2 \left(\frac{1}{2}{\beta^2}_P - \frac{(\tilde{z} - \tilde{z}_P)}{l} + 1\right) + 2\beta_P\beta + \left(\frac{1}{2}{\beta^2}_P - \frac{(\tilde{z} - \tilde{z}_P)}{l}\right)^2 \\ - {\beta^2}_P + \frac{[(x - x_P)^2 + (y - y_P)^2]^{1/2}}{l} \\ = 0, \end{aligned} \tag{2.5}$$

where $(\tilde{z} - \tilde{z}_P)/l$ marks the separation between $\tilde{z} = z - ut - \frac{1}{2}at^2$, the position of the source point, and

$$\tilde{z}_P \equiv z_P - ut_P - \frac{1}{2}{at^2}_P, \tag{2.6}$$

the observer's location. Fig. 2.2 shows the relationship between observation and emission time for four characteristic combinations of source speed and observer position.

Since the source travels not only faster than light, but is also subject to linear acceleration, the wave fronts for which $\beta > 1$, *i.e.,* those that are emitted after the source breaks the "light barrier," possess a Čerenkov envelope consisting of two axisymmetric sheets and an elongated nose (Fig. 2.3). This tube-like structure is the *locus* of contributions that stem from points in time at which the charge approaches the observer along the radiation direction and at the speed of light, *e.g.,* emissions for which

$$\partial g/\partial\beta = \beta^3 - (\beta_P^2 - 2\frac{\tilde{z} - \tilde{z}_P}{l} + 2)\beta + 2\beta_P = 0. \tag{2.7}$$

Anywhere within the volume confined by the envelope, the function $g(\beta)$ is oscillatory (Figure 2.2) and images of the source from three retarded times will be received as shown in curve (c). On the envelope of the wavefronts, two contributions from the source's history coalesce and an observer situated on the ordinate will sample two

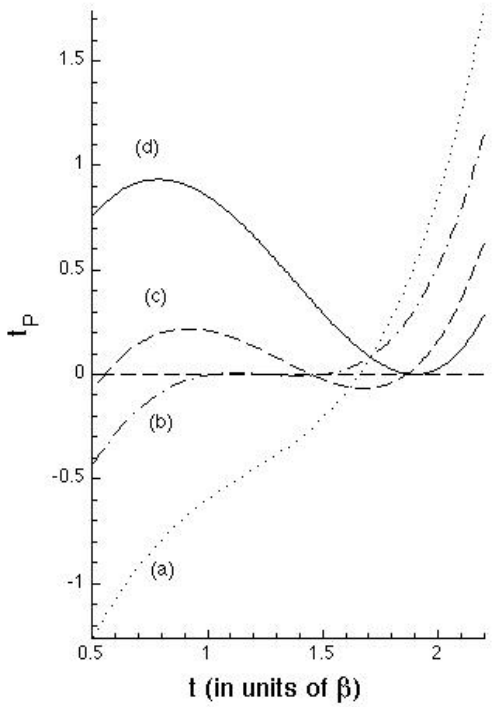

Figure 2.2: Relationship between emission (t) and observation (t_P) time (in units of β) for an observation point (a) outside the envelope, (b) on the cusp of the envelope, (c) inside the envelope and (d) on the envelope.

images, one of which was emitted at $t < 0$, *e.g.,* before the source's existence, and is therefore irrelevant for practical purposes (curve (d)).

Cubic equation (2.7) has three real roots, two of which satisfy the requirement $\beta > 0$. Using Cardano's[3] method [59], we find that these physically relevant solutions are

$$\beta_{\pm} = \frac{2}{\sqrt{3}}(\beta_P^2 - 2\frac{\tilde{z} - \tilde{z_P}}{l} + 2)^{-1/2}\cos[\frac{1}{3}(\pi \pm \sigma)], \tag{2.8}$$

[3] The method is, in fact, due to Scipione del Ferro and Niccolò Fontana Tartaglia, but was published by (and, hence, named after) Gerolamo Cardano in 1545.

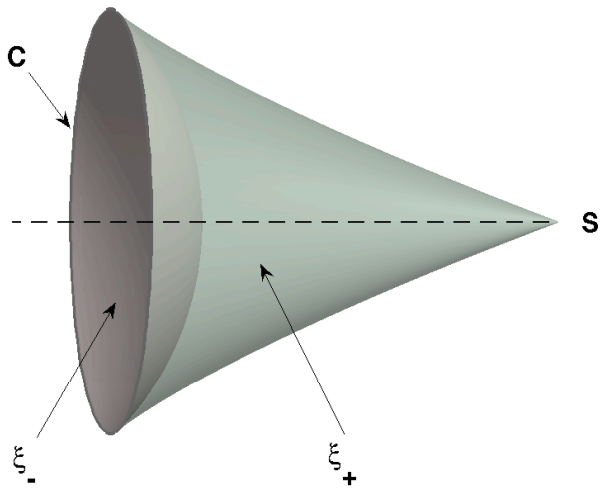

Figure 2.3: Superluminal source that is linearly accelerated. The wave fronts that are emitted after the source breaks the "light barrier" form a Čerenkov envelope consisting of two axisymmetric sheets (ξ_+ and ξ_-) which meet to form the cusp (C), a region of intense concentration of emitted radiation.

where

$$\sigma \equiv \arccos\left[3^{3/2}\beta_P(\beta_P^2 - \frac{2(\tilde{z} - \tilde{z_P})}{l} + 2)^{-3/2}\right]. \tag{2.9}$$

β_+ and β_- denote a local maximum and local minimum of $g(\beta)$, respectively. To calculate the location of the two-sheeted envelope, it is mathematically convenient, if at the expense of physical transparency, to move the problem to the (ζ, ξ) space, where

$$\xi \equiv \frac{[(x - x_P)^2 + (y - y_P)^2]^{1/2}}{l} \tag{2.10}$$

represents the distance of the observation point from the path of the source in units of l and the Lagrangian coordinate

$$\zeta \equiv \frac{\tilde{z} - \tilde{z_P}}{l} \tag{2.11}$$

denotes the separation between source and observation point in the $(x, y, \tilde{z})$ space. Inserting $\beta = \beta_{\pm}$ in equation (2.5) and solving for ξ as a function of ζ, we find that

$$\xi_{\pm} \equiv \left[\frac{1}{2}(\frac{1}{2}\beta_P^2 - \zeta + 1)\beta_{\pm}^2 - \frac{3}{2}\beta_P\beta_{\pm} + \beta_P^2 - (\frac{1}{2}\beta_P^2 - \zeta^2)\right]^{1/2}. \tag{2.12}$$

The two sheets, ξ_+ and ξ_-, meet tangentially to form a cusp, a region of intense concentration of radiation (illustrated in Figure 2.3), that is emitted when the charge approaches the observer not only with the wave speed but with zero acceleration at the retarded time. On the cusp, the function $g(\beta)$ has a point of inflection, as shown in Figure 2.2, curve (b), and $\partial^2 g/\partial\beta^2$ as well as $\partial g/\partial\beta$ and g all vanish. It is easy to see that these "shock waves" of light constitute, in effect, an optical analogue of the "sonic boom;" as shown in Section 1.2, the most intense concentration of sound waves occurs when $\partial r/\partial t = -c$, where r is the retarded separation of aircraft and observer and c – in that case – the speed of sound.

Following a procedure similar to the one outlined in Equation (2.12), the cusp can be described mathematically as a circle expanding at the speed of light around the source's path, where

$$\xi = (\beta_P^{2/3} - 1)^{3/2} \equiv \xi_C, \quad \zeta = \frac{1}{2}\beta_P^2 - \frac{3}{2}\beta_P^{2/3} + 1 \equiv \zeta_C \tag{2.13}$$

and

$$\beta = \beta_P^{1/3} \equiv \beta_C. \tag{2.14}$$

The analysis of faster-than-light sources that move along a rectilinear trajectory serves not only as an introductory case to more complex dynamical systems but has applications in its own right such as the development of novel directed energy and radar technologies [65, 66]. Of more relevance from an astrophysical point of view, however, is the investigation of the electromagnetic fields that arise if a source of this type rotates about a fixed axis at a constant angular frequency. While our studies

of such radiation sources were originally motivated by astronomical observations of pulsars, they extend to rapidly spinning, highly magnetized stellar remenants in general and may aid in the explanation of phenomena as diverse as gamma-ray burst afterglows and the intense radiation received from quasars.

2.2 Anatomy of a Charge in Superluminal Rotation

Consider a localized charge q, *e.g.,* a polarization-current element of infinitesimal volume, that rotates in the X-Y plane at radius r with angular velocity ω, *i.e.,* whose path $\mathbf{x}(t)$, in terms of the cylindrical coordinates (r, φ, z), is

$$r = \text{const}, \quad z = 0, \quad \varphi = \hat{\varphi} + \omega t, \tag{2.15}$$

where the Lagrangian coordinate $\hat{\varphi}$ denotes the initial value of φ and is, without loss of generality, assumed to be zero throughout the remainder of this chapter. The wave fronts that are emitted by such a source in an empty and unbounded space are given by Eq. (2.2), where the constant c denotes the wave speed and the space-time of observation points is defined as $(\mathbf{x}_P, t_P) = (r_P, \varphi_P, z_P, t_P)$; hence, the equation describes expanding spheres of radius $c(t_P - t)$ whose fixed centers $r_P = r$, $\varphi_P = \hat{\varphi} + \omega t = \omega t$ and $z_P = z = 0$ depend on their emission times t.

By the Pythagorean Theorem, the retarded distance R from the source to an observer is given by

$$\begin{aligned} |\mathbf{x}_P - \mathbf{x}(t)| \equiv R(t) &= \left[z_P^2 + r_P^2 + r^2 - 2 r_P r \cos(\varphi_P - \omega t)\right]^{1/2} \\ &= c(t_P - t). \end{aligned} \tag{2.16}$$

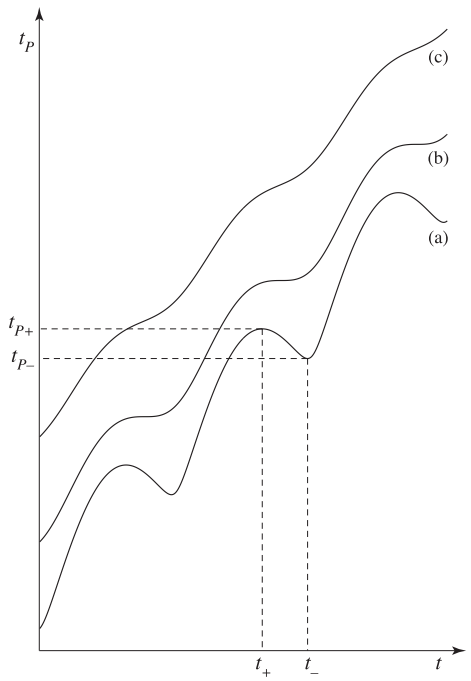

Figure 2.4: Relationship between observation and emission time for an observation point (a) inside, (b) on the cusp of, and (c) outside the envelope. (Curves (a) and (c) are originally given on p. 85 of Ref. [53], (b) in Ref. [58].)

and a retarded time t for observation time t_P must therefore satisfy

$$\begin{aligned} t_P &= t + R(t)/c \\ &= t + \left[z_P^2 + r_P^2 + r^2 - 2r_P r\cos(\varphi_P - \omega t)\right]^{1/2}/c \\ &= h(t). \end{aligned} \tag{2.17}$$

Figure 2.4 shows the function h for three characteristic combinations of source speed and observer position, where solutions of $t_P = h(t)$ are intersections of the horizontal lines t_P with the graph of h. Due to the oscillating term in Eq. (2.16), the function need not be monotonic and one-to-one; $h(t)$ can equal t_P at more than one value of t and there is no longer a straightforward relationship between the (retarded) time at which the source emits and the time at which the emitted waves arrive at an observer or detector. Hence, for case (a) there may be three contributions

from the domain of h for a single observation time. Higher source speeds increase the amplitude of the oscillations in h, resulting in higher odd numbers of retarded times. [4] A space-time diagram depicting the intersection of the trajectory of the point charge S with the past light cone of the observer position P is shown in Figure 2.5.

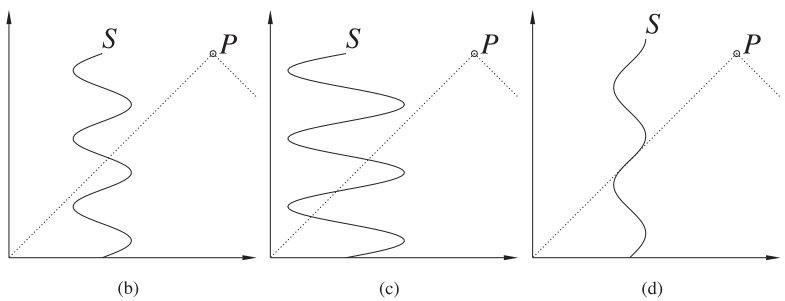

Figure 2.5: (b), (c) and (d) Space-time (*i.e.* ct versus distance x) diagrams showing the intersection of the trajectory of the source point S with the past light cone of the observation point P when P lies outside (b), inside (c), and on the cusp of (d) the envelope of wave fronts.

Analogous to a source that travels along a rectilinear trajectory (discussed in Sections 1.1, 1.2 and 2.1), the wavefronts emitted by a rotating point-charge intersect to form a tubelike structure – the Čerenkov envelope (Fig. 2.6 (left)) – when the source exceeds the wave speed and $r\omega/c > 1$. In Astronomy and Astrophysics, the quantity $r = c/\omega$ is traditionally referred to as the "velocity of light cylinder" (or "light cylinder," in short) and denotes the (imagined) cylinder located at radial distance r from a pulsar's center, where a co-rotating extension of the star would have a speed equal to the velocity of light, *i.e.,* $v/c = 1$, where $v = r\omega$ denotes

[4] Schott showed that this is the case when

$$\tan\sqrt{\left(\frac{\omega}{c}\right)^2 - 1} = \sqrt{\left(\frac{\omega}{c}\right)^2 - 1}, \tag{2.18}$$

that is, for the values $(\omega/c)^2 = 1, 1 + (1.43\pi)^2, 1 + (2.45\pi)^2$....

the instantaneous linear velocity [82, 100]. In this spirit and for mathematical ease, we introduce here the length scale c/ω (where a circumflex over a length variable denotes such a scaled length) and express all distances in units of light cylinders (*e.g.,* $\hat{r} = r\omega/c, \hat{z} = z\omega/c, \hat{r}_P = r_P\omega/c$ and $\hat{z}_P = z_P\omega/c$). We shall, however, on occasion revert to the use of unscaled quantities, most notably for calculating the degree of temporal focusing in Section 2.3, where quantitative measurements are needed.

Since the source is not only moving faster than light, but is also subject to centripetal acceleration, the envelope of the emitted wave fronts consists of two sheets (corresponding to $t_P\pm$ in Fig. 2.4), which form where the caustics meet tangentially and two of the roots of $h(t) = t_P$ coincide (Fig. 2.7). As was shown in Section 1.2 above, the wave fronts that combine to create the envelope are emitted when the charge approaches the observer along the radiation direction at the speed of light and

$$\partial h/\partial t = \frac{1}{\omega}\left[1 - \hat{r}\hat{r}_P \sin(\varphi_P - \omega t)/\hat{R}(t)\right] = 0. \tag{2.19}$$

For points situated on the envelope, *e.g.,* those for which $h(t)$ is as in curve (a) of Fig. 2.4, Eq. (2.19) has the doubly infinite set of solutions $t = t_\pm + 2n\pi$, where

$$t_\pm = \frac{1}{\omega}\left[\varphi_P + 2\pi - \arccos\left(\frac{1 \mp \Delta^{1/2}}{\hat{r}\hat{r}_P}\right)\right], \tag{2.20}$$

$$\Delta \equiv (\hat{r}_P^2 - 1)(\hat{r}^2 - 1) - \hat{z}_P^2, \tag{2.21}$$

and n is an integer. Function $h(t)$ is locally maximum at $t_+ + 2n\pi$ and minimum at $t_- + 2n\pi$.

Inserting $t = t_\pm$ in Eq. (2.17), we find the following expression for $\mathfrak{T}_\pm$, the temporal relation that determine the location of the two sheets of the envelope (Fig. 2.6 left and Fig. 2.7):

$$\mathfrak{T}_\pm \equiv h(t_\pm) = \frac{1}{\omega}\left[2\pi - \arccos\left(\frac{1 \mp \Delta^{1/2}}{\hat{r}\hat{r}_P}\right)\right] + \hat{R}_\pm, \tag{2.22}$$

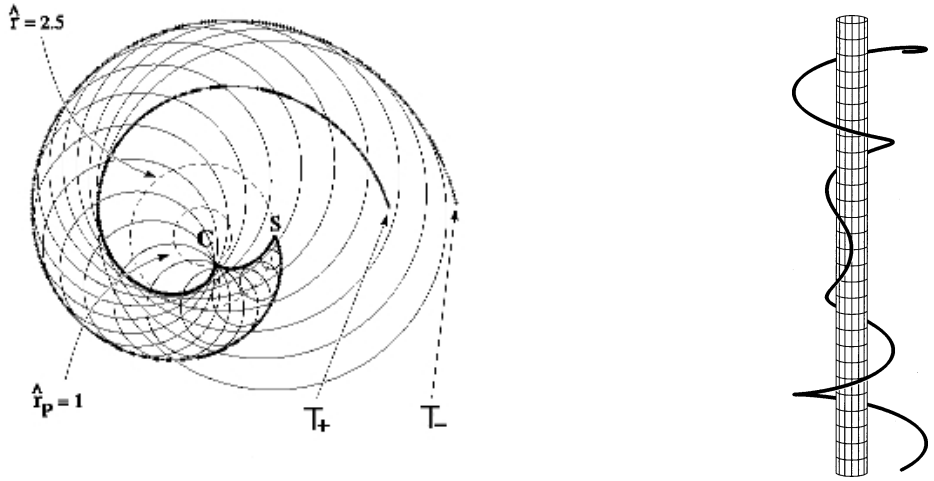

Figure 2.6: Left: Cusp (C) and envelope ($\mathfrak{T}_{\pm}$) of the spherical wave fronts emanating from a point charge (S) in constant superluminal rotation. The bold curves show the cross section of the envelope with the rotational plane of the source. The larger of the two broken circles marks the orbit (at $r = 2.5c/\omega$), the smaller one the velocity of light cylinder ($r = c/\omega$). Right: Segment of the cusp curve, touching the light cylinder before spiraling out above and below the plane of rotation, approaching the cone of polar angle $\arcsin c/r\omega$ in the far field. This expanding spiral shape may be derived from Equation (2.34). (After Ref. [58].)

in which

$$\hat{R}_{\pm} \equiv \left[\hat{z}_P^2 + \hat{r}^2 + \hat{r}_P^2 - 2(1 \mp \Delta^{1/2})\right]^{1/2}. \tag{2.23}$$

denote the values of $\hat{R}$ at time $t = t_{\pm}$.

The two sheets meet tangentially to form a cusp, the *locus* of points that are emitted when the source approaches the observer not only with the wave speed, but with zero acceleration at the retarded time. This corresponds to the inflection point of curve (b) of Fig. 2.4. The cusp curve is tangent to the light cylinder in the plane of rotation (point C in Fig. 2.6 (left)) and spirals out above and below the plane, [5] approaching the cone of polar angle $\theta_P = \arcsin(c/r\omega)$, as shown in Fig. 2.6 (right). Mathematically, $\mathfrak{T}_C$, the temporal relation that determines the location of the cusp

[5] We will encounter this geometrical property of the cusp again in Eq. (2.34).

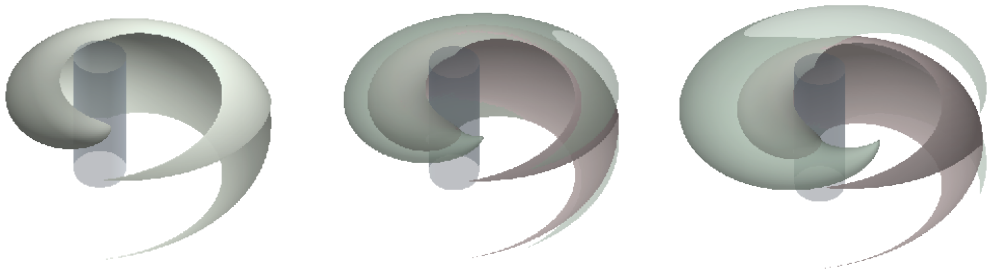

Figure 2.7: Development of the two-sheeted envelope for source velocities of $r\omega = c$ (left), $1.75c$ (center) and $2.5c$ (right).

can be expressed as

$$\mathfrak{T}_C \equiv h(t_C) = \frac{1}{\omega}\left[2\pi - \arccos\left(\frac{1}{\hat{r}\hat{r}_P}\right) + (\hat{r}_P^2\hat{r}^2 - 1)^{1/2}\right], \tag{2.24}$$

$$\hat{z}_C = \hat{z}_P \pm (\hat{r}_P^2 - 1)^{1/2}(\hat{r}^2 - 1)^{1/2}. \tag{2.25}$$

The unusual electromagnetic phenomena associated with the cusp will be investigated more thoroughly in the following section.

2.3 Temporal Focusing and the "Electromagnetic Boom"

Let us examine Figure 2.4 in more detail, in particular curve (b), which corresponds to an observation point located on the cusp of the envelope and is, for our purposes, the most intriguing of the three cases. From visual inspection it is evident that there is an extended region where the gradient of $h(t)$ becomes infinitesimal. In this area, emission covering a prolonged period of source time is compressed into a much shorter period of observation time. This unique effect, which has been demonstrated experimentally [17, 18, 35–37], constitutes temporal focusing, *i.e.,* focusing of radiation in the time domain. In consequence, a relatively weak faster-than-light

source that emits over an extended period of its own time frame may produce very tightly-focused, intense pulses of radiation. As before, this is of course the electromagnetic analogue to the "sonic boom" described in Section 1.2: In the aircraft's frame of reference, low energy sound is emitted over an extended period of time, all of which arrives at a distant location instantaneosly creating a large and concentrated "boom."

The objective of this section is to evaluate the degree of temporal focusing with respect to t_P – the observer's time frame – numerically. To determine the length of source time corresponding to a given reception period, we move a "window" along $h(t)$ as shown in Figure 2.8 (left). The window's height was chosen to be one nanosecond, a period of reception time that allows realistic comparisons with the radiation received from pulsars, since it is the minimum time interval resovable in current astronomical instrumentation. The width of the window is determined by the intersections of the horizontal lines t_{P_0} and $t_{P_0} + 1\text{ns}$ with h.

Calculating the degree of temporal focusing of $h(t)$ is mathematically reminiscent of taking the Lebesgue measure, which is usually introduced as part of the modern theory of integration [67]. In the Lebesgue scheme, instead of partitioning the domain of a function f, the range of f is subdivided, *i.e.,* $\min f \geq y_0 < y_1 < ... < y_n \geq \max f$, to form the sum $\sum_{i=1}^{n} y_{i-1} \cdot \text{measure}(\{x|f(x) \in [y_{i-1}, y_i]\})$. Here, $\text{measure}(\{x|f(x) \in [y_{i-1}, y_i]\})$ is the sum of the lengths of those subintervals of $[a, b]$ on which $y_{i-1} \leq f(x) \leq y_i$ or, in the present case, the differences Δ_i in Figure 2.8. In other words, it is determined how much of the domain is mapped by the function to some value between two end points in the range. While the Lebesgue measure is traditionally intimately connected whith the notion of integrability, we use it here to analyze the behavior of the function $h(t)$ as it transitions through its characteristic forms and to derive quantitative – *e.g.,* measurable – conclusions.

Since we wish particularly to examine the radiation sampled by an observer sit-

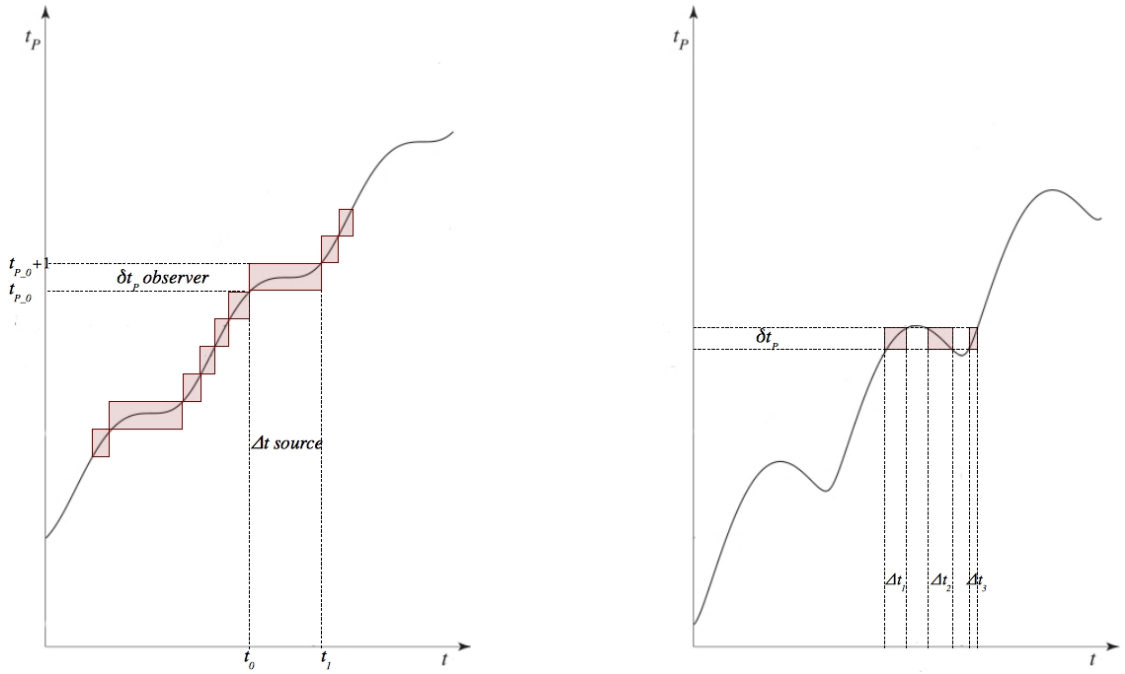

Figure 2.8: Left: The curve $t_P = h(t)$ (see Eq. (2.17)) for an observation point on, or very close to, the cusp, *e.g.,* $\theta_P = \theta_{P_C}$. The reception time window δt_P (observer) slides along the curve, and the corresponding limits in the source's time frame, t_0 and t_1, are found. The degree of temporal focusing is $\Delta t/\delta t_P$, where $\Delta t = t_1 - t_0$. Right: The curve $t_P = h(t)$ for the case $\theta_{P_C} < \theta_P < 180^o - \theta_{P_C}$. Here, there are three windows of Δt corresponding to δt_P. To assess the degree of temporal focusing, $\Delta t/\delta t_P$ is again used, but with $\Delta t = \Delta t_1 + \Delta t_2 + \Delta t_3$.

uated on (or very close to) the cusp of the envelope, the first step is to choose such an observation position (r_P, φ_P, z_P) approximately. [6] The value of z_P is then refined until the desired accuracy is achieved.

The process begins with a choice of r_P and the use of the far-field approximation for θ_P, the polar angle of the cusp location,

$$\sin\theta_P = \frac{c}{r\omega}. \tag{2.26}$$

[6] Notice that Equations (2.24) and (2.25), albeit analytically exact, cannot be used here since we are seeking the location of the cusp in terms of the observer's frame of reference, rather than the source's, *e.g.,* we are trying to find z_{P_C}, not z_C.

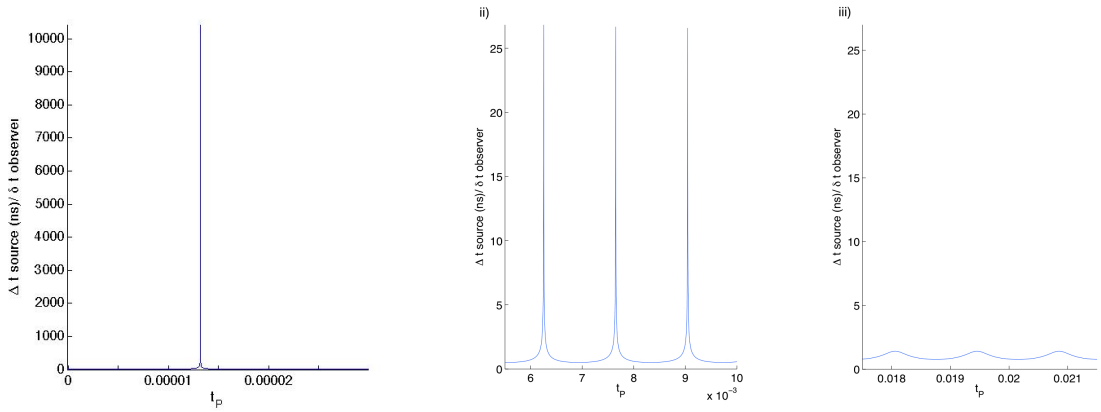

Figure 2.9: Left: Degree of temporal focusing calculated for an observer situated on the cusp. More than $10,000$ns of source time are compressed into a single ns of reception time, which is, analogous to the "sonic boom," perceived as a powerful electromagnetic pulse. This "electromagnetic boom" passes the observer once during each rotation of the source (center). Right: Outside the envelope, temporal focusing is almost imperceptible.

The relation relation between θ_P, r_P and z_P then gives a first estimate for z_P, namely

$$\tan\theta_P = \frac{r_P}{z_P}. \tag{2.27}$$

To refine the location more precisely, recall that in Section 2.2, Eq. (2.16), we established that the square of the retarded distance R from the source to an observer is

$$R^2 = z_P^2 + r_P^2 + r^2 - 2rr_P\cos\omega t, \tag{2.28}$$

where φ_P has, without loss of generality, been set to zero. [7] Taking the first and second partial derivatives with respect to t on both sides of (2.28) yields

$$R\frac{\partial R}{\partial t} = rr_P\omega\sin\omega t \tag{2.29}$$

[7] φ_P is irrelevant here, as for the correct values of r_P and z_P the cusp must pass the observer once each rotation (see Fig. 2.9 (center)).

and

$$\left(\frac{\partial R}{\partial t}\right)^2 + R\frac{\partial^2 R}{\partial t^2} = r r_P \omega^2 \cos\omega t, \tag{2.30}$$

respectively. Since the charge approaches the observer at the speed of light and zero acceleration,

$$\frac{\partial R}{\partial t} = -c \quad \text{and} \quad \frac{\partial^2 R}{\partial t^2} = 0;$$

hence,

$$r r_P \omega^2 \cos\omega t = c^2. \tag{2.31}$$

To eliminate t from the above equation, we make use of the relations

$$\cos\omega t = \frac{c^2}{r r_P \omega^2} \quad \text{and} \tag{2.32}$$

$$\sin\omega t = \left(1 - \frac{c^4}{r^2 r_P^2 \omega^4}\right)^{1/2}, \tag{2.33}$$

and utilize (2.28) and (2.29) such that

$$\frac{r^2 r_P^2 \omega^2 \left(1 - \frac{c^4}{r^2 r_P^2 \omega^4}\right)}{r_P^2 + r^2 - 2\frac{c^2}{r r_P \omega^2} r r_P + z_P^2} = c^2. \tag{2.34}$$

It is (2.34) that defines the expanding, spiral-shaped *locus* of the cusp curve described at the beginning of the present section and shown in Fig. 4.1.

Rearranging terms and substituting the linear velocity v for $r\omega$, we find that

$$\frac{c^2}{v^2}\left(1 + \frac{v^2 - c^2}{\omega^2(r_P^2 + z_P^2)}\right) = \frac{r_P^2}{r_P^2 + z_P^2} = \sin^2\theta_P. \tag{2.35}$$

Equation (2.35) gives the means to refine z_P until the cusp is located to the desired precision. This is done by iterating through

$$z_P = r_P / \tan\theta_P \tag{2.36}$$

and

$$\theta_{P_{new}} = \arcsin\left[\frac{c}{v}\left(1 + \frac{v^2 - c^2}{\omega^2(r_P^2 + z_P^2)}\right)^{1/2}\right] \tag{2.37}$$

until convergence for θ_P is reached. This procedure, albeit simple, tends to converge to a precision of 10^{-15} in less than 20 iterations.

Once the values of r_P and z_P have been determined, the function $t_P = h(t)$ (Eq. (2.17)) can be generated for an abitrarily small neighborhood around the cusp location. As shown in Fig. 2.8 (left), the window of observation time, $\delta t_P = 1$ns, can be moved along this curve and the corresponding upper and lower limits in the source-time domain, t_0 and t_1, determined. In the discussion that follows below, we will plot the ratio $\Delta t/\delta t_P$, where $\Delta t = t_1 - t_0$, as a measure of the degree of temporal focusing. The root-finding procedure used to find the retarded times t and their values will be outlined in detail in Section 4.1 and can be found in Section 4.4.

Having located the cusp, z_P can be raised or lowered to assess the degree of temporal focusing on either side. Figure 2.8 (right) shows $t_P = h(t)$ for a location $\theta_{P_C} < \theta_P < 180^o - \theta_{P_C}$, where θ_{P_C} denotes the exact angle of observation of the cusp. In this case, there are values for t_P at which either – or both – edges of the window δt_P intersect the curve $t_P = h(t)$ on more than one occasion. In such cases we calculate $\Delta t = \sum_i \Delta t_i$ as in Fig. 2.8 (right), where the Δt_i denote the extent of source time for each contribution. Fig. 2.9 (left) shows the results of a calculation of $\Delta t/\delta t_P$ for a point on the cusp. Values of $\omega = 4.5 \times 10^3/2\pi$ Hz and $r = 10^5$ m were chosen to reflect a pulsar similar in size and characteristics to the Crab (see Appendix A). The observer is located at $r_{P_C} = 3 \times 10^5$ m and $z_{P_C} \approx 3.2744 \times 10^5$ m, where the subscript C, as in previous sections, denotes "cusp". It is clear that a very large amount of source time, *e.g.,* 1.0421×10^4 ns, is compressed into 1 ns of observation time. The exceptional degree of focusing in the time domain that occurs on (or near) the cusp is responsible for some of the intriguing properties of cusp radiation (*e.g.,* its unusual "brightness" and non-spherical decay, see Chapter 3), which, in Appendix A,

will be relevant for the analysis and interpretation of astronomical data. The degree of temporal focusing for several θ_P is shown in Fig. 2.10 (top). The bottom panel shows the corresponding $t_P = h(t)$ curves and observer locations. As mentioned above in the discussion of Fig. 2.9, $\Delta t/\delta t_P$ exhibits a pronounced spike at locations for which $\theta_P = \theta_{P_C}$, *i.e.,* those that are subject to cusp radiation. For $\theta_P < \theta_{P_C}$ or $\theta_P > 180^o - \theta_{P_C}$, a single hump is observed, but for $\theta_{P_C} < \theta_P < 180^o - \theta_{P_C}$, the three intervals of source time that arrive within one interval of observation time result in a double-horned structure. As will be seen later, these features resemble closely those observed in pulsar light curves. Figure 2.10 is also suggestive of how the fact that cusp radiation from an extended source decays more slowly than predicted by the inverse square law (see Chapter 3) does not violate conservation of energy. Though $\Delta t/\delta t_P$ exhibits huge spikes on the cusp, elsewhere it is much less than one, which is to say that the radiation that is expended to form the strong fields on the cusp – a travelling caustic that is constantly dispersed and reconstructed from different waves – is "stolen" from weaker fields elsewhere in the emitted radiation. In the case of a stationary source, $\Delta t/\delta t_P$ would be one everywhere since there exists an exact correspondence between observation and retarded time.

Using, in essence, basic methods established by Huyghens and Fresnel, we have quantitatively analyzed ("measured") the relation between emission and observation time of a radiation source in constant superluminal rotation and found that intriguing phenomena occur on the cusp and within the envelope of the emitted wave fronts. To investigate these unusual features further, we now proceed to calculate the more sophisticated Liénard-Wiechert potentials and fields for these locations, thereby introducing amplitude in addition to phase information. First, however, we will issue a word of caution against using textbook *formulae*, derived in the context of stationary or subluminal sources, indiscriminately when treating faster-than-light charges. This will be the focus of the next chapter.

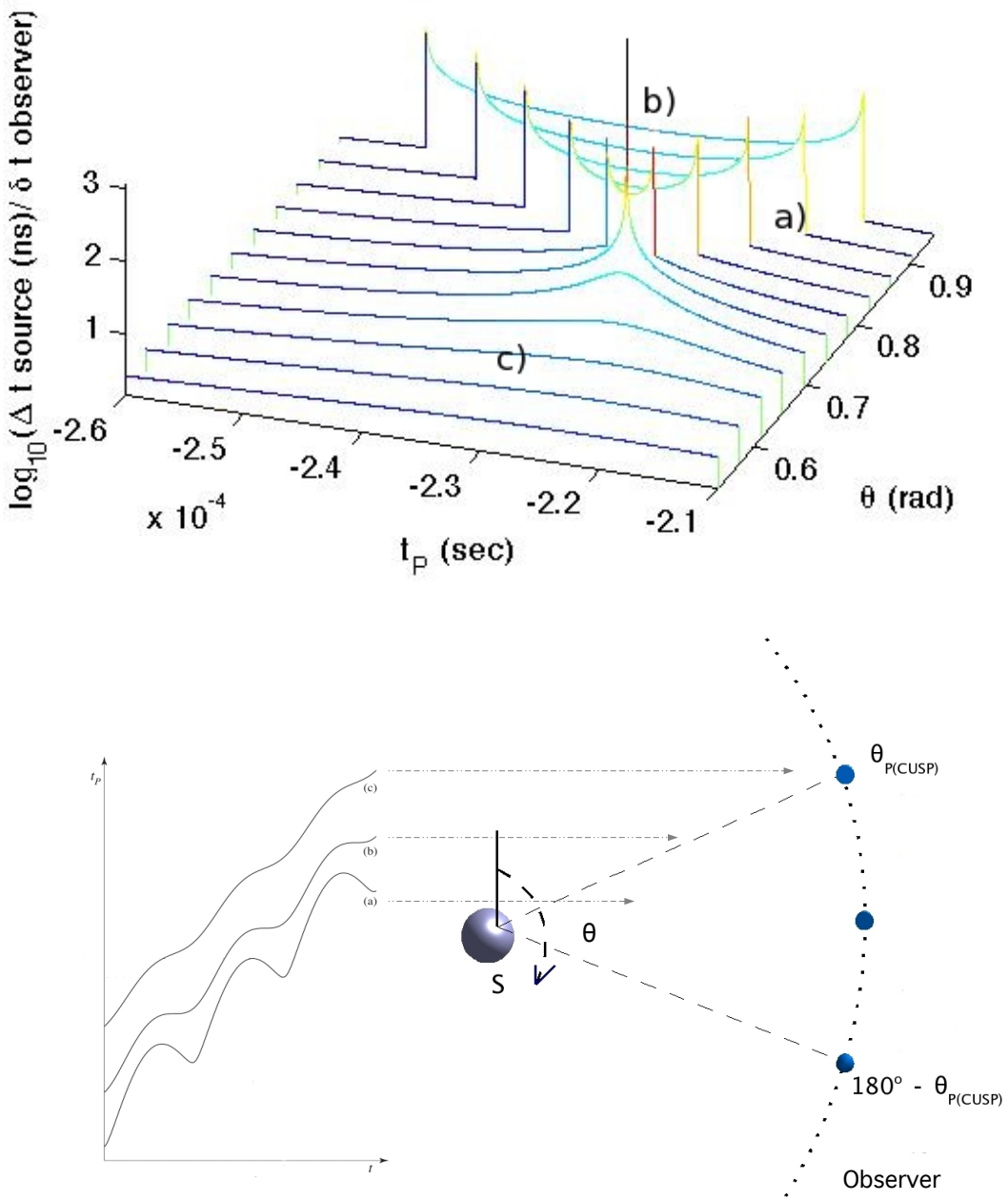

Figure 2.10: Top: Waterfall plot for the degree of temporal focusing (a) inside, (b) on the cusp of, and (c) outside the envelope of the wave fronts. $\Delta t/\delta t_P$ exhibits a pronounced spike at locations for which $\theta_P = \theta_{P_C}$. For $\theta_P < \theta_{P_C}$ or $\theta_P > 180^o - \theta_{P_C}$, a single, broader peak is observed, but for $\theta_{P_C} < \theta_P < 180^o - \theta_{P_C}$, *e.g.,* region (b), the three intervals of source time that arrive within one interval of observation time result in a double-horned structure. Bottom: Corresponding $t_P = h(t)$ curves and observer locations.

Chapter 3

Potentials, Fields and How to Treat Them

Many texts in electromagnetism contain retarded integral solutions to Maxwell's equations that may be evaluated to give the time-dependent electric and magnetic fields due to a charge (or charges) in motion (see, *e.g.,* [33] or [60]). Generated either directly from the wave equations governing the fields or via the analogous expressions for the retarded potentials, these solutions are applied widely to treat, for example, synchrotron radiation and the power radiated by various antennae. The question, therefore, arises as to why these solutions, derived in the context of stationary or subluminal sources, must be used with circumspection in the present context of charges that exceed the speed of light.

We have already established (Chapter 2) that superluminal sources are unusual in that the radiation received at a distance may contain contributions from multiple retarded times, or even an extended period of emission time. As we now show, it is precisely this feature of faster-than-light sources that leads to difficulties with standard textbook expressions. Thus we are left with the alternative between the

integral solution, Equation (3.2), or the integral equation (3.12). Both are correct, but we will focus on the latter.

In the sections to follow we will demonstrate, by an intuitive argument, that part of the radiation field generated by a rotating superluminal source decays as $1/d$, rather than spherically as $1/d^2$, with distance d, implying that the radiation *stays focused in the far field*. We then derive the fundamental causal solution, or causal "Green's function solution" to the scalar wave equation governing the electromagnetic field *ab initio* and show that the resulting *formula* contains a surface integral which includes the gradient of the radiation field and reflects its boundary conditions. The boundary term may be (and is) neglected if it diminishes with distance faster than the contribution of the source density, a volume integral traditionally called the "source term." This is the case for conventional radiation sources, whose emission decays according to the inverse square law, but not for a source whose distribution pattern both rotates and travels faster than light. Hence, an argument based on a retarded integral solution which neglects the boundary term (as given, *e.g.,* on page 246 of [33]) ignores nonspherically-decaying contributions to the field, which, as we have shown, dominate in the far zone (see, *e.g.,* the discussion of the "electromagnetic boom" in Section 2.3). We conclude the chapter with a brief introduction to electromagnetic potentials, and, in the process, demonstrate that results derived from the retarded potentials – rather than the fields – do not depend crucially on the boundary term, which, in this case, can always be rendered equal to zero by virtue of a gauge transformation.

3.1 Radiation That Stays Focused in the Far Field – An Intuitive Argument

As evidenced in Chapter 2, the most intense electromagnetic disturbances caused by a point-like source in constant superluminal rotation occur on the cusp of the wave fronts, which is emitted when the charge approches the observer not only with the wave speed but with no acceleration at the retarded time. We observed that on this *locus* (given by Equation (2.34)), the degree of temporal focusing is sharply peaked (Figures 2.9 and 2.10). As the cusp, reminiscent of an old-fashioned bed spring in shape, spirals up and out into the far field, it asymptotically approaches a cone of semi-angle $\arcsin c/v$.

Let us now assume that this source is extended, and that it can be treated as a collection of closely spaced source points. All source elements situated at a constant radius and lying on a filament extending vertically (*i.e.,* parallel to the rotation axis) must possess the same instantaneous velocity. Their cusps will, therefore, propagate outwards in unison along parallel paths. In consequence, a distant observer will encounter a vertical line of cusps whose reach in the z–direction is determined *only* by the vertical extent of the filamentary source. Such a string of cusps produces what appears to be an unusual "beam" (or "subbeam," as it is often referred to in the literature [57]), with fixed azimuthal *angular* width (because the temporally-focused pulse rotates rigidly with the source), but a z–extent that is fixed in *height*, leading to a polar angular width that narrows with separation from the source. The energy in this beam is spread over an area that increases with distance, rather than distance squared, leading to an intensity that falls off nonspherically as $1/d$ (Figure 3.1).

Though the discussion thus far has just involved a simple qualitative extension of the temporal focusing concepts introduced in Chapter 2, detailed analytical studies ([17, 18, 35, 36]) as well as experimental observations ([31, 32, 55]) confirm that tem-

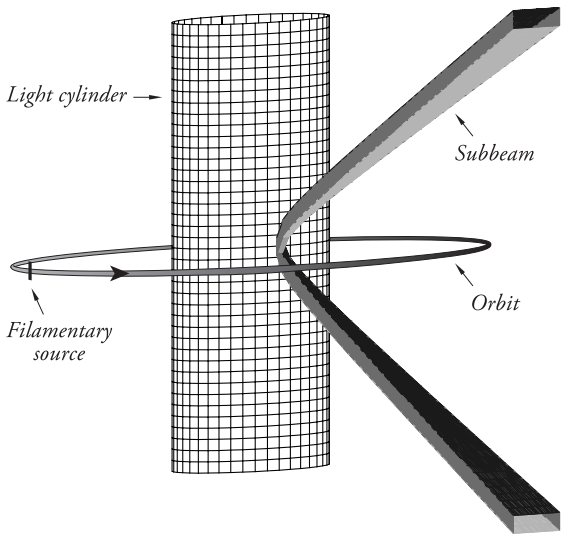

Figure 3.1: Schematic illustration of the light cylinder $r = c/\omega$, the filamentary part of the source that approaches the observation point with the speed of light and zero acceleration at the retarded time, the orbit $r = c/(\omega \sin\theta_{\rm P})$ of this filamentary source, and the subbeam formed by the bundle of cusps that emanate from the constituent volume elements of this filament.

poral focusing leads to the magnitude of this particular component of the source's emission falling off more slowly than emission from a conventional radiation source which diminishes as $1/d^2$ with distance d. This nonspherically decaying component of the radiation appears as a spiral-shaped packet of intense localized electromagnetic waves, a diffraction-free propagating caustic that, when detected by a far-field observer, presents itself as a powerful pulse of light. The fact that cusp radiation decays more slowly than predicted by the inverse square law does not violate conservation of energy since the radiation field is not isotropic; weaker fields elsewhere in the emitted radiation compensate for the strong fields on the cusp (again, see [17, 18, 31, 32, 35, 36, 55] and the discussion of Figure 2.9), which is constantly reconstructed from conventional (*i.e.,* spherically decaying) waves that combine and disperse. Because the "beams" are narrower, in angular terms, the farther away from the source they are detected, the absolute value of the gradient of the radiation field

associated with them will *increase* with distance, rather than decrease, as is the case for conventional, diffracting radiation.

That a radiation field which possesses a gradient that increases, rather than decreases, with distance, does not *per se* constitute a violation of the conservation laws, as can be illustrated with the following *gedankenexperiment*, borrowed from [56]:

Imagine a rotating radiation beam with the amplitude

$$A(R_P, \varphi_P, t_P) = A_0 \hat{R}_P^{1/2} \exp[-(\hat{R}_P^3 \hat{\varphi}_P)^2]$$

where, as before, $\hat{R}_P$ stands for the scaled distance $R_P\omega/c$, $\hat{\varphi}_P \equiv \varphi_P - \omega t_P$ is the azimuthal angle in the rotating frame, t_P denotes the observation time, and A_0 is a constant. This beam would be observed as a Gaussian pulse that has an azimuthal width of the order of $\hat{R}_P^{-3}$ and carries a constant flux of energy,

$$\int A^2 R_P^2 \sin\theta_P d\theta_P d\varphi_P = (2\pi)^{1/2}(c/\omega)^2 A_0^2,$$

across any large sphere of radius R_P. The gradient of the amplitude of this pulse,

$$\partial A/\partial\hat{\varphi}_P = -2A_0 \hat{R}_P^{7/2}(\hat{R}_P^3\hat{\varphi}_P)\exp[-(\hat{R}_P^3\hat{\varphi}_P)^2],$$

increases in magnitude with distance as $R_P^{7/2}$ at the edges of the pulse.

It has been shown explicitly that the gradient of the nonspherically decaying field generated by a source in superluminal rotation increases as $d^{7/2}$ with distance d. The derivation of these results, however, is non-trivial and exceeds the scope of this work; we refer the interested reader to [56]or [57] instead.

3.2 Derivation of the Fields *via* the Inhomogeneous Wave Equation

In Section 1.3.1 we described that electric and magnetic fields arising from varying distributions of electric charges and currents can, with wave-like motion, propagate indefinitely through space, far from the varying charges and currents where they originated. We then proceeded to show that Maxwell's four equations can easily be combined to yield a pair of homogeneous three dimensional wave equations governing the electric and the magnetic field intensities *in vacuo* and far from the sources of their origin.

In the presence of sources, the inhomogeneous wave equation that governs the electric and magnetic field intensities can be given in the general form [60]

$$\nabla^2\Psi - \frac{1}{c^2}\frac{\partial^2\Psi}{\partial t^2} = -4\pi q(\mathbf{x}, t), \tag{3.1}$$

where the function $q(\mathbf{x}, t)$ describes the charge density, giving not only the distribution of the sources, but also their time dependence at each point in space.[1]

The issue of mathematical rigor has already been covered in brief in the abstract and will be further discussed in Chapter 5. In the context of Equation (3.1) this is to mean the following. There exists a unique smooth solution of the initial value problem of the inhomogeneous wave equation (3.1) when the function q and the initial data $\Psi(\cdot, 0)$, $\frac{\partial\Psi}{\partial t}(\cdot, 0)$ are sufficiently smooth functions (see, *e.g.,* [61], Section

[1] In the interest of generality, we extend the discussion to follow to source distributions, rather than restrict it to point charges as in previous chapters. We will return to the treatment of point sources in Chapter 4, where we discuss the potentials and fields emitted by a single charged particle moving at an arbitrary velocity.

2.4). This solution has the form

$$\Psi(\mathbf{x},t) = \int_{B_t(\mathbf{x})} \frac{q(\mathbf{y}, t-|\mathbf{x}-\mathbf{y}|/c)}{|\mathbf{x}-\mathbf{y}|} d\mathbf{y} + \frac{1}{4\pi c^2 t}\int_{\partial B_t(\mathbf{x})} \frac{\partial \Psi}{\partial t}(\mathbf{y},0) d\sigma(\mathbf{y}) + \frac{1}{4\pi c^2}\frac{\partial}{\partial t}[\frac{1}{t}\int_{\partial B_t(\mathbf{x})} \Psi(\mathbf{y},0) d\sigma(\mathbf{y})] \ , \qquad (3.2)$$

where $t \geq 0$ and

$$B_t(\mathbf{x}) := \{\mathbf{y} \in \mathbb{R}^3 : |\mathbf{x}-\mathbf{y}| \leq ct\} \ , \quad \partial B_t(\mathbf{x}) := \{\mathbf{y} \in \mathbb{R}^3 : |\mathbf{x}-\mathbf{y}| = ct\} \ . \quad (3.3)$$

Returning to (3.1), we wish to find the fundamental solution (or, equivalently, the Green's function) for the problem, that is, the response of the physical system to a concentrated or impulsive forcing function. By inspection, we suggest

$$\nabla^2 G - \frac{1}{c^2}\frac{\partial^2 G}{\partial t^2} = -4\pi\delta(\mathbf{x_P}-\mathbf{x})\delta(t_P - t), \qquad (3.4)$$

where, as in previous chapters, t is the retarded time, the time at which light must be emitted from location $\mathbf{x}$ in order to reach location $\mathbf{x_P}$ at time t_P. Clearly, the source is an impulse occuring at time t and location $\mathbf{x}$. G then gives the description of the effect of this impulse as it travels away from $\mathbf{x}$ in the course of time. It seems reasonable to impose causality as an initial condition, *e.g.,* that G and $\partial G/\partial t$ should be zero for $t_P < t$: if an impulse occurs at t, no effects of this impulse should be present at an earlier time. The directionality in time imposed by the Cauchy conditions implies that (3.4) is invariant under time translation and the reciprocity relation becomes (see, *e.g.,* pg 835 of [60] for a detailed discussion):

$$G(\mathbf{x_P}, t_P|\mathbf{x}, t) = G(\mathbf{x}, -t|\mathbf{x_P}, -t_P). \qquad (3.5)$$

To solve (3.1), we use this reciprocity relation and write

$$\nabla^2 G(\mathbf{x_P}, t_P|\mathbf{x}, t) - \frac{1}{c^2}\frac{\partial^2 G(\mathbf{x_P}, t_P|\mathbf{x}, t)}{\partial t^2} = -4\pi\delta(\mathbf{x_P}-\mathbf{x})\delta(t_P - t). \qquad (3.6)$$

Multiplying (3.1) by G, (3.6) by Ψ and subtracting the latter from the former results in

$$G\nabla^2\Psi - \Psi\nabla^2 G + \frac{1}{c^2}\left(\frac{\partial^2 G}{\partial t^2}\Psi - G\frac{\partial^2\Psi}{\partial t^2}\right) = 4\pi\left\{\Psi\delta(\mathbf{x_P}-\mathbf{x})\delta(t_P - t) - q(\mathbf{x},t)G\right\}, \quad (3.7)$$

and we may now integrate over the volume of interest as well as t:

$$\int_0^{t_\mathrm{P}} \mathrm{d}t \int_V \mathrm{d}^3x \left\{G\nabla^2\Psi - \Psi\nabla^2 G + \frac{1}{c^2}\left(\frac{\partial^2 G}{\partial t^2}\Psi - G\frac{\partial^2\Psi}{\partial t^2}\right)\right\} = 4\pi\left\{\Psi(\mathbf{x_P}, t_P) - \int_0^{t_\mathrm{P}} \mathrm{d}t \int_V \mathrm{d}^3x\, q(\mathbf{x},t)G\right\}. \quad (3.8)$$

Since

$$G\nabla^2\Psi - \Psi\nabla^2 G = \nabla\cdot(G\nabla\Psi - \Psi\nabla G), \quad (3.9)$$

we utilize the vector form of Green's theorem (see, *e.g.,* [63]) and write

$$\int_V \mathrm{d}^3x\, G\nabla^2\Psi - \Psi\nabla^2 G = \int_\Sigma \mathrm{d}\mathbf{S}\cdot(G\nabla\Psi - \Psi\nabla G). \quad (3.10)$$

Hence, Equation (3.8) can be re-stated as

$$\int_0^{t_\mathrm{P}} \mathrm{d}t \int_\Sigma \mathrm{d}\mathbf{S}\cdot(G\nabla\Psi - \Psi\nabla G) + \frac{1}{c^2}\int_V \mathrm{d}^3x \left[\frac{\partial G}{\partial t}\Psi - G\frac{\partial\Psi}{\partial t}\right]_0^{t_P} + 4\pi\int_0^{t_\mathrm{P}} \mathrm{d}t \int_V \mathrm{d}^3x\, q(\mathbf{x},t)G = 4\pi\Psi(\mathbf{x_P}, t_P) \quad (3.11)$$

and, after formally integrating the second term, [2] the complete solution to the inhomogeneous problem (3.1), including the satisfaction of initial conditions, becomes

$$\Psi(\mathbf{x}_\mathrm{P}, t_\mathrm{P}) = \int_0^{t_\mathrm{P}} \mathrm{d}t \int_V \mathrm{d}^3x\, q(\mathbf{x},t)G + \frac{1}{4\pi}\int_0^{t_\mathrm{P}} \mathrm{d}t \int_\Sigma \mathrm{d}\mathbf{S}\cdot(G\nabla\Psi - \Psi\nabla G) - \frac{1}{4\pi c^2}\int_V \mathrm{d}^3x \left(\frac{\partial G}{\partial t}\Psi - G\frac{\partial\Psi}{\partial t}\right)_{t=0}. \quad (3.12)$$

[2]Notice that the integrand vanishes when evaluated at $t = t_P$ due to the initial conditions imposed on G.

The first integral on the right side of Equation (3.12) is the source term, which stands for the effect of the sources q distributed throughout the volume V, the last involves the effect of the initial conditions, and the second – the boundary term – represents the effect of the boundary conditions on space boundaries. It is the boundary term around which the current discussion is centered.

In the derivation of Equation (3.12), the sole assumption made on the volume V is that it contains $\mathbf{x}_P$. We now remark further on V, so let $(\mathbf{x}_P, t_P)$ be fixed. If we choose V such that the ball $B_{t_P}(\mathbf{x})$ is a subset of V, then the boundary term, i.e., the second term on the RHS of (3.12), vanishes and (3.12) is identical to (3.2). If, however, V is chosen as a subset of $B_{t_P}(\mathbf{x})$, then, in general, the second term on the RHS of (3.12) does not vanish since it has to 'compensate' information for $\Psi(\mathbf{x}_P, t_P)$ that is 'missing' in the first and third terms on the RHS of (3.12). Thus, by choosing an appropriate V, the second term on the RHS of (3.12) may yield interesting information about $\Psi(\mathbf{x}_P, t_P)$.

Various methods can be applied to find the explicit form of the Green's function G in Eq. (3.4). Here we proceed to remove the explicit time dependence by introducing a Fourier transform with respect to frequency. We assume that $\Psi(\mathbf{x_P}, t_P)$ and $q(\mathbf{x}, t)$ have the Fourier integral representations

$$\Psi(\mathbf{x_P}, t_P) = \frac{1}{2\pi} \int_{-\infty}^{\infty} \mathrm{d}\omega \, \tilde{\Psi}(\mathbf{x_P}, \omega) e^{i\omega t} \qquad \text{and} \tag{3.13}$$

$$q(\mathbf{x}, t) = \frac{1}{2\pi} \int_{-\infty}^{\infty} \mathrm{d}\omega \, \tilde{q}(\mathbf{x}, \omega) e^{i\omega t} \qquad \text{where} \tag{3.14}$$

$$\tilde{\Psi}(\mathbf{x_P}, \omega) = \int_{-\infty}^{\infty} \mathrm{d}t \, \Psi(\mathbf{x_P}, t_P) e^{i\omega t}, \tag{3.15}$$

$$\tilde{q}(\mathbf{x}, \omega) = \int_{-\infty}^{\infty} \mathrm{d}t \, q(\mathbf{x}, t) e^{i\omega t} \tag{3.16}$$

Introducing the Fourier integrals into (3.1) we find that they satisfy the inhomogeneous Helmholtz equation

$$\left(\nabla^2 + \frac{\omega^2}{c^2}\right) \tilde{\Psi}(\mathbf{x_P}, \omega) = -4\pi\tilde{q}(\mathbf{x}, \omega) \tag{3.17}$$

Hence, upon insertion of the Green's function appropriate for the problem we have

$$\left(\nabla^2 + k^2\right) g(\mathbf{x_P}, \omega|\mathbf{x}, t) = -4\pi\delta(\mathbf{x_P} - \mathbf{x}), \tag{3.18}$$

where $k = \omega/c$ denotes the wave number. In the absence of boundary surfaces, the Green's function can depend only on $R = |\mathbf{x_P} - \mathbf{x}|$ and must possess spherical symmetry about the source point. We write, in spherical coordinates,

$$\frac{1}{R}\frac{\mathrm{d}^2}{\mathrm{d}R^2}\,(R\,g) + \frac{\omega^2}{c^2}\,g = -4\pi\delta(\mathbf{R}). \tag{3.19}$$

For $\mathbf{R} \neq 0$, the right hand side of (3.19) is identically zero and $R\,g(R)$ satisfies the homogeneous equation

$$\frac{1}{R}\frac{\mathrm{d}^2}{\mathrm{d}R^2}\,(R\,g) + \frac{\omega^2}{c^2}\,g = 0, \tag{3.20}$$

which has the solution

$$\begin{aligned} R\,g &= Ae^{ikR} + Be^{-ikR} \\ g &= \frac{1}{R}\,(Ae^{ikR} + Be^{-ikR}). \end{aligned} \tag{3.21}$$

Near the origin, where the delta function contributes, the second term on the left hand side of (3.18) is negligible compared to the first, and the equation becomes

$$\nabla^2\,g = -4\pi\delta(\mathbf{x_P} - \mathbf{x}), \tag{3.22}$$

which is satisfied by

$$\lim_{kR\to 0} g(R) = \frac{1}{R}. \tag{3.23}$$

Hence the general solution for the Green's function is

$$g(\mathbf{x_P}, \omega|\mathbf{x}, t) = \frac{1}{R}\left(Ae^{ikR} + Be^{-ikR}\right). \tag{3.24}$$

Using the inverse transforms from (3.13), we finally write the time-dependent Green's function as

$$G(\mathbf{x_P}, t_P|\mathbf{x}, t) = \frac{A}{R}\delta\left[t - (t_P - R/c)\right] + \frac{B}{R}\delta\left[t - (t_P + R/c)\right]. \tag{3.25}$$

The first term in Equation (3.25) is called the *retarded* Green's function because it exhibits the causal behavior associated with a wave disturbance: An effect observed at point $\mathbf{x_P}$ at time t_P is caused by the action of a source at distance R at an earlier time $t = t_P - R/c$. The second term, the *advanced* Green's function, must be rejected as it does not satisfy the causality condition imposed earlier, namely, that no response may be predicted to an event occurring in the future. Hence, $B \equiv 0$, which implies $A = 1$, and

$$G(\mathbf{x_P}, t_P|\mathbf{x}, t) = \frac{\delta\left[(R/c) - (t_P - t)\right]}{R}; \qquad R,\, t_P - t > 0. \tag{3.26}$$

Let us now examine the specific case of the inhomogeneous wave equation that governs the magnetic field, $\mathbf{B}$. In analogy with (3.1), it can be written as

$$\nabla^2\mathbf{B} - \frac{1}{c^2}\frac{\partial^2\mathbf{B}}{\partial t^2} = -4\pi\frac{\boldsymbol{\nabla}\times\mathbf{j}}{c} \tag{3.27}$$

and has the full solution

$$\begin{aligned}\mathbf{B}(\mathbf{x}_\mathrm{P}, t_\mathrm{P}) =& \frac{1}{c}\int_0^{t_\mathrm{P}} \mathrm{d}t \int_V \mathrm{d}^3x\,(\boldsymbol{\nabla}\times\mathbf{j})G + \frac{1}{4\pi}\int_0^{t_\mathrm{P}} \mathrm{d}t \int_\Sigma \mathrm{d}\mathbf{S}\cdot(G\nabla\mathbf{B} - \mathbf{B}\nabla G) \\ &- \frac{1}{4\pi c^2}\int_V \mathrm{d}^3x\Big(\mathbf{B}\frac{\partial G}{\partial t} - G\frac{\partial\mathbf{B}}{\partial t}\Big)_{t=0}\end{aligned} \tag{3.28}$$

with G as given in (3.26). Here, the source $q(\mathbf{x}, t)$ is assumed to be a current with density $\mathbf{j}$. Under the null initial conditions $\mathbf{B}|_{t=0} = (\partial\mathbf{B}/\partial t)_{t=0} = 0$ assumed throughout this chapter (see above), the third term in Eq. (3.28) is identically zero and the expression reduces to

$$\mathbf{B}(\mathbf{x}_\mathrm{P}, t_\mathrm{P}) = \frac{1}{c}\int_0^{t_\mathrm{P}} \mathrm{d}t \int_V \mathrm{d}^3x\,(\boldsymbol{\nabla}\times\mathbf{j})G + \frac{1}{4\pi}\int_0^{t_\mathrm{P}} \mathrm{d}t \int_\Sigma \mathrm{d}\mathbf{S}\cdot(G\nabla\mathbf{B} - \mathbf{B}\nabla G). \tag{3.29}$$

However, in some standard textbooks (see, *e.g.,* Eq. (6.52) of [33]), *formula* (3.29) is published as

$$\mathbf{B}(\mathbf{x}_{\mathrm{P}}, t_{\mathrm{P}}) \simeq \frac{1}{c} \int \mathrm{d}^3 x \frac{[\boldsymbol{\nabla} \times \mathbf{j}]_{ret}}{|\mathbf{x}_{\mathrm{P}} - \mathbf{x}|}. \tag{3.30}$$

It is immediately obvious that the derivation of Eq. (3.30) involves the neglect of the boundary term, which here entails a surface integral over the boundary values of both the field and its gradient.[3] In the case of a conventional source, this boundary term decays more rapidly with distance than the integral that remains in Eq. (3.30). For a rotating superluminal source, where the gradient of the field increases as $R_{\mathrm{P}}^{7/2}$ with the distance R_{P} from its source, this boundary contribution is proportional to $R_{\mathrm{P}}^{-1/2}$ [56]. Not only is this not negligible relative to the contribution from the source term, *but the boundary term constitutes the dominant contribution to the radiation field in this case* [56].

It is important to note that the radiation field cannot be calculated directly from the integral equation (3.12) (the solution whose boundary term is normally neglected [41–45]), as it is merely a mathematical identity, not a solution that could be used to calculate the field arising from a given source distribution in free space. Thus we are left with the alternative between Equation (3.2) or (3.12). As will be shown in the next section, one can instead first solve the wave equation governing the *potential* (whose solution is independent of the boundary term) and then use this solution to evaluate the neglected term in the exact version of the retarded solution for the field (Eq. (3.28)). Thus, one could argue that the rôle of the classical expression for the retarded potential in radiation theory is much more fundamental than that of the corresponding retarded solution of the wave equation governing the field [56]. Clearly, one way to calculate the free-space radiation field of an accelerated superluminal source is to calculate the retarded potential and differentiate the resulting expression

[3] Note also that the Green's function G has been integrated over t_P and is given explicitly as $\frac{1}{|\mathbf{x_P}-\mathbf{x}|}$.

to find the field [56,57] (see also [32,48]). This will be shown in detail in Section 4.1, where we derive the Liénard-Wiechert fields for a charge moving arbitrarily fast from the corresponding potentials.

3.3 Derivation of the Fields *via* the Retarded Potentials

The calculations in Section 3.2 illustrate that the results of an analysis based on the retarded solution to the wave equation governing the field depend crucially on the boundary conditions satisfied by the field at infinity. Here we will show that, if we instead base our analysis on the retarded potential, we require no corresponding explicit knowledge of the value of the potential in the radiation zone. Contrary to the claims made, *e.g.,* in [41–45], there is no discrepancy between the results obtained from the retarded solution for the potential and the retarded solution for the field once the boundary term in the solution to the wave equation governing the field is retained.

3.3.1 In the Lorenz Gauge

In the simplest of terms, a potential is taken to be a function whose derivative yields a field [33,60]. Hence, fields are associated with forces, potentials with energy. If we define he magnetic vector potential $\mathbf{A}$ in terms of the magnetic field $\mathbf{B}$ [33],

$$\mathbf{B} = \nabla \times \mathbf{A}, \tag{3.31}$$

Faraday's law (1.4) can be written

$$\nabla \times \left(\mathbf{E} + \frac{\partial \mathbf{A}}{\partial t} \right) = 0, \tag{3.32}$$

and the quantity with vanishing curl in (3.32) may be expressed as the gradient of some scalar function, namely the electric scalar potential Φ [33]:

$$\mathbf{E} = -\nabla\Phi - \frac{\partial \mathbf{A}}{\partial t}. \tag{3.33}$$

The definition of $\mathbf{B}$ and $\mathbf{E}$ in terms of the potentials (3.31) and (3.33) satisfies identically the two homogeneous Maxwell's equations (1.3) and (1.4). The inhomogeneous equations can be expressed in terms of the potentials using relations (1.6) and (1.7) while recalling that $(\epsilon_0\mu_0)^{1/2} = c$,

$$\nabla^2\Phi + \frac{\partial}{\partial t}\left(\nabla \cdot \mathbf{A}\right) = -\frac{\rho}{\epsilon_0} \tag{3.34}$$

and

$$\nabla^2\mathbf{A} - \frac{1}{c^2}\frac{\partial^2 \mathbf{A}}{\partial t^2} - \nabla\left(\nabla \cdot \mathbf{A} + \frac{1}{c^2}\frac{\partial \Phi}{\partial t}\right) = -\mu_0\mathbf{J}. \tag{3.35}$$

Thus the set of Maxwell's equations has been whittled down to two – if coupled – expressions. Elementary electromagnetism (and basic calculus), however, suggests that there must be some freedom in the choice of Φ and $\mathbf{A}$: While the fields $\mathbf{B}$ and $\mathbf{E}$ are unique and cannot change, they are both defined in terms of *derivatives* of the potentials; in consequence, there exists an infinite family of possible potentials that will all lead to the same fields. Since $\mathbf{B}$ is defined through (3.31) in terms of $\mathbf{A}$, the vector potential is arbitrary to the extent that the gradient of some scalar function Λ can be added. Hence, $\mathbf{B}$ is left unchanged by the transformation

$$\mathbf{A} \to \mathbf{A}' = \mathbf{A} + \nabla\Lambda. \tag{3.36}$$

The above expression is called a *gauge transformation* of the vector potential; it leaves the field invariant. For the electic field to be unchanged as well, the scalar potential needs to be similarly transformed, namely

$$\Phi \to \Phi' = \Phi - \frac{\partial \Lambda}{\partial t}. \tag{3.37}$$

Hence we can choose a set of potentials that satisfy the Lorenz condition [4]

$$\nabla \cdot \mathbf{A} - \frac{1}{c^2}\frac{\partial}{\partial t}\Phi = 0 \tag{3.38}$$

and uncouple Equations (3.34) and (3.35) such that we are left with two homogeneous wave equations that can be written in the familiar form (3.1):

$$\nabla^2 \mathbf{A} - \frac{1}{c^2}\frac{\partial^2 \mathbf{A}}{\partial t^2} = -\mu_0 \mathbf{J} \tag{3.39}$$

and

$$\nabla^2 \Phi - \frac{1}{c^2}\frac{\partial^2 \Phi}{\partial t^2} = -\frac{\rho}{\epsilon_0}. \tag{3.40}$$

[33] emphasizes that Equations (3.39) and (3.40) together with the Lorenz condition (3.38) form a set of equations equivalent to the Maxwell's equations *in vacuo*, as observed by Lorenz *et al.*

The expressions for the *retarded* potentials describe the scalar or vector potential for electromagnetic fields of a time-varying current or charge distribution. As is the case for the fields, the retardation of the influence connecting cause and effect is thereby essential; *e.g.,* the signal takes a finite time, corresponding to the propagation at the velocity of light, to travel the distance from $\mathbf{x}$ to $\mathbf{x_P}$, where an effect is produced or measured.[5] This temporal relation for sub- and superluminal sources has already been discussed in detail in Chapters 2.

[4] Named after Ludvig Valentin Lorenz (1829–1891), a Danish mathematician and physicist. Not to be confused with the *Dutch* physicist Hendrik Lorentz.

[5] The same principle underlies the derivation of Special Relativity, so that all rigorously-defined descriptions of Electromagnetism – *e.g.,* Maxwell's Equations – are necessarily relativistic [33, 83].

3.3.2 The Classical Expression for the Retarded Potential

In the Lorenz gauge, (*i.e.,* the choice of a set of potentials $(\mathbf{A}, A^0)$ that satisfy the Lorenz condition $\boldsymbol{\nabla}\cdot\mathbf{A} + c^{-2}\partial A^0/\partial t = 0$), the electromagnetic fields

$$\mathbf{E} = -\nabla_{\mathrm{P}} A^0 - \frac{1}{c}\frac{\partial \mathbf{A}}{\partial t_{\mathrm{P}}}, \qquad \mathbf{B} = \nabla_{\mathrm{P}} \times \mathbf{A}, \tag{3.41}$$

are given by a four-potential[6] A^μ that satisfies the wave equation

$$\nabla^2 A^\mu - \frac{1}{c^2}\frac{\partial^2 A^\mu}{\partial t^2} = -\frac{4\pi}{c} j^\mu, \qquad \mu = 0, \cdots, 3, \tag{3.42}$$

where A^0/c and j^0/c are the electric potential and charge density and A^μ and j^μ for $\mu = 1, 2, 3$ are the Cartesian components of the magnetic potential $\mathbf{A}$ and the current density $\mathbf{j}$ [33]. As we have seen in the sections above, the solution to the initial-boundary value problem for Eq. (3.42) satisfies the Green's identity

$$\begin{aligned} A^\mu(\mathbf{x}_{\mathrm{P}}, t_{\mathrm{P}}) =& \frac{1}{c}\int_0^{t_{\mathrm{P}}} \mathrm{d}t \int_V \mathrm{d}^3x\, j^\mu G + \frac{1}{4\pi}\int_0^{t_{\mathrm{P}}} \mathrm{d}t \int_\Sigma \mathrm{d}\mathbf{S}\cdot(G\nabla A^\mu - A^\mu \nabla G) \\ & - \frac{1}{4\pi c^2}\int_V \mathrm{d}^3x \Big(A^\mu \frac{\partial G}{\partial t} - G\frac{\partial A^\mu}{\partial t}\Big)_{t=0}, \end{aligned} \tag{3.43}$$

in which G is the retarded free-space Green's function given in equation (3.26), and Σ is the surface enclosing the volume V of the retarded distribution of the localized source already discussed in Section 3.2.

While Equation (3.43) is deceptively similar in form to (3.12) (derived in Section 3.2), there is a fundamental difference between the retarded solution of the wave

[6]The electromagnetic four-potential combines both an electric scalar potential and a magnetic vector potential into a single four-vector. In cgs units it can be defined as

$$A^\mu = (\Phi, \mathbf{A})$$

in which Φ is the electric, $\mathbf{A}$ the magnetic potential. The fields associated with the four-potential are

$$\mathbf{E} = -\nabla\Phi - \frac{1}{c}\frac{\partial}{\partial t}\mathbf{A}, \quad \mathbf{B} = \nabla \times \mathbf{A}.$$

equation that governs the field and the corresponding expression for the potentials: As discussed in the previous section, one can always use the freedom implied in gauge transformations (3.36) and (3.37) to choose potentials such that the boundary contribution (the second term) in Eq. (3.43) is made to vanish, since this term, too, satisfies the homogeneous wave equation. Under the null initial conditions $A^\mu|_{t=0} = (\partial A^\mu/\partial t)_{t=0} = 0$ assumed here, the contribution from the third term in Eq. (3.43) is identically zero, and the retarded Green's function has the familiar form (3.13).

Irrespective of whether the radiation decays spherically (as in the case of a conventional source) or nonspherically (as applies for a rotating superluminal source—see Section 3.1 and [31, 56]), therefore, the potential A^μ due to a localized source distribution that is switched on at $t = 0$ in an unbounded space can be calculated from the first term in Eq. (3.43):

$$A^\mu(\mathbf{x}_\mathrm{P}, t_\mathrm{P}) = c^{-1} \int \mathrm{d}^3x\mathrm{d}t\, j^\mu(\mathbf{x}, t)\delta(t_\mathrm{P} - t - R/c)/R, \tag{3.44}$$

i.e., from the classical expression for the retarded potential.

In conclusion, we have seen in this section that the indiscriminate application of integral solutions to Maxwell's equations, derived within the standard theory of moving charges, can yield misleading answers in the superluminal regime if terms are omitted that are negligible for subluminal sources, but that may dominate in the case of superluminal ones. To wit, if one ignores the boundary term in the retarded solution of the wave equation governing the field, as in [33, 41–45], one obtains a different result, in the superluminal regime, from that obtained by calculating the field via the retarded potential [31, 32, 48]. This apparent contradiction stems solely from having ignored a term in the solution to the wave equation that is, by a factor of the order of $R_\mathrm{P}^{1/2}$, larger than the term that is normally kept, and disappears once the neglected term is taken into account.

We note, furthermore, that the representation

$$\mathbf{A}(\mathbf{x}_{\mathrm{P}}, t_{\mathrm{P}}) = \frac{1}{c} \int \mathrm{d}^3 x \, \frac{[\mathbf{j}(\mathbf{x}, t)]_{ret}}{|\mathbf{x} - \mathbf{x}_{\mathrm{P}}|}, \tag{3.45}$$

of the retarded potential is differentiable as a classical (as opposed to generalized) function only in the case of a moving source whose speed does not exceed that of the waves it generates. Contrary to the usual assumption [41–45], the retarded distribution of the density of a moving source is not necessarily smooth and differentiable if its rest-frame distribution is: As we have seen in Chapter 2.1, the retarded distribution of a rotating source with a moderate superluminal speed is in general spread over three disjoint volumes (differing in shape from each other and from the volume occupied by the source in its rest frame) whose boundaries depend on the space-time position of the observer. Hence, in the superluminal regime, derivatives of the integral representing the retarded potential are well-defined only as generalized functions [55]. For an outline of a rigorous treatment in terms of generalized functions, see Chapter 5 .

We submit that the key issue is, in essence, the presence of multiple or extended retarded times and the associated non-spherical decay observed in the far field. In what follows, we therefore return to basics, to the fundamental Liénard-Wiechert potentials and fields, and take great care in the evaluation of the retarded times involved in the problem.

Chapter 4

Mathematical Treatment II: Liénard-Wiechert Potentials and Fields

The expressions for the radiation field emitted by a single charged particle moving at an arbitrary velocity – in essence a generalized solution to Maxwell's equations – were formulated correctly in 1898 by Alfred-Marie Liénard (1869-1958) and Emil Wiechert (1861-1928), before the advent of the special theory of relativity. Equivalent solutions were given by Sommerfeld (1904) and Schott (1912); for detailed historical and mathematical accounts, see, *e.g.,* [53] or [68]. As shown by Maxwell (Section 1.3.1), electromagnetic waves, once emitted by a charged particle, will propagate at the speed of light, irrespective of how fast the particle is moving, just as sound waves propagate at a speed independent of the source's velocity. Hence, as pointed out in Section 1.3.2 and Chapter 3, Maxwell's equations are invariant under Lorentz transformations and the results derived by Liénard and Wiechert, in consequence, relativistic [33].

Here we will rederive their calculations, which are today encountered in the analysis of synchrotron radiation, and generalize them such that the speed of the source is not restricted to the subluminal regime (Section 4.1). In Section 4.2, we proceed to evaluate the radiated fields derived in 4.1 numerically, which requires a detailed investigation of the function that determines the temporal separation between source and observer (already encountered in Chapter 2). As will be seen, the relation $h(t)$ is of the form of Kepler's equation for elliptical orbits and poses unexpected difficulties when solved for large (*e.g.,* astronomical) distances. Finally, the chapter concludes with a discussion of the results of the evaluations of the Liénard-Wiechert field for faster-than-light charges.

4.1 Liénard and Wiechert's *formulae* for a Charge Moving Arbitrarily Fast

The Liénard-Wiechert potentials $\mathbf{A}$ and Φ describe radiation emanating from a moving electric point charge in terms of a vector and a scalar potential, respectively, and are discussed in many excellent texts to which we refer the interested reader (see, for example, [33] or [68]). Built directly from Maxwell's equations, they give the complete, relativistically correct, time-varying electromagnetic field for a point charge q in arbitrary motion. Developed by Alfred-Marie Liénard and, independently, Emil Wiechert in the late 1800s, they can be written [33]

$$\Phi(\mathbf{x_P}, t_P) = \left[\frac{q}{(1-\boldsymbol{\beta}\cdot\mathbf{n})R}\right]_{ret}, \quad \mathbf{A}(\mathbf{x_P}, t_P) = \left[\frac{q\boldsymbol{\beta}}{(1-\boldsymbol{\beta}\cdot\mathbf{n})R}\right]_{ret}. \tag{4.1}$$

Here, as before, $\mathbf{R}(t) \equiv |\mathbf{x_P} - \mathbf{x}|$ denotes the temporal separation between source and observer, $\mathbf{n} \equiv \mathbf{R}/R$ designates the radiation direction, and $\boldsymbol{\beta} \equiv \mathbf{v}/c$ is the velocity vector of the source scaled by the speed of light. The subscript "ret" indicates that the quantity within the brackets is to be evaluated at the retarded time.

As discussed in detail in Section 3.3.1, the corresponding electric and magnetic fields – the Liénard-Wiechert fields – can be calculated directly from the potentials (4.1), using the definitions $\mathbf{E} = -\nabla\Phi - \partial\mathbf{A}/\partial t$ and $\mathbf{B} = \nabla \times \mathbf{A}$, listed as Equations 3.31 and 3.33 in Section 3.3.1. The derivation, however, is non-trivial and requires a number of steps, which exceed the scope of this work and can be found in standard textbooks. Here, we just state the result and give the expressions for the fields as follows [33]:

$$\mathbf{E}(\mathbf{x}_P, t_P) = q\left[\frac{\mathbf{n}-\boldsymbol{\beta}}{\gamma^2(1-\boldsymbol{\beta}\cdot\mathbf{n})^3R^2}\right]_{ret} + \frac{q}{c}\left[\frac{\mathbf{n}\times\{(\mathbf{n}-\boldsymbol{\beta})\times\dot{\boldsymbol{\beta}}\}}{(1-\boldsymbol{\beta}\cdot\mathbf{n})^3R}\right]_{ret} \tag{4.2}$$

and $\mathbf{B} = \mathbf{n}\times\mathbf{E}$.

Here,

$$\gamma = \sqrt{\frac{1}{1-\boldsymbol{\beta}^2}},$$

denotes the Lorentz factor, a quantity encountered ubiquitously in electrodynamics. As advanced in the introduction to this chapter, *formulae* (4.2) are generalized solutions to Maxwell's equations and describe the radiation field emitted by a single charged particle traveling along an arbitrary path. Today, they are widely used in the standard analysis of synchrotron radiation. Jackson ([33], p. 657) points out that they divide themselves naturally into "velocity fields," which are independent of acceleration, and "acceleration fields," which depend linearly on $\dot{\boldsymbol{\beta}}$. The velocity fields are essentially static fields falling off as R^{-2}, whereas the acceleration fields are typical radiation fields varying as R^{-1}.

While the formulation of the Liénard-Wiechert potentials as given in (4.1) (and in most standard textbooks) is sufficient to describe charges that remain subluminal, they must be generalized if the source is allowed to travel arbitrarily fast and multiple retarded times may occur. We propose

$$\Phi(\mathbf{x_P}, t_P) = q\sum_{t_{ret}}\left[\frac{1}{|1-\boldsymbol{\beta}\cdot\mathbf{n}|R}\right], \quad \mathbf{A}(\mathbf{x_P}, t_P) = q\sum_{t_{ret}}\left[\frac{\boldsymbol{\beta}}{|1-\boldsymbol{\beta}\cdot\mathbf{n}|R}\right], \tag{4.3}$$

where we added summations and absolute-value brackets in the factor $|1 - \boldsymbol{\beta} \cdot \mathbf{n}|$, which stems from the evaluation of the Dirac delta function $\delta(t - t_P + R/c)$ ((3.26) after having made use of the reciprocity relation (3.5)) in the classical expression for the retarded potential (Eq. (3.42)). Both are typically omitted from textbook derivations, since for the subluminal regime, retarded times are unique and $1 - \boldsymbol{\beta} \cdot \mathbf{n}$ must be positive. We note that the potentials diverge where $\boldsymbol{\beta} \cdot \mathbf{n} = 1$; that is, where the source approaches the observer at the speed of light. Furthermore, it is easy to see that Equations (4.3) reduce to (4.1) for a point source whose velocity remains below c.

Here we verify that the potentials (4.3) are indeed fundamental causal solutions for Maxwell's equations for the special case of a point charge in uniform circular motion. We recall from Sections 3.2 and 3.3 that the scalar potential arising from the polarization-current element of infinitesimal volume considered in Section 2.2 satisfies the retarded solution of the wave equation and may hence be written

$$\nabla^2 G - \frac{1}{c^2} \frac{\partial^2 G}{\partial t^2} = -4\pi\rho, \tag{4.4}$$

in which

$$\rho(r, \varphi, z, t) = \delta(r - r_P)\delta(\varphi - \omega t - \hat{\varphi})\delta(z - z_P)/r \tag{4.5}$$

is the density of a point source of unit strength moving along the trajectory (2.15) [32]. As before, r, φ, z and t indicate retarded quantities, whereas the space-time of observation points is denoted by the subscript P. The Lagrangian coordinate $\hat{\varphi}$ stands, as in Section 2.2, for the initial value of φ and is, without loss of generality, assumed to be zero. Causality is imposed by demanding that the solution be zero before any cause takes effect, which excludes from the outset the consideration of anti-causal derivations.

Since the scalar potential Φ must also satisfy 3.40, it is sufficient to show that

$G \equiv \Phi(\mathbf{x_P}, t_P)$, *e.g.,*

$$G = q \sum_{t_{ret}} \left[\frac{1}{|1 - \boldsymbol{\beta} \cdot \mathbf{n}| R} \right] = \Phi(\mathbf{x}, t), \tag{4.6}$$

where $q = 1$ since the charge is of unit strength. In other words, we need to ascertain that $\Phi(\mathbf{x_P}, t_P)$ satisfies the equation for the Green's function G in (4.4).

In the absence of boundaries and accounting for the conditions (2.15), the potential in (4.4) has the value [32]

$$\begin{aligned} G(\mathbf{x_P}, t_P) &= \int d^3x dt \rho(\mathbf{x}, t) \\ &\quad \times \delta(t_P - t - |\mathbf{x_P} - \mathbf{x}|/c)/|\mathbf{x_P} - \mathbf{x}| \\ &= \int_{-\infty}^{+\infty} dt \delta(t_P - t - R(t)/c)/R(t). \end{aligned} \tag{4.7}$$

where $R(t)$ is the function defined in (2.16). After substituting $h(t)$ for $t_P - t - R(t)/c$ and formally evaluating the integral, (4.7) may be rewritten as[1]

$$G = \sum_{t=t_j} \frac{1}{R|\partial h(t)/\partial t|}, \tag{4.8}$$

where the retarded times t_j are, of course, the roots of the transcendental equation $h(t)$ (Equation (2.17), already discussed at length in Chapter 2) and correspond to the retarded times at which the source point $(\mathbf{x}, t)$ makes its contribution towards the value of G at the observation point $(\mathbf{x_P}, t_P)$.

Equation (4.8) confirms the results that we derived in Chapter 2 using basic Huyghens techniques: Namely that the potential G of a point source is discontinous on the envelope and the cusp of the wave fronts. If we approach the envelope from

[1] Due to the integral form of the generalized scaling property,

$$\int_{-\infty}^{+\infty} \mathrm{dx\, f(x) \delta(g(x))} = \sum_{\mathrm{i}} \frac{\mathrm{f(x_i)}}{|\mathrm{g'(x_i)}|},$$

where the summation extends over all roots of $g(x)$, which are assumed to be simple.

the outside, the sum (4.8) has only a single term and yields a finite value for G, but if we approach it from the inside, two of the t_j coalesce at an extremum of h and the equation yields a divergent value for G.

Recalling that $\mathbf{n} = \mathbf{R}/R = \mathbf{x_P} - \mathbf{x(t)}/R$, where $\mathbf{x(t)} = [r, \hat{\varphi} + \omega t, z]$ and $\mathbf{x_P} = [r_P, \varphi_P, z_P]$, we return to Equation (4.8) and find that

$$\begin{aligned} \left|\frac{\partial h}{\partial t}\right| &= |1 - r_P(r\omega/c)\sin(\varphi_P - \omega t)/R(t)| \\ &= |1 - \mathbf{n}\cdot\dot{\mathbf{x}}/c| \\ &= |1 - \boldsymbol{\beta}\cdot\mathbf{n}| \end{aligned} \tag{4.9}$$

Indeed,

$$G = q\sum_{t_{ret}}\left[\frac{1}{|1-\boldsymbol{\beta}\cdot\mathbf{n}|R}\right] = \Phi(\mathbf{x_P}, t_P).$$

Having verified that the potentials (4.3) are indeed fundamental causal solutions of Maxwell's equations, the Liénard-Wiechert fields of a point charge q travelling arbitrarily fast on a given trajectory $\mathbf{x}(t)$ as observed at space-time coordinates $(\mathbf{x_P}, t_P)$ can now be derived directly and may be given

$$\mathbf{E}(\mathbf{x}_P, t_P) = q\sum_{t_{ret}}\left[\frac{\mathbf{n}-\boldsymbol{\beta}}{\gamma^2|1-\boldsymbol{\beta}\cdot\mathbf{n}|^3R^2}\right] + \left[\frac{\mathbf{n}\times\{(\mathbf{n}-\boldsymbol{\beta})\times\dot{\boldsymbol{\beta}}\}}{|1-\boldsymbol{\beta}\cdot\mathbf{n}|^3cR}\right] \tag{4.10}$$

and $\quad \mathbf{B} = \mathbf{n}\times\mathbf{E}$.

Notice that, for a charge that moves faster than c, the Lorentz factor γ is complex, not real, as in the subluminal regime. As a result, the intensity of the radiation due to a superluminal source oscillates as a function of its frequency. This unique feature of faster-than-light sources explains, among others, the oscillations observed in the frequency spectrum of the Crab pulsar, which will be discussed briefly in Appendix A.2.3.

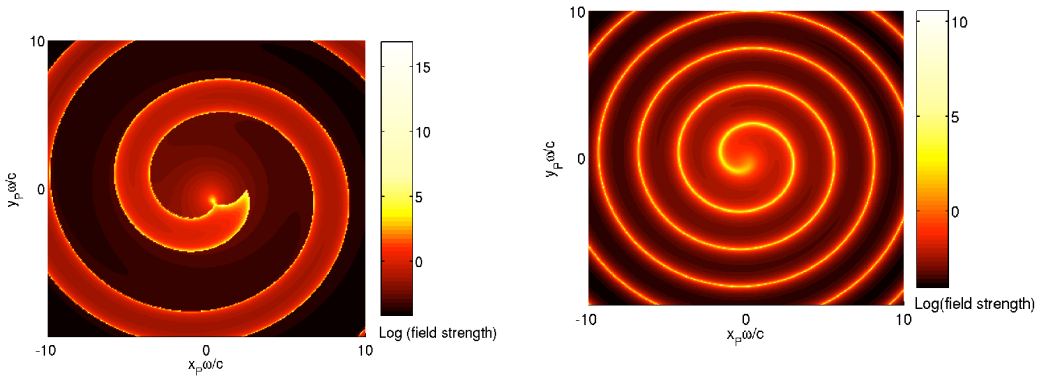

Figure 4.1: (left) Field strength in the plane of the source's orbit, for $\hat{r} = 2.5$. Note the high radiation intensity along the inner edges of the envelope and near the cusp. (right) Relative radiation intensity on the limiting cone of the cusp.

4.2 The Relation between Emission and Observer Time: An Old Problem Revisited

The evaluation of the radiation fields given in Equation (4.10) poses no difficulties once the number of retarded times t and their values have been determined. Hence, we must find the root(s) of function $h(t)$ (Eq. (2.17)), *i.e.,* solutions to the relation

$$t - t_P + c^{-1}[z_P^2 + r_P^2 + r^2 - 2r_P r\cos(\varphi_P - \omega t)]^{1/2} = 0, \tag{4.11}$$

which is transcendental.

For mathematical ease, if, again, at the cost of physical transparency, we introduce the Lagrangian variables $\hat{\varphi} \equiv \varphi - \omega t$ and $\hat{\varphi}_{\rm P} \equiv \varphi_{\rm P} - \omega t_{\rm P}$, capturing the rigid rotation of the patterns of the source and the radiation field [69]. Using distances scaled by units of light cylinders as introduced in Section 2.2, (2.16) becomes

$$\phi = h(\varphi) \equiv \varphi + \left[\hat{R}_P^2 + \hat{r}^2 - 2\hat{r}\hat{r}_P\cos(\varphi - \varphi_P)\right]^{1/2}, \tag{4.12}$$

where $\phi \equiv \hat{\varphi} - \hat{\varphi}_{\rm P}$ and $\hat{R}_{\rm P}^2 = \hat{z}_{\rm P}^2 + \hat{r}_{\rm P}^2$. A numerical difficulty with (4.12) is that a large (*e.g.,* astronomical) $\hat{R}_{\rm P}$ swamps the oscillations in the cosine term. We remedy

this by subtracting $\hat{R}_0 \equiv (\hat{R}_{\rm P}^2 + \hat{r}^2)^{1/2}$ from both sides, resulting in

$$\begin{aligned}\Delta\phi = \Delta h(\varphi) &\equiv \varphi + \hat{R}(\varphi) - \hat{R}_0 \\ &= \varphi - \frac{2\hat{r}\hat{r}_{\rm P}\sin\varphi}{(\hat{R}_0^2 - 2\hat{r}\hat{r}_{\rm P}\sin\varphi)^{1/2} + \hat{R}_0},\end{aligned} \tag{4.13}$$

where we have also chosen $\varphi_{\rm P} = -3\pi/2$ for convenience. In the limit that $\hat{R}_{\rm P} \to \infty$, this becomes

$$\Delta\phi = \varphi - \hat{r}\sin\theta_{\rm P}\sin\varphi, \tag{4.14}$$

which is of the form of Kepler's Equation[2] for elliptical orbits,

$$M = E - e\sin E. \tag{4.15}$$

Simply stated, Kepler's Equation relates the eccentric anomaly E, the mean anomaly M, and the eccentricity e in an elliptic orbit. It is, up to this day, of fundamental importance in celestial mechanics, but cannot be inverted directly to determine E – the angular parameter that defines the position of the body. Hence, despite its apparent simplicity, papers devoted to Kepler's Problem have appeared in virtually every decade from 1650 to the present, endowing it with an undeniable luster and allure for the modern practitioner, although a number of satisfactory solutions are long known. Peter Colwell's text [70] provides an excellent survey of the problem and its treatment over the centuries, beginning with early attempts by Kepler himself, [3] Newton, Euler, Gauss and Cauchy. Infinite series solutions – the

[2] What we call Kepler's Equation and Kepler's method of solving it appeared, in fact, in the ninth century writings of Habash-al-Hasib in connection with problems of parallax.

[3] Kepler's own solution can be summarized as follows: Given e and M, guess an approximate solution E_0 for E and calculate

$$M_0 = E_0 - e\sin E_0.$$

Let $E_1 = E_0 + (M - M_0)$ and calculate

$$M_1 = E_1 - e\sin E_1.$$

Then $E_2 = E_1 + (M - M_1)$ should yield a better approximation of E.

most elegant – use Lagrange's Theorem, Bessel functions and Levi-Civita as well as Lie series while modern treatments are due to Burniston and Siewert [71], Ioakimidis and Papadakis [72], and Delves and Lyness [73]. In our case, the "eccentricity" e is greater than one when multiple solutions for retarded times are possible, which is to say that the orbit is "nearly parabolic."[4]

The correspondence of Eq. (4.14) with Kepler's Equation brings to the fore the serious numerical difficulty in solving either of the transcendental equations (4.13) or (4.14): That e near one and M near zero results in severe subtractive cancellation [70]. In orbital mechanics, this special case of determining the eccentric anomaly near the pericenter of a near-parabolic orbit is usually merely a side issue, but for our superluminal sources, the analogous situation is a central concern: As described in Section 2.3, we are interested precisely in determining retarded times near the cusp of the envelope, which are the strongest contributors to the observed field. For typical pulsar observations, $\hat{r}\sin\theta_{\mathrm{P}}$ is very near indeed to unity. Close to the cusp, the increment above one is of the order of $\hat{R}_{\mathrm{P}}^{-2}$, with the scaled distances $\hat{R}_{\mathrm{P}}$ to pulsars being of order 10^9 to 10^{15}. The oscillatory region of g is correspondingly tiny: in radians, $\varphi_- - \varphi_+$ is of order $\hat{R}_{\mathrm{P}}^{-1}$, and $\phi_+ - \phi_-$, $\hat{R}_{\mathrm{P}}^{-3}$. *Hence, one of the central problems of the present thesis is one in numerical analysis: To find one or more solutions to Kepler's Equation near the pericenter of a near-parabolic orbit, where e is near one and M near zero.*

4.2.1 An Iterative Solution to Kepler's Equation

Whilst various numerical methods of approximation have been suggested to find the (usually sole) root of Kepler's Equation, most contemporary solutions are based on

[4] An elliptic or a hyperbolic orbit with eccentricity close to 1 is said to be "nearly parabolic." Convention holds that this this is the case if the boundary $\delta = |e - 1| \leq 0.01$.

an iterative algorithm developed by Newton and later refined by Raphson.[5]

Given a real-valued continuous function f, we wish to construct a sequence (x_i), using iteration, which converges to a solution of $f(x) = 0$. Newton's method for the solution of this problem is formally defined as

$$x_{i+1} = x_i - \frac{f(x_i)}{f'(x_i)}, \qquad i = 0, 1, 2, ..., \tag{4.16}$$

with prescribed starting value x_0, where we implicitly assume that $f\prime(x_k) \neq 0$ for all $k \geq 0$.

Hence, Newton's method is a simple iteration of the function

$$g(x) = x - f(x)/f'(x), \tag{4.17}$$

that, unlike other iterative approximation algorithms, requires the evaluation of both the function $f(x)$ *and* its derivative $f'(x)$ at arbitrary points x. Geometrically, it consists of extending the tangent line at a current point x_i until it crosses zero, then setting the next guess x_{i+1} to the abscissa of that zero-crossing.

The power of Newton's method lies in its rate of convergence, which is quadratic, where quadratic convergence of a sequence is defined as follows:

Suppose that $\xi = \lim_{i\to\infty} x_i$. We say that the sequence (x_i) converges to ξ *with at least order* $q > 1$, if there exists a sequence (ϵ_i) of positive real numbers converging to 0, $\mu > 0$, such that

$$|x_i - \xi| \leq \epsilon_i, \qquad i = 0, 1, 2, ..., \qquad \text{and} \qquad \lim_{i\to\infty} \frac{\epsilon_{i+1}}{\epsilon_i^q} = \mu. \tag{4.18}$$

If (4.18) holds with $\epsilon_i = |x_i - \xi|$ for $i = 0, 1, 2, ...$, then the sequence (x_i) is said to converge to ξ *with order* q. In particular, if $q = 2$, the sequence (x_i) is said to converge to ξ *quadratically*.

[5] For an exhaustive list of references, see [70].

Taylor's theorem states that any function $f(x)$ which has a continuous second derivative can be represented by an expansion about a point that is close to a root of $f(x)$. Suppose this root is ξ. Then the expansion about x_i is of the form

$$f(\xi) = f(x_i) + f'(x_i)(\xi - x_i) + R, \tag{4.19}$$

where the Lagrange form of the remainder R is

$$R = \frac{1}{2!} f''(\chi_i)(\xi - x_i)^2, \tag{4.20}$$

with $x_i \leq \chi_i \leq \xi$.

Since ξ is a root, (4.19) assumes the form

$$f(\xi) = 0 = f(x_i) + f'(x_i)(\xi - x_i) + \frac{1}{2} f''(\chi_i)(\xi - x_i)^2. \tag{4.21}$$

Rearranging and dividing Equation (4.21) by $f'(x_i)$ gives

$$\frac{f(x_i)}{f'(x_i)} + (\xi - x_i) = -\frac{f''(\chi_i)}{2f'(x_i)}(\xi - x_i)^2. \tag{4.22}$$

Recalling that x_{i+1} is defined by (4.16), we find that

$$\underbrace{\xi - x_{i+1}}_{\epsilon_{i+1}} = -\frac{f''(\chi_i)}{2f'(x_i)} \underbrace{(\xi - x_i)}_{\epsilon_i}^2, \tag{4.23}$$

that is,

$$\epsilon_{i+1} = -\frac{f''(\chi_i)}{2f'(x_i)} \epsilon_i^2. \tag{4.24}$$

Taking absolute values on both sides yields

$$|\epsilon_{i+1}| = \frac{|f''(\chi_i)|}{2|f'(x_i)|} \epsilon_i^2, \tag{4.25}$$

which shows that the rate of convergence is quadratic. As in (4.16) above, we require that $f'(x) \neq 0 \quad \forall x \in I$, where I is the interval $[\xi - r, \xi + r]$ for some $r \geq |(\xi - x_0)|$, and that $f''(x)$ be finite $\forall x \in I$. Furthermore, the prescribed starting value x_0 needs to be *sufficiently close* to the root.

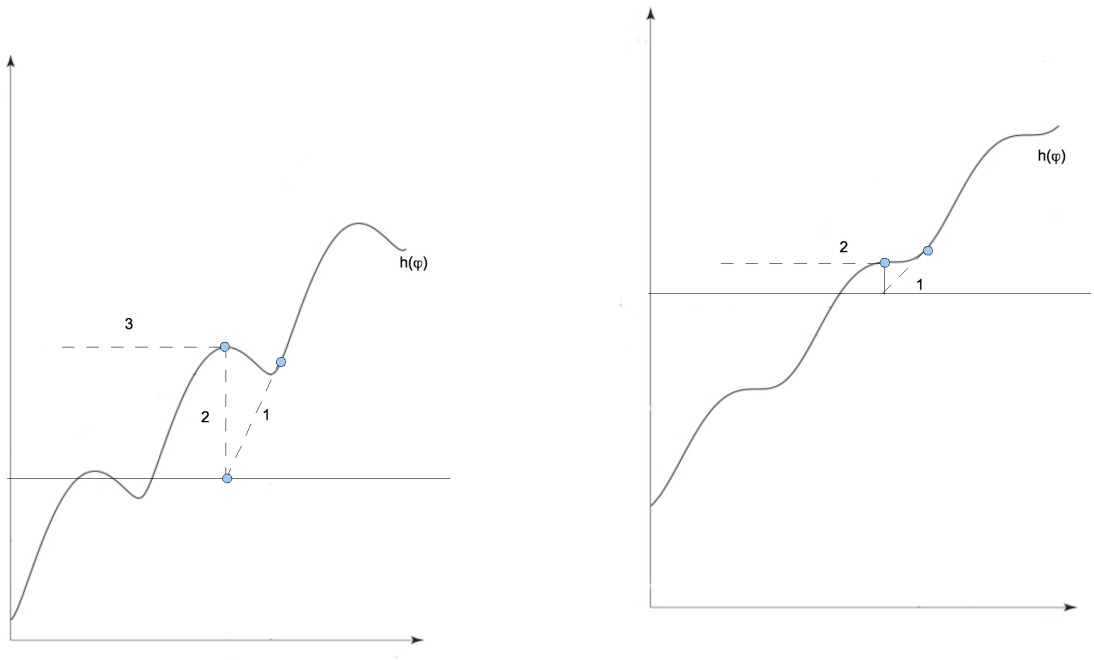

Figure 4.2: Pathological cases in which Newton's method as applied to (4.14) will fail to converge. Carefully chosen bracketing bounds and the insertion of a bisection step whenever Newton-Raphson would take the solution out of bounds prevent calamities such as these.

While Newton's method has very attractive local convergence properties, its global behavior can be complicated and erratic [74–77]. Many texts in numerical analysis include detailed studies of pathological cases, where the algorithm yields grossly inaccurate, meaningless corrections, enters a nonconvergent cycle or attempts to locate a root at infinity [74–77]. While a formal analysis of the Newton-Raphson formula as applied to Kepler's equation for nearly parabolic orbits is beyond the scope of this work, we include two examples (Figure 4.2) which illustrate how the procedure will fail to locate the roots of (4.14) if the starting values φ_0 are ill-chosen.

Since the global convergence properties of Newton's method are rather poor, it is necessary to design routines that i) guard against the method making inappropriate

corrections while ii) ensuring that rapid convergence be maintained. The former is achieved fairly easily by utilizing a combination of bisection and the Newton-Raphson formula as suggested in [78]. The hybrid algorithm takes a bisection step whenever the Newton-Raphson procedure would take the solution out of bounds or is not reducing the bracket size – the extent of the region around the function's crossing of the abscissa – swiftly enough. A full listing of the algorithm is given in Section 4.4. The latter, namely to bracket the roots such that few bisection steps need to be taken and quadratic convergence remains ensured, requires more diligence and ingenuity.

The first step is to assess the characteristic combination of emission and observation time for each individual point of the radiated field, *i.e.,* to determine whether the observer is located inside, on the cusp of, or outside the envelope. To this end we evaluate the difference $\Delta \equiv (\hat{r_P}^2 - 1)(\hat{r}^2 - 1) - \hat{z_P}^2$ (Eq. (2.21)). If this is nonpositive, then h is nonoscillatory and we have a single zero of $h(t) - t_P$ somewhere on the closed interval bounded by $t_P - c^{-1}(r^2 + r_P^2 + z_P^2 \pm 2rr_P)^{1/2}$ We may employ Newton's method as outlined and modified above or any other numerical procedure that locates a single root on a continuous interval. If, on the other hand, Δ is positive, there may be multiple retarded times, each bracketed by a sequence of adjacent local extrema with alternating signs (or zero). Using (2.20), we locate the greatest minimum $h(t_{min_0})$ not exceeding t_P and the least minimum $h(t_{min_k})$ greater than t_P. Then the extrema of h between $h(t_{min_0})$ (inclusive) and $h(t_{min_k})$ (exclusive) delimit a sequence of monotonic intervals, each of which contains a single zero of $h(t) - t_P$, and we apply our numerical root-finder to each of these. The full algorithm for this bracketing routine is listed in Section 4.4.

Whilst the approach described above is sufficiently accurate for terrestrial distances, difficulties arise if we move to astronomical length scales, especially if we wish to determine the eccentric anomaly near the pericenter of the nearly parabolic orbit, as outlined above. (The closest known pulsar to Earth is PSR J0108-1431 in

the direction of the constellation Cetus, at a distance of about 85 parsecs or 280 light years from the sun.)

Our solution to finding retarded times in this critical region is to precisely locate the turning points (φ_+, ϕ_+) and (φ_-, ϕ_-) of h using multiple-precision arithmetic and approximate $\Delta\Phi$ in this region by a cubic interpolating the turning points and matching the zero derivatives at those points. We find that this cubic is typically a good approximation to $\Delta\Phi$ over a range several orders of magnitude larger than $\varphi_- - \varphi_+$, and it can be directly inverted to yield three real roots for $\phi_- < \phi < \phi_+$ or one elsewhere. Beyond this range, $\Delta\Phi$ is well enough behaved that, starting from a linear first approximation to the root, Newton's modified iteration method will converge quickly. There may be other regions of the parameter space, however, where a more involved interpolation technique will be needed to produce a root or a first approximation. However, it appears that approximating the Kepler function by a cubic Hermite spline with knots at multiples of π or $\pi/2$ might be a viable approach to solving Kepler's problem in the near-parabolic case.

4.3 Discussion of Results

Having evaluated the relevant retarded times using the methods described above, Eq. (4.10) is summed numerically to yield the Liénard-Wiechert fields at space-time points $\mathbf{x_P}, t_P$. [6] The radiated electric field thus produced has an orientation, or polarization, that changes rapidly with time and location. In addition to visualizing $|\mathbf{E}|^2$, which is proportional to the average power in the radiated fields, we will employ Stokes parameters, which provide a description of the polarization state of electromagnetic radiation and are widely used in the analysis of astronomical data (see, *e.g.,* pp. 25–37 of [81]). Named after Sir George Stokes (1819–1903), these

[6] The results described below were published in part as [54].

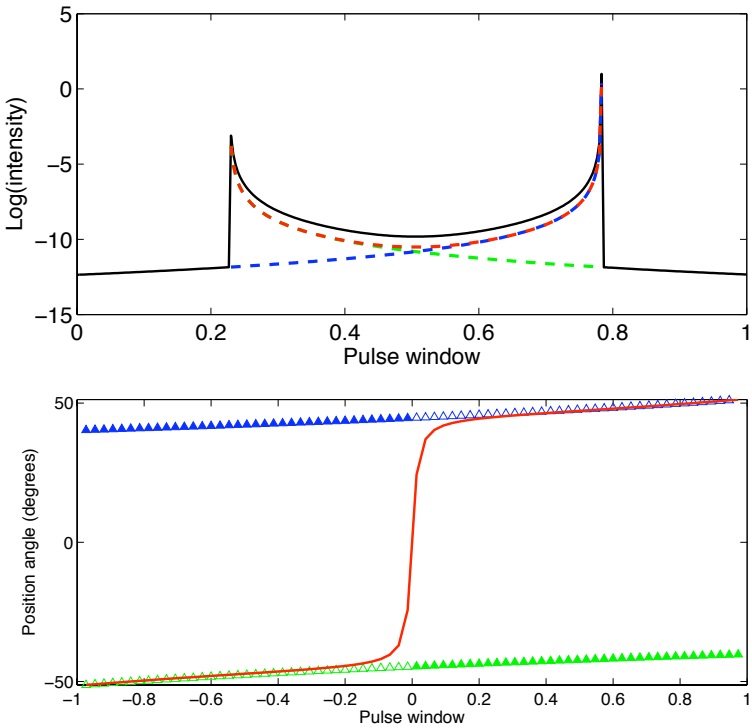

Figure 4.3: (Top) The relative strengths of the three radiation modes (green, red, blue) and the total field (black) as experienced by an observer inside the envelope (*e.g.*, $\theta_{P_C} < \theta_P < 180^\circ - \theta_{P_C}$) near the cusp on a sphere of large radius. Note that the contribution from the third retarded time (green) is much stronger than that from the first (blue) near the beginning of the pulse, with these rôles reversed near the end. Furthermore, two of the contributions are stronger than the third everywhere except in the middle of the pulse. (Bottom) Position angle of the contributions from the three retarded times (green, red, and blue triangles) are shown relative to one another for the same source and observation arc as above. The position angles of the dominant contributions are shown with open, those of the weakest contributions with filled triangles. Note that the position angle of the second contribution (red) closely follows the average position angle, bridging the first and third contributions.

quantities are defined as

$$I = |\mathbf{E}_\parallel|^2 + |\mathbf{E}_\perp|^2 \qquad \frac{U}{I} = \frac{2|\mathbf{E}_\parallel/\mathbf{E}_\perp|\cos\delta}{|\mathbf{E}_\parallel/\mathbf{E}_\perp|^2+1} \tag{4.26}$$

$$\frac{Q}{I} = \frac{|\mathbf{E}_\parallel/\mathbf{E}_\perp|^2-1}{|\mathbf{E}_\parallel/\mathbf{E}_\perp|^2+1} \qquad \frac{V}{I} = \frac{2|\mathbf{E}_\parallel/\mathbf{E}_\perp|\sin\delta}{|\mathbf{E}_\parallel/\mathbf{E}_\perp|^2+1,}$$

where the subscripts $\parallel$ and $\perp$ denote directions parallel and perpendicular to an axis chosen to be in the plane transverse to the direction of light propagation given by $\mathbf{S} = \mathbf{E} \times \mathbf{H}$. The parameter δ is the phase difference, at the frequency of interest, between $\mathbf{E}_\parallel$ and $\mathbf{E}_\perp$. In visualizing and discussing the results of Eq. (4.10), we will use the following:

$$\begin{aligned} &\text{degree of circular polarization:} && \frac{V}{I} \\ &\text{degree of linear polarization:} && \frac{L}{I} = \frac{\sqrt{Q^2 + U^2}}{I} \\ &\text{and} \\ &\text{polarization position angle:} && \frac{1}{2} \tan^{-1} \frac{U}{Q}, \end{aligned} \tag{4.27}$$

which is also the standard procedure of depicting pulsar data [82]. Typical results for $I \propto |\mathbf{E}|^2$ are shown in Figure 2.6, for the plane of the source's orbit (left), and for the limiting cone of the cusp (right), $\theta_P = \sin^{-1} c/v$. The former clearly shows that most of the radiated energy is confined within the boundaries of the Čerenkov envelope, most notably its edges, as well as regions near the cusp (compare with Fig. 2.7). The intensity on the cone that approaches the cusp curve asymptotically from the outside as $R_P \to \infty$ (Fig. 4.1, right) falls off almost imperceptibly with increasing distance (as expected, see Section 2.3). As this region of high electromagnetic intensity spirals out and into the far-field, it will sweep past an observer once for every rotation of the source, delivering a powerful pulse of light. This is in exact correspondence to the sharp "spikes" observed in the temporal focusing plots of Figure 2.9 (left) and (center).

Since the field of the rotating source itself rotates rigidly, an observer at spherical coordinates $(R_P, \varphi_P, \theta_P)$ samples, during each rotation period, the field on the arc that lies at the intersection of the cone $\theta_P =$ constant and the sphere $R_P =$ constant. For the limiting cone of the cusp, this arc lies partly inside and partly outside the envelope. Owing to the discontinuous change in the strength of the field across

the envelope, the intensity of the radiation received along this curve has a pulsed distribution consisting of two sharply peaked components; the closer the opening angle of the cone to $\sin^{-1} c/v$, the smaller the width of this two-component pulse, until, on the cusp itself, the two peaks combine to form a single flash of light.

Moving off the cusp further into the volume enclosed by the two sheets of the envelope, (*e.g.,* $\theta_{P_C} < \theta_P < 180^\circ - \theta_{P_C}$), the temporal focusing calculations (see Figure 2.10) would lead one to expect three retarded contributions. This is indeed shown in Fig. 4.3, which depicts the time dependence (in units of the pulse window [7]) of the intensity from each of these retarded time contributions. The total yields a double-peaked structure connected by a saddle, which is very reminiscent indeed of the temporal focusing calculations for a similar location (Fig. 2.10). Thus, the "light curve" of the pulses can be seen to reflect the degree of temporal focusing directly.

The polarization characteristics of the emitted radiation are probably most easily grasped by following the example of observational astronomers and calculating the Stokes parameters, in particular the polarization position angle. The bottom panel of Figure 4.3 shows the position angles of the contributions from the three retarded times across the pulse window, where open triangles donote the dominant, closed ones the weakest contributions, respectively. Two of the radiation modes remain approximately parallel to each other for the duration of the pulse, displaying very little change in their position angles. The third contribution, however, closely follows the average position angle, bridging the remaining two in an S-shaped curve. Figure 4.4 shows similar plots for several observer locations in the range $\theta_{P_C} < \theta_P < 180^\circ - \theta_{P_C}$, which reveal that the position angles of the three radiation modes are mirror-symmetrical about the plane of rotation ($\theta_P = 90^\circ$); the position angles of the two contributions depicted in green and blue reverse signs, while the position angles of the third retarded-time component reverses its direction of swing.

[7] The pulse emission from pulsars is usually confined to a time span of a few per cent of the pulsar period – the "pulse window".

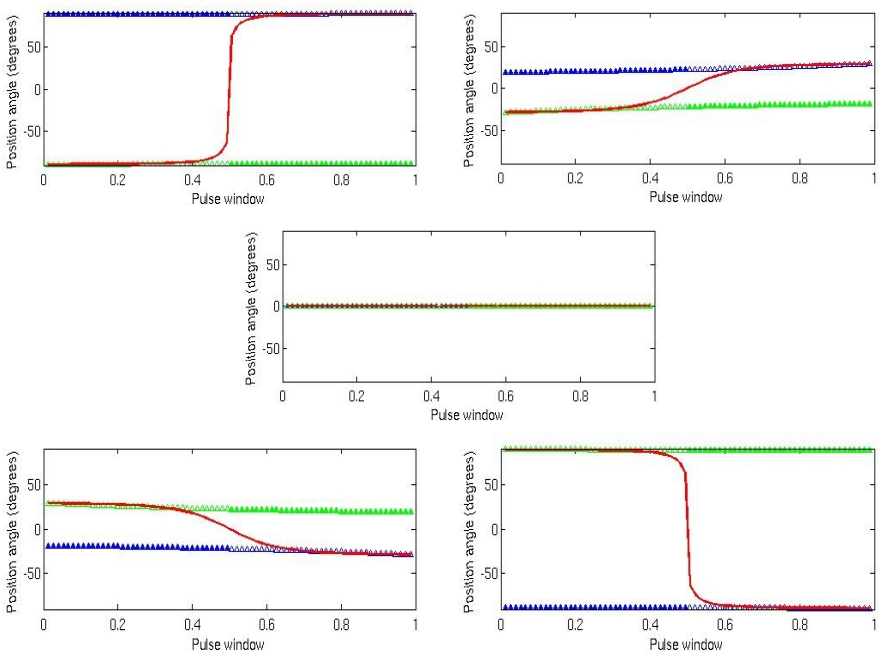

Figure 4.4: Position angle of the contributions from the three retarded times (green, red, and blue triangles) for several observer locations in the range $\theta_{P_C} < \theta_P < 180° - \theta_{P_C}$. The position angles of the three radiation modes are mirror-symmetrical about the plane of rotation ($\theta_P = 90°$); the position angles of the two contributions depicted in green and blue reverse signs, while the position angles of the third retarded-time component reverses its direction of swing.

The polarization position angles for the entire field, scaled by their intensity, are shown in Figure 4.5. The aesthetically pleasing, filigreed structure seems organic in its appearance, showing that the relative directions and sizes vary only subtly over the duration of a pulse.

The numerical valuations of the temporal focusing factor as well as the Liénard-Wiechert fields of a localized source in superluminal rotation show a consistent set of intrinsic characteristics. A formal summary of the numerical data in Figures 2.9 to 4.5 inclusive may be given as follows:

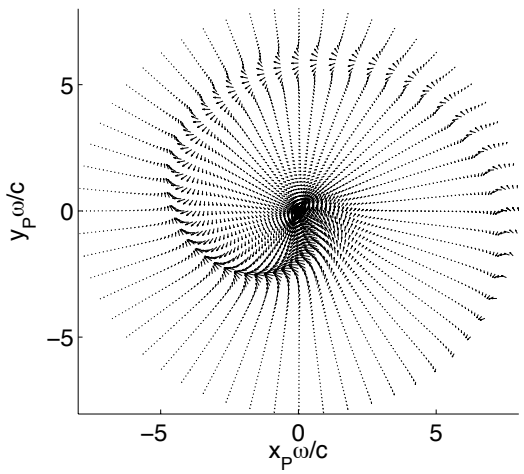

Figure 4.5: Polarization position angles and intensities for the same source as depicted in Fig. 4.1 (right). The arrows represent the direction and magnitude of the electric field for a given field point.

(i) The radiation is sharply focused along a narrow, rigidly rotating spiral-shaped beam that embodies the cusp of the envelope of the emitted wave fronts.

(ii) For moderately superluminal sources, it consists of either one or three concurrent polarization modes (depending on the position of the observer relative to the cusp) that arise from contributions to the field from differing retarded times.

(iii) At each edge of the pulse, two of the modes are comparable in strength, dominating over the third. Near the middle of the pulse, the three modes are of comparable strength (Fig. 4.3).

(iv) The position angle of one of the modes, as well as that of the total field, swings across the beam by as much as 180°, while the position angles of the other two modes remain approximately orthogonal throughout their excursion across the beam (Fig. 4.5).

(v) One of the three modes is highly circularly polarized and differs in its sense of polarization from the other two.

(vi) Two of the modes are highly linearly polarized across the entire pulse.

In Appendix A, we will see how these predictions relate to astronomical observations of highly magnetized, rotating stellar remnants, and thereby justify the superluminal model as a viable explanation for observational pulsar data.

4.4 Listing of Algorithms

```
1 function [solns]=find_t(r,r_p,fi_p,z_p,t_p)
2 %Finds solutions to the equation t_P=h(t)=t+R(t)/c
3 %Synopsis: [solns] = find_t(r,r_p,fi_p,z_p,t_p)
4 %
5 %Input:                  r = the radius of source point x
6 %         r_p, fi_p, z_p = the cylindrical polar coordinates of
7 %                          observationpoint x_P
8 %                    t_p = observation time
9 %Output:             solns = solutions to the equation t=t_P-R(t)/c
10
11 global a b hb;
12 a=z_p^2+r_p^2+r^2;
13 if r_p == 0.0  %degenerate case: observer on z-axis
14   solns = [t_p-sqrt(a)];
15 else
16   hb = r_p*r;
17   b = hb+hb;
18   %Determine if h is oscillatory, that is, if there are distinct
```

```
19  %real roots in cos(\varphi-t) to dh/dt = 0:
20    d=(r_p^2-1)*(r^2-1)-(-z_p)^2;
21  if d <= 0 % nonoscillatory
22  % h is monotonically increasing.  The single root lies
23  % between t_p-sqrt(a[-+]b) inclusive.
24    solns = findRoot('find_th0',t_p-sqrt(a+[b,-b]));
25    else  % oscillatory
26    %The roots (possibly multiple) are bracketed by a
27    %sequence of adjacent local extrema with alternating signs
28    %(or zero).
29    q = 1 + sqrt(d);
30    %local maximum,minimum
31    extremum = fi_p - acos([(a/hb-hb)/q,q/hb]);
32    h0 = find_th0(extremum);
33    %Find the first local maximum >= 0.
34    %Back up to the previous minimum.
35    twopi = 2*pi;
36    k = floor(h0(1)/twopi);
37    delta = twopi*[k,k+1];
38    extremum = extremum - delta;
39    h0 = h0 - delta;
40    i = [2 1];
41    solns = [];
42    while sign(h0(1)) ~= sign(h0(2))
43    % the extrema bracket a zero
44      if h0(i(2)) == 0
45      % the extremum is a double root
46        solns = [solns,extremum(i(2))];
47        % Advance two intervals.
48        extremum = extremum + twopi;
```

```
49          h0 = h0 + twopi;
50        else
51          solns = [solns,findRoot('find_th0',extremum(i))];
52          % Advance one interval.
53          extremum(i(1)) = extremum(i(1)) + twopi;
54          h0(i(1)) = h0(i(1)) + twopi;
55          i = i([2 1]);
56        end
57      end
58    end
59 end
60
61 function xr = findRoot(fun,xb)
62 %Using a combination of Newton-Raphson and bisection,
63 %findRoot finds the root of a function bracketed between
64 %xb(1) and xb(2). The root, returned as function value xr,
65 %will be refined until the step does not change the estimate.
66 % fun is a user-supplied subroutine which returns both the
67 %functionvalue and the first derivative of the function.
68 %Synopsis:        xr   = findRoot(fun,xb)
69 %
70 %Input:           fun  = (string) name of a matlab external
71 %                        function
72 %                 xb   = vector of bracket endpoints
73 %Output:          xr   = root (or singularity) of the function
74 %                        in xb
75
76 MAXIT=100;  %Maximum number of iterations allowed
77 %Evaluate the user-supplied subroutine at the bracket endpoints
78 yb = feval(fun,xb);
```

```
79 %Determine if an endpoint is exactly zero
80 z = find(yb==0,1);
81 if ~isempty(z)
82    xr = xb(z);
83    return
84 end
85 %Guard against empty brackets
86 if prod(yb) > 0
87    error('Root must be bracketed in findRoot.');
88 end
89 %Orient the search such that f(xb(1))<0.
90 if yb(1) > 0
91    xb = xb([2 1]);
92 end
93 dxold = diff(xb); %the penultimate step size
94 dx = 0.5*dxold; %the last stepsize
95 xr = xb(2); %the last estimate
96
97 for j=1:MAXIT
98    xrold = xr;
99    xr = xr - dx;
100   if xr == xrold
101      return
102   end
103   [f,df]=feval(fun,xr);
104   xb((f>=0)+1) = xr; %maintain the bracket.
105   %Bisect if Newton out of range or not decreasing fast enough.
106   if prod((xr-xb)*df-f) >= 0 | abs(2*f) > abs(dxold*df)
107      dxold = dx;
108      dx = xr - 0.5*sum(xb);
```

```
109    else                                %Newton step acceptable
110      dxold = dx;
111      dx = f/df;
112    end
113 end
114 warning('findRoot has exceeded maximum iterations.')
```

Chapter 5

Conclusions and Future Studies

In this thesis, we studied the emission of a polarization-current element of infinitesimal volume in constant superluminal rotation. We set out by applying basic methods introduced by Huyghens and Fresnel to gain phase information and found that radiation sources that travel not only faster than light, but are also subject to acceleration, possess a two-sheeted envelope and a cusp – a region of intense concentration of energy. Moreover, we carefully analyzed the relationship between emission and observation time, which need not be monotonic and one-to-one, as multiple retarded times – or even extended periods of source time – can contribute to a single instant of reception. This unusual temporal relation is of the form of Kepler's equation for elliptical orbits, which is of fundamental importance in celestial mechanics, but cannot be inverted directly to determine the position of the body. The numerical difficulty in finding one or more solutions to Kepler's problem near the pericenter of a near-parabolic orbit was solved by implementing an iterative algorithm developed by Newton and later refined by Raphson. This enabled us to analyze the electromagnetic effects associated with the unusual temporal relation between source and observer quantitatively using a "measure" that we christened the "temporal focusing factor." Not surprisingly, it was found that intriguing phenomena occur on the cusp

and within the envelope of the emitted wave fronts. To investigate these unusual features further, we proceeded to calculate the more sophisticated Liénard-Wiechert potentials and fields for these locations, thereby introducing amplitude in addition to phase information. Since integral solutions to Maxwell's equations, derived in the context of stationary or subluminally moving sources, can be inconvenient in treating faster-than-light charges due to the presence of multiple or extended retarded times, we derived what constitutes the main, substantive part of the present work: The correct *formulae* for the Liénard-Wiechert potentials and fields of a point charge travelling arbitrarily fast along a given trajectory. Once found, these expressions were numerically evaluated and the results visualized.

Whilst many features are already clarified by this point-like source, further development will require the introduction of a source that has finite extent. One possible method would be to consider summation over a volume distribution of discrete, point-like sources; alternatively, one could try to develop the integration of a continuous function. However, owing to the complexity of the problem, any such calculation will involve numerical processing, which always implies some form of discretization. Hence, both approaches ultimately involve discrete sums, but over different lengthscales. This is an intriguing problem, because a macroscopic polarization current is, by its nature, an extended object, as is required for a superluminal source. However, if one looks on a sufficiently small (*e.g.,* atomic) lengthscale, the polarization no longer appears like a continuous distribution, but instead consists of a volume distribution of discrete dipoles (atoms and ions). Over such distances, the assumptions of the superluminal model may be in question. Once an extended source model is developed, quantitative model comparisons with the point source model can be made, as well as possible implications for pulsars studied.

An important feature of future work will be the issue of mathematical rigor since most computations in the present thesis are of a formal nature only. Rigor can be

achieved rather easily since the initial value problem for the inhomogeneous wave equation is well understood for all sources and all initial data mentioned in this work. Moreover, the initial value problem for Maxwell's equations can be treated by simple corollaries to the theorems for the initial value problem of the inhomogeneous wave equation.

In fact, there exist existence/uniqueness theorems for the initial value problem of the inhomogeneous wave equation for all sources and all initial data mentioned. For example, in the case of smooth source data and smooth initial data we already introduced an existence/uniqueness theorem from [61] and applied it in Section 3. In the case of nonsmooth source data and/or nonsmooth initial data one has at one's disposal an existence/uniqueness theorem where the initial data are distributions in $D'(\mathbb{R}^3)$ and the source data and solution are distributions in $D'(\mathbb{R}^4)$ (details on the initial value problem of the inhomogeneous wave equation for D' distributions can be found for example in [79, 80]). Indeed, all initial data mentioned in the present work are in $D'(\mathbb{R}^3)$ and all source data are in $D'(\mathbb{R}^4)$ whence the above mentioned existence/uniqueness theorem applies for all data used throughout this thesis. Using D' distributions the inhomogeneous wave equation reads as

$$\nabla^2 \hat{\Psi} - \frac{\partial^2 \hat{\Psi}}{\partial t^2} = \hat{S} \,, \tag{5.1}$$

where $\hat{S}$ is a distribution in $D'(\mathbb{R}^4)$ which contains the source data and the initial data. The above mentioned existence/uniqueness theorem says that (5.1) has exactly one solution $\hat{\Psi}$ in $D'(\mathbb{R}^4)$ whose support is a subset of $\{(\mathbf{x}, t) : \mathbf{x} \in \mathbb{R}^3, t \geq 0\}$. Most importantly this unique solution has the form

$$\hat{\Psi} = -\hat{G} * \hat{S} \,, \tag{5.2}$$

where $\hat{G}$ is that distribution in $D'(\mathbb{R}^4)$ which corresponds to Green's function G and where $*$ denotes the convolution in $D'(\mathbb{R}^4)$. Note that the convolution $\hat{G} * \hat{S}$ is, by

being a convolution of D' distributions, not a convolution of functions. Thus every formal computation which treats $\hat{G}, \hat{S}$ as functions has to be taken with a grain of salt (and this, in turn, is one reason why D' distributions are important in our context). Although the definition of $*$ in $D'(\mathbb{R}^4)$ is slightly more intricate than the convolution of functions, computations with $\hat{G} * \hat{S}$ are not necessarily more intricate than those for functions, especially so, when $\hat{S}$ contains the delta distribution. In the case where the source and initial data are not only D' distributions but regular distributions in D', i.e., distributions which can be represented by locally integrable functions (e.g., smooth functions), one has an existence/uniqueness theorem where the unique solution $\hat{\Psi}$ is a regular distribution in $D'(\mathbb{R}^4)$, i.e., can be represented by a locally integrable function. In that case the convolution $\hat{G} * \hat{S}$ can be written as an integral over functions. In particular Equation (3.2) covers the smooth subcase.

Note finally that all theorems mentioned above don't care if the source data are subluminal or superluminal. However as this work indicates, the solutions for superluminal sources can differ appreciabely from those for subluminal sources.

Appendix A

The Superluminal Model of Pulsar Emission

In what is to follow, we compare the findings of the previous chapters to the radiation emitted by pulsars, rapidly rotating, highly magnetized neutron stars, and find that virtually all of the enigmatic features of their radiation can be explained using a single, elegant model with few input parameters and no external assumptions. Although physical and heuristic – rather than mathematical – in nature, these results have been included in the present thesis, as they demonstrate that superluminal emission is almost certainly an ubiquitous process in the observable universe and may, therefore, be of importance for the astronomical and astrophysical communities.

A.1 Pulsars 101

A.1.1 The Discovery of Pulsars

Soon after Jocelyn Bell, quite serendipitously, discovered the first pulsars in the Summer of 1967 [88], Pacini [89,90] and Gold [91,92] suggested independently that rapidly rotating, highly magnetized neutron stars must be responsible for the observed radio pulses since "no other theoretically known astronomical object would possess such short and accurate periodicities [91]." This insight provided an entirely unexpected verification of a proposal made more than 30 years earlier by Walter Baade and Fritz Zwicky [93], who suggested the existence of a new form of star, namely the neutron star, which would be the end point of stellar evolution. In 1934 the two astronomers wrote [93]:

> "...with all reserve we advance the view that a supernova represents the transition of an ordinary star into a neutron star, consisting mainly of neutrons. Such a star may possess a very small radius and an extremely high density."

However, since such a neutron star would likely be small, cold, inert and emit preciously little light, their conjecture seemed, at the time, beyond the possibility of actual astronomical verification.

In his seminal letter to *Nature*, Gold also pointed out that pulsar emission per unit emitting volume must be exceptionally high, since "the size of the region emitting any one pulse can, after all, not be much larger than the distance light travels in the few milliseconds that represent the lengths of the individual pulses," and that rotational energy must be lost through magnetic dipole radiation, such that the pulsar would appreciably "spin down" with age [91]. Subsequent measurements confirmed that the period of the Crab pulsar lengthenes uniformly by $36.48 \pm 0.04ns$ per day, *i.e.,* by over $1\mu s$ per month [94]. This rate of change is not only consistent with the known age of the Crab nebula, thus confirming the association of the pulsar with the

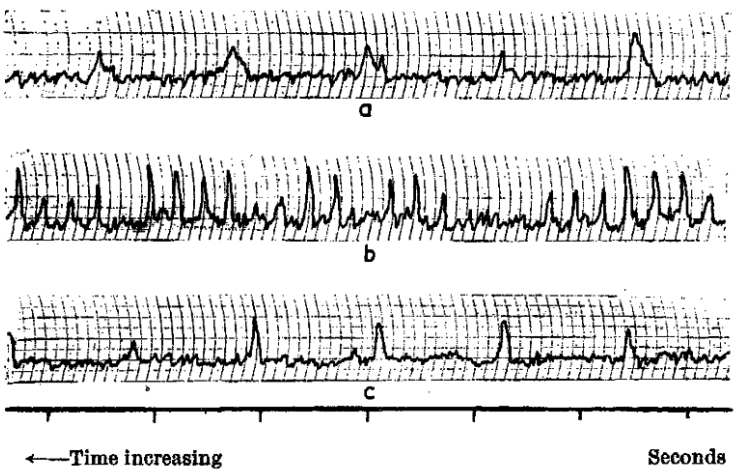

Figure A.1: Discovery observations of pulsating radio sources recorded by Jocelyn Bell in July 1967 [88].

supernova observed in AD 1054 (Fig. A.3), but also provides sufficient energy for the excitation of the synchrotron radiation that continuously emanates from the nebula itself [92]. Soon thereafter, Goldreich and Julian [95] concluded that, in spite of their intense surface gravity, rotating magnetic neutron stars "cannot be surrounded by a vacuum," but must possess a "dense magnetosphere." The particle density within this "plasma atmosphere" can be approximated by

$$n_{GJ} \equiv n_- - n_+ = 7 \times 10^{-2} B_z P^{-1} cm^{-3}, \tag{A.1}$$

where n_{GJ} is known as the Goldreich-Julian density, B_z is the axial component of the magnetic field in Gauss, and P is the period in seconds [95].

In January 1969, a small team at the Steward Observatory in Arizona observed optical pulsations emanating from the Crab pulsar, confirming the possibility that rotating neutron stars might emit pulses of light as well as radio waves [96], and two rocket flights, launched shortly thereafter by a team at the Naval Research Laboratory in Washington [97] and the Massachusetts Institute of Technology [98], respectively, showed that the Crab's frequency spectrum extends into the X- and

gamma-ray regions.[1]

45 years after their initial discovery, the catalogue of known pulsars, observed by numerous ground-based and orbiting telescopes, has grown to more than 1500 identified sources. Yet, many of the intrinsic characteristics of spinning neutron stars have remained mysterious and seemingly impervious to human analysis. Most noticeably, neither the location of the source of the emision within the pulsar magnetosphere nor the mechanism that produces it have been unambiguously identified, a quandary which caused eminent pulsar astronomer Jean Eilek from NRAO to exclaim in frustration, "We know why they pulse. But why do they shine? " [2]

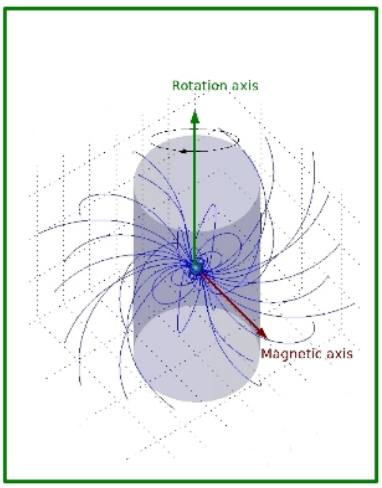

Figure A.2: Schematic representation of a pulsar. (Credit: P. Volegov, LANL)

A.1.2 The Physics of Neutron Stars

A pulsar is born when a massive star exhausts its supply of fuel and, without the opposing force of fusion to balance gravity, collapses in a powerful and violent supernova explosion.[3] What is left behind is a ball of tightly-packed neutrons which

[1] X-radiation is absorbed by the Earth's atmosphere; hence, instruments to detect X-rays must necessarily be taken to high altitude by balloons, sounding rockets, and satellites. Since there was no X-ray telescope orbiting the Earth in 1969, the only possibility lay in rocket flights.

[2] Jean Eilek, 2006, personal communication.

[3] The supernova explosion that created the Crab nebula and its central pulsar in AD 1054 was visible on Earth at high noon, and remained discernible during daylight for 23 days. The appearance of a very bright "guest star" in the constellation Taurus was recorded by Chinese and Japanese astronomers around July 4, 1054 and was noticed by Anasazi Indians as evidenced by petrographs in Navajo Canyon and White Mesa (both

Figure A.3: Left: The Crab pulsar, a city-sized, magnetized neutron star spinning 30 times a second, lies at the center of this composite image of the Crab Nebula, which combines optical data (red) from the Hubble Space Telescope and X-ray images (blue) from the Chandra Observatory. Right: Petrographs in Chaco Canyon depicting Supernova 1054 (now Crab nebula) above and Halley's comet below.

is only about 20 kilometers in diameter but contains most of the progenitor's core – about 1.5 to 2 solar masses – which makes neutron stars the most compact objects in the observable universe apart from black holes.[4] Due to conservation of angular momentum these neutron balls rotate rapidly, with spin periods ranging from 1.4 milliseconds to about eight seconds.

Pulsars are extraordinarily luminous. Their brightness temperature, given by

$$T_b = c^2 S_\nu (2k_B \nu^2 \Omega)^{-1}, \tag{A.2}$$

where S_ν is the measured flux[5] at frequency ν, Ω the opening angle of the source as seen from the Earth, and k_B denoes the Boltzmann's constant, is generally be-

AZ) as well as in the Chaco Canyon National Park (NM) (Fig. A.3).

[4] Indian astrophysicist Subrahmanyan Chandrasekhar showed that the theoretical upper limit to the mass of a white dwarf star – the "Chandrasekar limit" – is approximately 1.4 solar masses. Above this limit, degenerate electron pressure is insufficient to prevent gravity from collapsing the star further to become a neutron star. If the Oppenheimer-Volkoff limit, generally believed bo be about 2 to 3 solar masses, is exceeded as well, the collapse will result in a black hole.

[5] Flux (or radiant flux), S, is the total amount of energy that crosses a unit area per unit time. Flux is measured in Joules per square meter per second (Joules/m^2/s), or Watts per square meter (Watts/m^2).

tween 10^{25} and $10^{30}K$, but can be as high as $10^{39}K$. The central neutron star is surrounded by a "plasma atmosphere" – the magnetosphere – through which a magnetic field of extraordinary strength (at the order of 10^7 to 10^{11}Tesla) rotates.

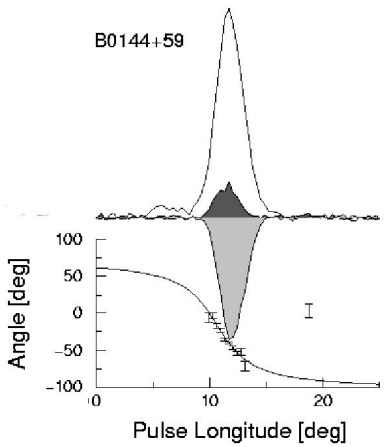

Figure A.4: Light curves, circular (light gray) and linear (dark gray) polarization, and polarization position angles for PSR B0144+59.

The electromagnetic waves emitted by pulsars are broadband with frequencies extending over 60 octaves from radio waves to high-energy gamma rays, the broadest spectrum known to arise from any single source. In general, the observed light curves consist either of a single, sharp pulse (Fig. A.4) or two closely spaced peaks (Fig. A.5) and the integrated pulse profiles – constructed from some hundreds or thousands of individual pulses – remain surprisingly consistent across all frequencies. Moreover, pulsar emission is highly linearly and circularly polarized, often with a sense change of circular polarization through the pulse. Linear polarization is usually dominant, however, very high degrees of circular polarization are occasionally observed (mean values are typically $20 - 30$ per cent, but can be as high as 100 per cent in individual pulses). The position angle of the radiation follows an S–shaped curve as a function of pulse longitude, often broken by one or more "jumps" (Figures A.4 and A.5, bottom panels).

Given these widely accepted findings, radio astronomer D. B. Melrose [99] postulated in 1996 that any model seeking to explain the mechanics of pulsar emission must account for the characteristic light curves, the enigmatic polarization properties, and the broad frequency spectrum. However, he conceded that "we cannot expect a theory of pulsar emission to be quantitative in the sense that the theory of synchrotron emission is quantitative" and that "our theories are likely to be useful

only in describing the most general features of pulsar emission – the 'climate' as opposed to the 'weather' " [99].

A.2 The Model

A.2.1 Introduction

In the four and a half decades since the discovery of the first pulsars, a plethora of disperse models has been employed to explain pulsar radiation processes and to identify their associated locations of emitting regions. An excellent summary of pulsar data and their interpretation is available [100]; yet even a brief perusal of this book will reveal that standard models of pulsar emission are fraught with problems.

The authors identify three sources of emission: The surface of the neutron star, the polar caps and the "outer magnetospheric gap." The latter is is a volume bounded by the "last closed field line" as defined by Julian and Goldreich and extends from the "neutral surface" to the velocity of light cylinder. (For a definition of the velocity of light cylinder, see Section 2.2.) Standard models assume three regimes under

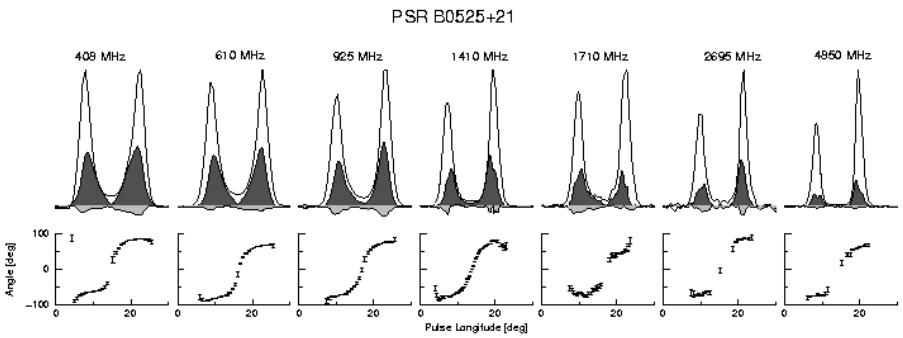

Figure A.5: Light curves, circular (light gray) and linear (dark gray) polarization, and polarization position angles at different frequencies for PSR B0525+21.

which pulsars radiate, namely, in order of increasing complexity: Thermal radiation from the surface, observed principally in the X-ray region of the frequency spectrum; beamed incoherent curvature radiation from high-energy electrons and positrons in the outer magnetospheric gaps; and beamed coherent radio emission from electrons and positrons located both in the outer gaps and above the magnetic poles. However, none of these mechanisms are able to account for more than a modest fraction of pulsar observations quantitatively.

The superluminal model of pulsar radiation, on the other hand, invokes a single emission mechanism operating across the entire frequency spectrum, namely emission by superluminal polarization currents. As has already been shown in Section 1.3, polarization P, defined as the dipole moment per unit volume, results from displacement of positive and negative charges in opposite directions. A *polarization current* occurs when a polarized region moves or changes with time t, hence the polarization current density is $\partial P/\partial t$ and has the same dimensions as a conventional current density of electrons. If a polarization current oscillates or accelerates, it will emit electromagnetic radiation, just as a current of electrons does. However, unlike electrons, which possess rest mass and are therefore limited to speeds less than c, the speed of light, polarization currents may travel arbitrarily fast, because the displacements of their constituent negative and positive particles are small; though the polarization currents travel faster than c, the particles' speeds remain subluminal. Albeit capable of moving faster than light, such a source distribution does not violate special relativity as it cannot be used to transmit a signal superluminally; the emitted radiation – as any other – travels *at* (or below) the speed of light. In Section 1.3.2 we compared this phenomenon to the "Mexican Wave," where slow, but carefully-timed movements of spectators send a rapidly-moving "wave" around a sports stadium. In the same section we showed that superluminal polarization currents have been created successfully in the laboratory. In experiments carried out in Russia, the United Kingdom and the USA, currents traveling at up to $12c$ have

been shown to emit tightly-focused pulses of radiation. Our ability to predict the results of these well-characterized, ground-based experiments gives us confidence in the use of the same models and techniques to treat pulsars.

The superluminal model of pulsar radiation assumes that a pulsar is a spinning neutron star with a strong, off-axis, magnetic field, B. This field will thus rotate through the pulsar's plasma atmosphere, at an instantaneous speed $v = \omega r$, where r is the perpendicular distance from the rotation axis and ω is the angular velocity [69]. A moving B will displace oppositely-charged particles in opposite directions, leading to a moving, electrically-polarized region, *i.e.* to a polarization current [69].

Though a similar assumption is a starting point for most pulsar models, such theories generally (i) constrain the emission to be within the light cylinder, at which the field's speed is the speed of light c, and (ii) consider only emission due to free currents of electrons. However, Maxwell's Equations show that the pulsar's distribution of fields and currents should rotate rigidly, so that for $r > c/\omega$, the distribution will be traveling faster than light [69]. For the reasons discussed above, such currents will be *polarization currents*. It is the emission from these faster-than-light polarization currents circling just outside the neutron star's light cylinder that is the basis of the present model.

Given that many emission processes are possible in a pulsar's atmosphere, it is natural to ask why superluminal emission dominates observations made from Earth. As has been shown exhaustively in Sections 2.3 through 4.3, this is due to a unique property of any source that both travels faster than the waves it emits and accelerates: Waves from several retarded times or even an extended period of source time can arrive instantaneously at a very distant point. As outlined in Section 1.2, such phenomena are well known in acoustics, *e.g.,* when a whip is cracked, a shot is fired from a gun or a high-performance aircraft accelerates through the sound barrier. In the aircraft's frame of reference, low energy sound is emitted over an extended period

of time, all of which arrives at a distant location instantaneously, creating a large and concentrated "boom."

Thus, a rotating superluminal source naturally produces very tightly-focused, intense pulses. More detailed studies show that the temporal focusing leads to the flux S of this particular component of the pulsar's emission falling off as $1/d$, rather than the usual $S \propto 1/d^2$ (see Section 2.3 and references therein), a prediction recently backed up by a statistical study of the Parkes Multibeam Survey [101, 102].[6] Hence, at large distances (*e.g.*, from Earth), this component of the emission will always dominate over other emission mechanisms whose flux falls off as $1/d^2$. Note that conservation of energy is not violated, as temporal focusing at this point is accompanied by dilation elsewhere (Section 2.3).

So, in spite of the certain presence of other emission mechanisms in pulsars, the efficient energy propagation of the wave packets emitted by superluminal polarization currents at, or close to, cusp conditions leads to their dominance in observations from Earth. The flux due to all other emission mechanisms falls off as $1/d^2$ (the inverse square law); the flux due to superluminal emission falls off more slowly. Hence, pulsar observations from Earth should be entirely explicable by superluminal processes. In the following sections, we compare the models outlined in Chapters 1 and 2 with observational data.

[6] The Parkes Multibeam (PM) Pulsar Survey uses a 20 cm multibeam receiver system and multibeam filter banks, digitizer and data-acquisition system to survey a region within $|b| < 5$ degrees in the inner Galactic plane for pulsars, many of which will be young and/or short-period. The PM Survey is specifically targeted for (i) obscured regions of the Galactic plane, (ii) young pulsars, and (iii) binary pulsars with massive companions. As of August 1999, analysis of about 50 per cent of the total expected data to be collected has resulted in the confirmed detection of over 400 new pulsars (an increase of more than 50 per cent of the known population).

A.2.2 Light Curve and Polarization

Single Pulse

The degree of temporal focusing (Figures 2.9 and 2.10) as well as the calculations of the Liénard-Wiechert fields (Fig. 4.1) of a rotating superluminal point charge show that an observer situated on the limiting cone of the cusp ($\theta_P = \theta_{P_C}$) will receive a very sharp pulse during each rotation of the source. For the astronomical scales on which both calculations are carried out, such a pulse has a width of $\leq$ 1ns and the periodicity of the pulse arrival is the same as that of the pulsar's rotation. Encouragingly, around 50 per cent of the pulsars in the Parkes data base (see footnote [1]) exhibit a single pulse, virtually all of the rest display double pulses, a phenomenon that we will explain in Section A.2.2. However, at first sight, there seems to arise a discrepancy in the pulse duration. Typical data suggest that the pulse width is at the order of milliseconds (see *e.g.,* Figure A.6 a)) and the data collected by J. Bell shown in Section A.1), much longer than the few nanoseconds predicted. However, this apparent width is almost certainly due to instrumental time resolution: In most telescopes, effective sensitivity is the most important consideration, and averaging of very many pulses is used to maximize this. [7] In other words, time resolution is sacrificed to sensitivity.

However, pulses from the Crab are sufficiently intense to permit high time resolution recordings of individual pulses (Fig. A.6 b) and c)). Once this is accomplished, structure on much shorter timescales reveals itself (Fig. A.6 a) and b)). Instrumental issues restrict the apparent widths to microseconds, but the observing team (T. Hankins, personal communication) believe that the true duration may be on a nanosecond timescale. Therefore, the short durations of the individual pulses are in accord with the model predictions from Chapter 2. From pulse to pulse, the tim-

[7] J. Middleditch and T. Hankins, numerous personal communications.

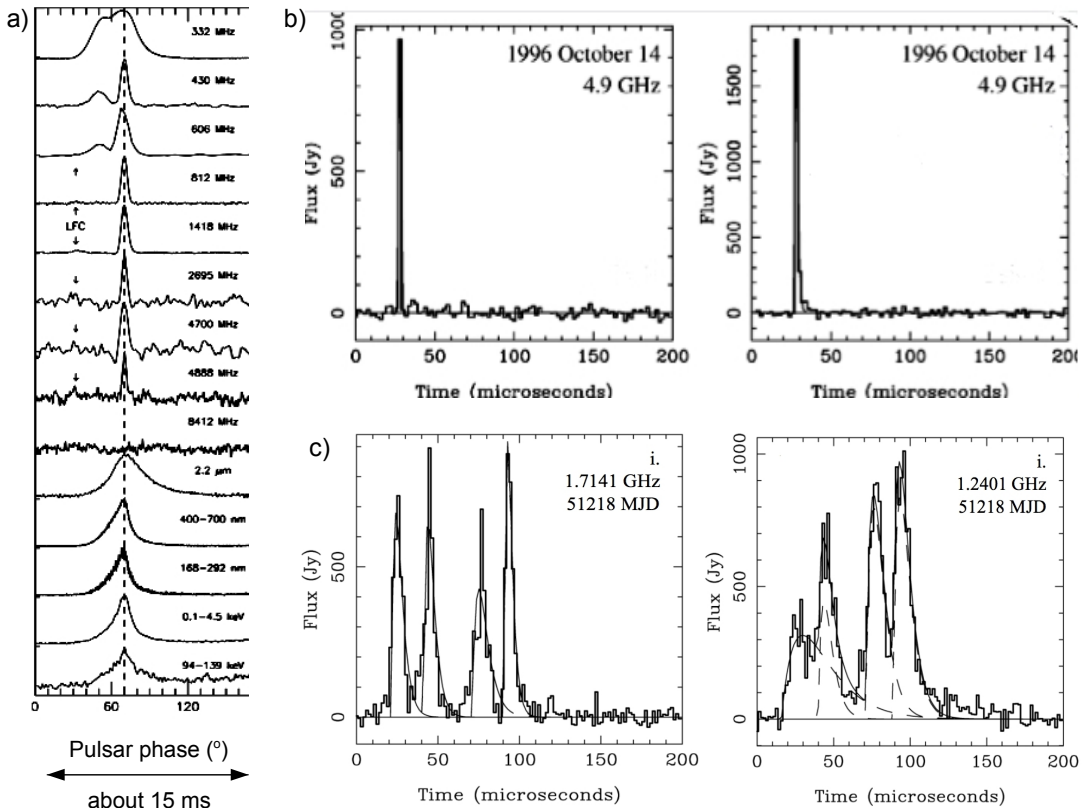

Figure A.6: a) Standard, time-averaged fluxes of the emission from the Crab pulsar, illustrating that the averaged pulse has a width in the milisecond range. b) and c) High time resolution data, showing individual pulses. The fine structure revealed is on timescales of microseconds.

ing and height of the sharp features (Fig. A.6 b) and c)) varies, eventually building up the broader, time-averaged pulses shown in Figure A.6 a). The latter are very predictable and regular, reflecting the stable rotation of the neutron star. The pulse-to-pulse variation, on the other hand, likely reflects the turbulence and atmospheric variations in the emitting plasma, the "weather," to speak with D. B. Melrose, and is likely to have a millisecond timescale.

Double Pulses and Polarization Structure

As the observer moves away from the cusp into the volume enclosed by the envelope of the emitted wave fronts such that $\theta_{P_C} < \theta_P < 180^\circ - \theta_{P_C}$, the single pulse experienced on the cusp gives way to a double-horned structure (Fig. 2.10), reflecting the underlying presence of three retarded contributions to the signal (Fig. 4.3). The intesities due to the three contributions have already been displayed in Figure 4.3; in Figure A.7, they are compared with pulsar observational data. Allowing for instrumental time resolution issues that will act to broaden features in the observational data, the agreement is very good.

Though a detailed examination of the frequency dependent spectrum predicted by the calculations of the radiation fields is a topic for future study (Chapter 5), the sharpness of the peaked structure (Figs. 2.10 and 4.3) will certainly lead to very broadband emission. The relative timing of the two pulses varies with observation angle, again accounting qualitatively for the double-peaked data in the Parkes Multibeam Survey [101]. A distinct feature of this mechanism will therefore be pulse timings that remain the same at all frequencies. This is in agreement with many observations; see, for instance, Figure A.5. The latter also allows for comparison of polarization properties; as was described in Section 4.3 and shown in Figure 4.1, results from the Liénard-Wiechert calculations for a generic charge in superluminal rotation can be expressed as Stokes parameters (Equation (4.26)), which are widely used in the analysis of astronomical data. Figures A.8 and A.9 illustrate such comparisons of Stokes parameters. As can be seen, the superluminal model accounts for the observational data very well, reproducing the light curve and swing in polarization position angle quantitatively. In particular, the polarization information extracted from 1404 MHZ observations of PSR B2016+28 by McKinnon [103] and shown in his Figure 1 (here Fig. A.9 (top)) is strikingly similar to our calculations (Figure A.9 (bottom)). The author notes some intriguing polarization properties

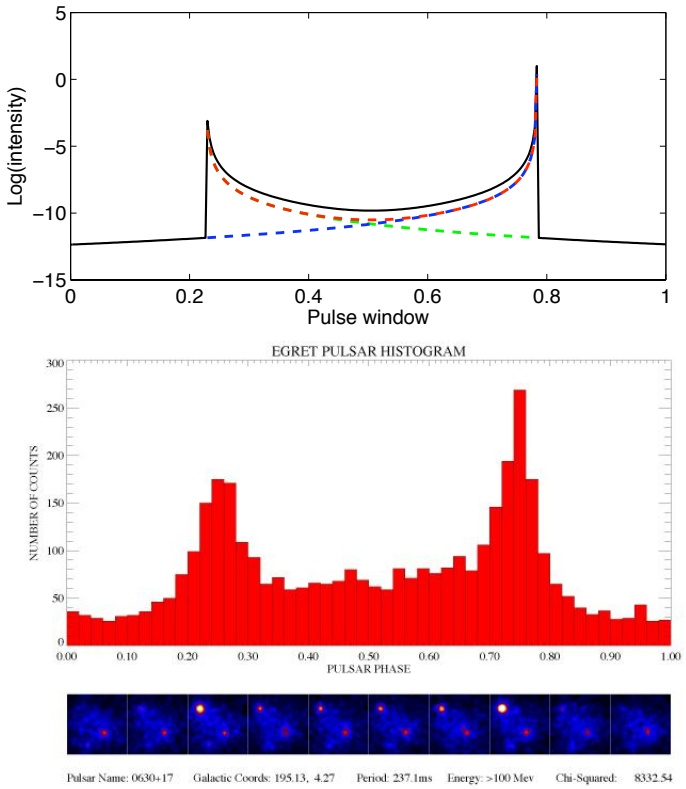

Figure A.7: Top: Calculated intensities of the contributions from the three retarded times (colour) and their resultant (black). Bottom: Observation of the gamma-ray intensity emanating from Geminga, related to the pulse phase, as detected by the EGRET instrument on the Compton Gamma Ray Observatory.

while all but conceding that standard models offer no explanation for the observed phenomena:

> Polarization observations of the radio emission from PSR B2016+28 at 1404 MHz reveal properties that are consistent with two, very different, interpretations of the pulsar's viewing geometry. The pulsar's average polarization properties show a rapid change in position angle (PA) near the pulse center, suggesting that the observer's sightline nearly intersects the star's magnetic pole. But single pulse, polarization observations of the pulsar show nearly orthogonal modes of polarization following relatively flat and parallel PA tra-

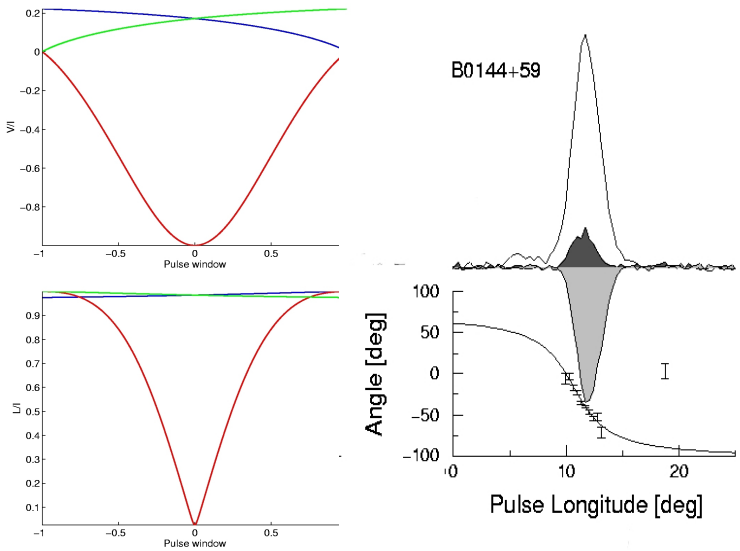

Figure A.8: Left: Stokes parameters, L (top) and V (bottom), from Liénard-Wiechert calculations described in Chapter 2. One of the three retarded times gives highly circularly polarized radiation and differs in its sense of polarization from the other two. Two of the modes have a very high degree of linear polarization. Right: Comparison with data. PSR B0144+59 has high right circular polarization (light gray) and moderate linear polarization (dark grey) in central portions of the pulse.

> jectories across the pulse, suggesting that the sightline is far from the pole. Additionally, PA histograms reveal a "modal connecting bridge," of unknown origin, joining the modal PA trajectories over much of the pulse and following the rapid PA change shown in the average data.

We note that the swing in position angle and the near orhogonality of the two polarization modes are entirely consistent with a superluminal source, which does not require a particular viewing angle with respect to the star's magnetic pole. Furthermore, we submit that the "modal connecting bridge of unknown origin" may well be the signal of the second of three contributing times of a superluminal source.

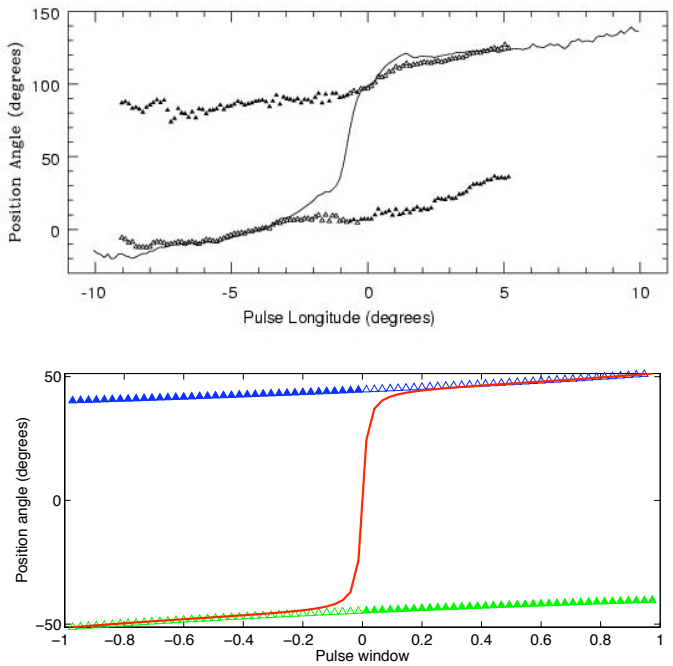

Figure A.9: Top: Data: Position angle histogramm of PSR 2016+28 at 1404MHz. Note the presence of the "mystery third component" bridging the middle of the pulse. Bottom: The three retarded times reproduce all of the features of the observational data, including the 90^o swing.

The Interpulse

Section A.2.2 describes how the superluminal model can reproduce the two-horned pulse structure observed in the emission of many pulsars. However, some pulsars emit an "interpulse," which is widely separated in time from the main pulse (by about half a rotational period). A detailed discussion of the interpulse is beyond the scope of this thesis. However, it is believed that the main and interpulses represent superluminal emission by two distinct regions of the pulsar's "atmosphere." This conclusion is suported by recent analysis of the Crab pulsar [104–107].

A.2.3 Spectral Features

The author of this thesis is involved in a project to fit broadband pulsar observations to the expected emission spectrum of a rotating superluminal source, and so a brief description is included here for completeness. As pointed out in Chapter 4.1, the emission of a small superluminal volume element is in many ways analogous to synchrotron radiation. In the latter, a highly relativistic single electron, or a highly relativistic compact bunch of electrons, emits radiation as it undergoes centripetal acceleration. The frequency spectrum of the radiation is, in essence, the Fourier transform of the electric field of the electron(s) as they pass the observer. Given that the source is both fast and compact, the time-dependent electric field is very sharply peaked: Hence the corresponding emission is very broadband and rather featureless. The rôle of the electron's electric field is fulfilled by the sharply-peaked electric field of the cusp radiation (see Figures 2.9 and 2.10) in the superluminal model. However, since the source itself is superluminal, the Lorentz factor $1/\sqrt{1-v^2/c^2}$ is imaginary (see Chapter 4.1). This has the effect of rendering exponential terms in the synchrotron radiation *formulae* oscillatory; in contrast to conventional synchrotron radiation with its smooth spectrum, the point-like superluminal source has an emission spectrum that oscillates as a function of frequency. The radiation spectrum is given by the following set of equations (for a complete mathematical treatment, see [69, 108]) in which $n = \frac{2\pi f}{\omega}$, and Ai and Ai$'$

Figure A.10: The Swiss Light Source (SLS) at the Paul Scherrer Institut is a third-generation synchrotron light source. With an energy of 2.4GeV, it provides photon beams of high brightness for research in materials science, biology and chemistry. .

are the Airy function and its derivative, respectively:

$$\begin{aligned}\frac{\mathrm{d}P_n}{\mathrm{d}\Omega_P} \;\propto\; & S_1(n)^2 \mathrm{Ai}^2\left[-\left(\frac{2}{n}\right)^{1/3}\frac{\Omega}{\omega}\right] \\ & + S_2(n)^2\left(\frac{2}{n}\right)^{2/3}\mathrm{Ai}'^2\left[-\left(\frac{2}{n}\right)^{1/3}\frac{\Omega}{\omega}\right] \\ & + 2S_3(n)^2\left(\frac{2}{n}\right)^{1/3}\mathrm{Ai}\left[-\left(\frac{2}{n}\right)^{1/3}\frac{\Omega}{\omega}\right] \\ & \times \mathrm{Ai}'\left[-\left(\frac{2}{n}\right)^{1/3}\frac{\Omega}{\omega}\right], \end{aligned} \tag{A.3}$$

in which

$$S_1(n) = n^{2/3}|K_r|K_{\varphi_0}\left(|\bar{s}_r|^2 + |\bar{s}_\varphi\cos\theta_P - \bar{s}_z\sin\theta_P|^2\right)^{1/2},$$

$$S_2(n) = n^{2/3}|K_r|K_{\varphi_0}\left(|\bar{s}_\varphi|^2 + |\bar{s}_r|^2\cos^2\theta_P\right)^{1/2},$$

and

$$\begin{aligned} S_3(n) \;=\; & n^{2/3}|K_r|K_{\varphi_0} \\ & \times\left\{\Im\left[\bar{s}_r^*\cos\theta_P\left(\bar{s}_\varphi\cos\theta_P - \bar{s}_z\sin\theta_P\right) - \bar{s}_r\bar{s}_\varphi^*\right]\right\}^{1/2}. \end{aligned}$$

Here, $\bar{s}_{r,\varphi,z}$ are the Fourier components of the source densities $s_{r,\varphi,z}|_{\hat{r}=\csc\theta_P}$ with respect to z, $\Im$ and the superscript star denote the imaginary part and the conjugate of a complex variable, respectively, and $(R_P, \theta_P, \varphi_P)$ are the spherical polar coordinates of the observation point P. The function K_{φ_0} is defined by

$$K_{\varphi_0} = (-1)^{n+m}\sin\left(\frac{\pi\Omega}{\omega}\right)\left(\frac{\mu_+}{n-\mu_+} + \frac{\mu_-}{n-\mu_-}\right), \tag{A.4}$$

where

$$\mu_+ = \left|\frac{\Omega+\omega}{\omega}\right| \quad \text{and} \quad \mu_- = \left|\frac{\Omega-\omega}{\omega}\right|. \tag{A.5}$$

Though Equation (A.3) appears complicated, the following points should be noted:

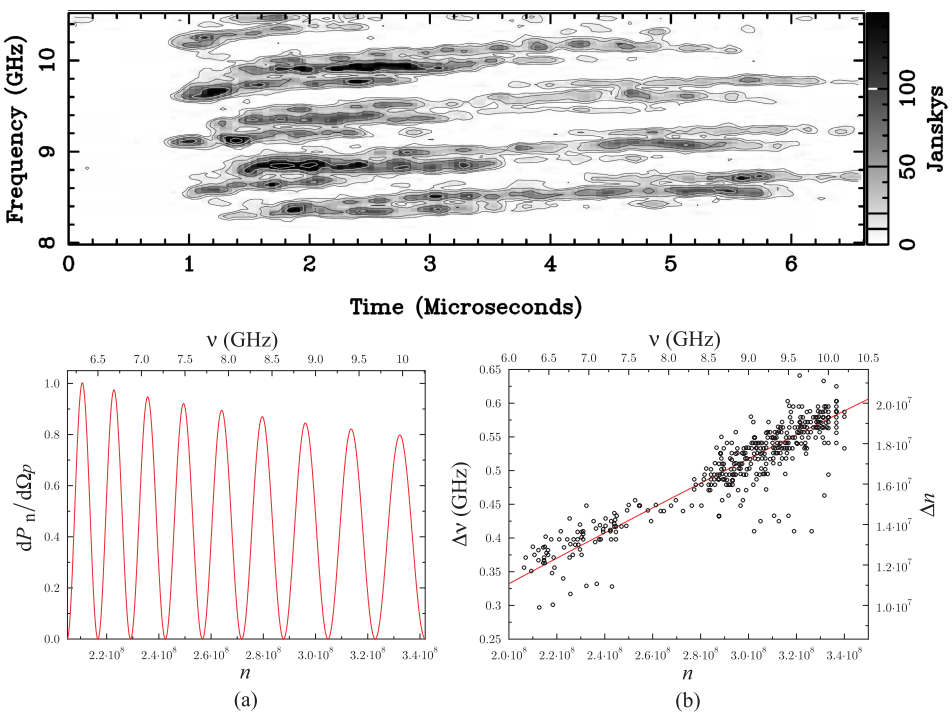

Figure A.11: Top: Superluminal emission is, analogous to that of synchrotrons, very broadband, but the Lorentz factor γ is imaginary. Hence, the intensity oscillates as a function of frequency. These oscillations are observed in Crab interpulses. Bottom: Predictions (left) fit observations (right) very well. The predicted oscillations of the spectrum of the emission for $\omega/(2\pi) = 30.3$ Hz and $\Omega/\omega \simeq 1.9 \times 10^4$, shown in (a), have the same spacing as those of the emission bands in the observed spectrum of the Crab pulsar.

1. The function is generic; it should apply to all rotating faster-than-light sources. Therefore the frequency-dependent emission of *all* pulsars should have a qualitatively similar form.

2. Whilst details of the spectrum can be adjusted by varying the relative sizes of S_1, S_2, and S_3, the overall appearance of the spectrum is determined by just two adjustable parameters, ω (the angular velocity of the source) and Ω, a frequency at which the pulsar's atmosphere responds resonantly to electromagnetic disturbances. This is thought to correspond to the plasma frequency of the free electrons, $\omega_P = \left(\frac{Ne^2}{\epsilon_0 m_e}\right)^{1/2}$, where N is the number density of electrons,

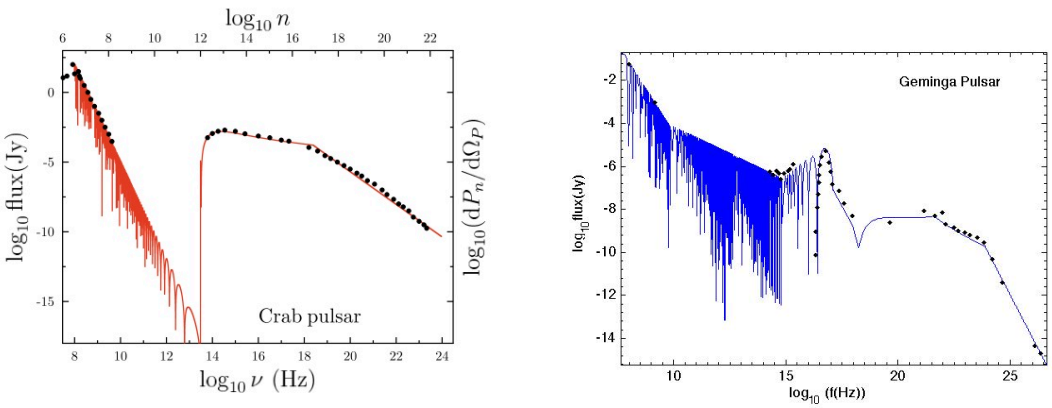

Figure A.12: Left: The points show observational data (where available) on the spectrum of the Crab pulsar. The curves show the spectral distribution $\log(\mathrm{d}P_n/\mathrm{d}\Omega_P)$, predicted by equation (A.3), versus $\log n$ and $\log \nu$ for $\nu = n\omega/(2\pi) \simeq 30.3n$ Hz and $\Omega/\omega \simeq 1.9 \times 10^4$. In the model, the recovery of intensity at the ultraviolet peak ($\sim 10^{15}$ Hz) is caused by resonant enhancement due to the azimuthal modulation frequency $m\omega/(2\pi) \simeq 3 \times 10^{13}$ Hz. The steepening of the gradient of the spectrum by -1 at 2.4×10^{18} Hz reflects a transition through the Rayleigh distance. Right: A similar fit for the Geminga pulsar. The overall characteristics of pulsar emission are determined by the *superluminal nature* of the source: Only the *details* depend on the pulsar "atmosphere", *i.e.,* its relative permittivity. One further parameter, namely the electron cyclotron frequency, is used to fit the peak at higher ν.

e the electron charge and m_e denotes the electron mass.

3. If there are subsequent, higher frequency, resonances in the plasma atmosphere, the emission will be enhanced at those frequencies. The only notable resonance expected for a pulsar's atmosphere would be the electron cyclotron frequency, $\omega_c = \frac{eB}{m_e}$, where B is the magnetic field in the emitting region of the atmosphere.

Typical fits are shown in Figures A.11 and A.12. From such models, the electron density and magnetic field at the emitting region can be deduced: Thus far, this has been done for 12 pulsars [69, 108]. The values deduced are in accord with the expectations for neutron stars and their atmospheres.

More recently, we employed the calculations outlined above to fit pulsed gamma-

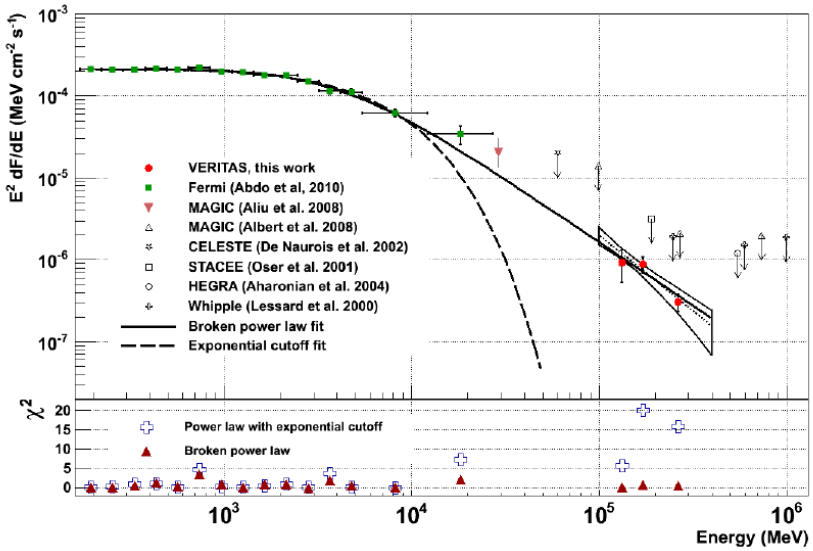

Figure A.13: Spectral energy distribution (SED) of the Crab pulsar in gamma rays. VERITAS flux measurements are shown by the solid red circles, Fermi-LAT data by green squares, and the MAGIC flux point by the solid triangle. The empty symbols are upper limits from CELESTE, HEGRA, MAGIC, STACEE, and Whipple. The bowtie and the enclosed dotted line give the statistical uncertainties and the best-fit power-law spectrum for the VERITAS data using a forward-folding method. The result of a fit of the VERITAS and Fermi-LAT data with a broken power law is given by the solid line and the result of a fit with a power-law spectrum multiplied with an exponential cutoff is given by the dashed line.

rays from the Crab pulsar at energies above 100GeV, detected by the VERITAS array of atmospheric Cherenkov telescopes [109]. The authors of [109] note that "the detection cannot be explained on the basis of present pulsar models," and conclude that the photon spectrum of pulsed emission between 100MeV and 400GeV is best described by a broken power law Figure A.13.

As Fig. A.14 shows, the superluminal model yields a comparable goodness of fit for the high-energy data observed by FERMI and VERITAS, while, at the same time, accounting for the *entire* frequency spectrum of the Crab pulsar, covering more than 9 orders of magnitude.

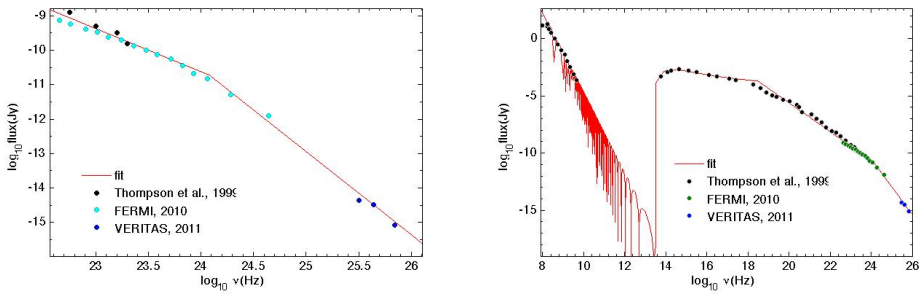

Figure A.14: Left: Fit of the superluminal model to the same FERMI and VERITAS observations as shown in Fig. A.13. Right: The superluminal model not only yields a comparable goodness of fit for the high-energy data observed, but accounts for the *entire* frequency spectrum of the Crab pulsar, covering more than 9 orders of magnitude.

Other Features

It will be clear from the previous sections that the electromagnetic emission of a small superluminal source in a circular orbit is extremely broadband (*i.e.,* it spans a very wide frequency range), and indeed, many pulsars are observed to emit from the radio frequencies to the X or gamma ray regions. (This has, in the past, led to some unusual deductions. If one assumes, for example, that the pulsar emission is thermal, then an inordinately high apparent brightness temperature results.) Moreover, the pulses themselves appear to be coherent. The latter behaviour can be understood in terms of the cusp, which results from the part of the source that approaches the observer at the speed of light and no acceleration. Consequently, all of the phase information from this part of the source will collapse onto a single arrival time, making the source appear coherent. This apparent coherence has been demonstrated in ground-based experiments.

Once one accepts that the emission from superluminal polarization currents dominates pulsar observations from Earth, the superluminal model of pulsar emission explains all the following data [108]: (i) the flux-distance relationship derived from the Parkes Multibeam Survey; (ii) the enigmatic polarization properties (*e.g.* swing

in position angle); (iii) the apparent radiation temperature and pulse shape; (iv) the oscillatory intensity seen in the Crab pulsar at around 10GHz; and (v) the broad-band radiation spectrum, covering 16-18 orders of magnitude of frequency. The latter point (*i.e.,* a single model fitting the entire broadband spectrum) shows the great advantage of the the present model; though we can show that, *e.g.,* the "slot gap" or "outer gap" models give comparable quality fits to parts of the data, *they are only applicable to a small frequency window*, and so a plethora of other (unrelated) phenomena must be invoked to cover the entire spectral range.

References

[1] B. M. Bolotovskii, A. V. Serov, *Radiation of superluminal sources in vacuum*, Radiation Physics and Chemistry, 2006, 75:813–24.

[2] Daniel Savitsky, *On the subject of high-speed monohulls*, presented to the Greek Section of the Society of Naval Architects and Marine Engineers, Athens, Greece, October 2, 2003.

[3] Homer, *The Iliad with an English Translation by A. T. Murray, Ph.D. in two volumes*, Harvard University Press, Cambridge, MA, William Heinemann, Ltd., London, 1924, I, 477 ff.

[4] Lionel Casson, *Ships and Seamanship in the Ancient World*, Johns Hopkins University Press, Baltimore, ML, 1995.

[5] Homer, *The Odyssey of Homer. Translated by George Herbert Palmer*, The Riverside Press, Cambridge, MA, XIII, 70 ff.

[6] Ernst Mach, *Über Erscheinungen an fliegenden Projektilen*, Populärwissenschaftliche Vorlesungen, 5. Auflage, Leipzig, 1923, pp. 351–77 (German).

[7] W. Gerhard Pohl, *Peter Salcher und Ernst Mach. Schlierenfotografie von Überschall-Projektilen*, Plus Lucis, 2/2002–1/2003, pp. 22–6 (German).

[8] Wolfgang F. Merzkirch, *Mach's Contribution to the Development of Gas Dynamics*, Ernst Mach: Physicist and Philosopher. Edited by R. S. Cohen and Raymond J. Seeger, Boston Studies in the Philosophy of Science, D. Reidel Publishing Company, Dodrecht, Holland, 2010, pp. 42–59.

[9] H. Reichenbach, *Contributions of Ernst Mach to Fluid Dynamics*, Ann. Rev. Fluid Mech., 1983, 15:1-28.

[10] G. M. Lilley, R. Westley, A. H. Yates and J. R. Busing, *The supersonic Bang*, Nature, 1953, 171:994–7.

[11] Albert Einstein, *Zur Elektrodynamik bewegter Körper*, Annalen der Physik, 1905, 17:891–921 (German).

[12] Oliver Heaviside, *Electrical Papers,* first edition, Macmillan and Co., New York and London, 1894.

[13] A. Sommerfeld, *Zur Elektronentheorie (3 Teile)*, Nach. Kgl. Ges. Wiss. Göttingen, Math. Naturwiss. Klasse, 1904, 99–130, 363–439, 1905, 201–35 (German).

[14] B. M. Bolotovskii and V. L. Ginzburg, *The Vavilov-Čerenkov effect and the Doppler effect in the motion of sources with superluminal velocity in vacuum*, SOVPU, 1972, 15:184–92.

[15] Emilio Segrè, *Nuclei and Particles*, second edition, W. A. Benjamin, Inc., Reading, MA, 1977.

[16] *Nobel Lectures, Physics 1942-1962*, Elsevier Publishing Company, Amsterdam, 1964.

[17] A. Ardavan, W. Hayes, J. Singleton, H. Ardavan, J. Fopma, D. Halliday, *Experimental observation of nonspherically-decaying radiation from a rotating superluminal source*, JAPPLPHYS, 2004, 96:7760–77(E). (Corrected version of 96:4614–31.)

[18] J. Singleton, A. Ardavan, H. Ardavan, J. Fopma, D. Halliday, W. Hayes, *Experimental demonstration of emission from a superluminal polarization current – A new class of solid-state source for MHz-THz and beyond*, Digest of the 2004 Joint 29th International Conference on Infrared and Millimeter Waves and 12th International Conference on Terahertz Electronics, IEEE, 2004.

[19] Tom Wolfe, *The right stuff*, Farar, Straus and Giroux, 1979, reissued by Picador, 2008.

[20] Al Blackburn, *Mach Match*, Air and Space Magazine, January 01, 1999.

[21] *Death at Farnborough*, Time Magazine, September 15, 1952.

[22] *The Farnborough tragedy*, Flight Magazine, September 1952.

[23] T. Gold, Nature, 1952,170:808.

[24] P. Rothwell, Nature, 1953,171:215–6.

[25] Theodore von Kàrmàn *Aerodynamics: selected topics in the light of their historical development*, Dover Publications, Inc., Mineola, NY, 2004, originally published by Cornell University Press, Ithaca, NY, 1954.

[26] J. Ackeret, *Akustische Phänomene bei hohen Fluggeschwindigkeiten*, Neue Zürcher Zeitung, September 18, 1952 (German).

[27] M. Roy, *A propos du gong sonique*, Comptes rendus de l' Académie des Sciences, Paris, 1952, 235:756–9 (French).

[28] *Concorde: You asked a pilot. Concorde pilot Peter Benn answered your questions*, transcript of a BBC News interview, October 24, 2003.

[29] V. L. Ginzburg, *Vavilov-Čerenkov effect and anomalous Doppler effect in a medium in which wave phase velocity exceeds velocity of light in vacuum*, SOVP-JETP, 1972, 35:92–3.

[30] Lokenath Debnath, *Nonlinear partial differential equations for scientists and engineers*, Birkhäuser, Boston, MA, 2005.

[31] H. Ardavan, A. Ardavan, J. Singleton, J. Fasel, A. Schmidt, *Morphology of the nonspherically decaying radiation field generated by a rotating superluminal source*, JOSAA, 2007, 24:2443–56.

[32] H. Ardavan, A, Ardavan, J. Singleton, *Spectral and polarization characteristics of the nonspherically decaying radiation generated by polarization currents with superluminally rotating distribution patterns: reply to comment*, JOSAA, 2006, 23:1535–39.

[33] J. D. Jackson, *Classical Electrodynamics*, third edition, John Wiley & Sons, New York, 1999.

[34] I. Farkas, D. Helbing, T. Vicsek, *Social behaviour: Mexican waves in an excitable medium - The stimulation of this concerted motion among expectant spectators is explained*, Nature, 2002,419:131–2.

[35] J. Singleton *et al.*, *Eighteen-month report on LDRD 20080085 DR: Construction and use of superluminal emission technology demonstrators with applications in radar, astrophysics, and secure communications*, 2009.

[36] J. Singleton, A. Schmidt, J. Wigger, *Tests of the Linear Superluminal Antenna done for and in collaboration with CommScope*, 2012.

[37] B. M. Bolotovskii, A. V. Serov, *Radiation of superluminal sources in empty space*, Phys. Usp., 2005, 48:903–15.

[38] A. V. Bessarab, A. A. Gorbunov, S. P. Martynenko, N. A. Prudkoi, *Faster-than-light EMP source initiated by short X-ray pulse of laser plasma.* IEEE Trans. Plasma Sci., 2004, 32:1400–03.

[39] A. V. Bessarab, S. P. Martynenko, N. A. Prudkoi, A. V. Soldatov, V. A. Terenkhin, *Experimental study of electromagnetic radiation from a faster-than-light vacuum macroscopic source*, Radiation Physics and Chemistry, 2006, 75:825-31.

[40] Yu. N. Lazarev, P. V. Petrov, *A high-gradient accelerator based on a faster-than-light radiation source*, Technical Physics, 2000, 45:971–9.

[41] J. H. Hannay, *Bounds on fields from fast rotating sources, and others*, Proc. R. Soc. London, 1996, Ser. A, 452:2351–4.

[42] J. H. Hannay, *Comment II on 'Generation of focused, nonspherically decaying pulses of electromagnetic radiation'*, Phys. Rev. E, 2000, 62:3008–9.

[43] J. H. Hannay, *Comment on 'Method of handling the divergences in the radiation theory of sources that move faster than their waves'*, J. Math. Phys., 2001, 42:3973–4.

[44] J. H. Hannay, *Spectral and polarization characteristics of the nonspherically decaying radiation generated by polarization currents with superluminally rotating distribution patterns: comment*, J. Opt. Soc. Am. A, 2006, **23**, 1530–4.

[45] J. H. Hannay, *Morphology of the nonspherically decaying radiation generated by a rotating superluminal source: comment*, J. Opt. Soc. Am. A, 2008, 25:2165–6.

[46] H. Ardavan, *Reply to comments on 'Generation of focused, nonspherically decaying pulses of electromagnetic radiation'*, Phys. Rev. E, 2000, 62:3010–13.

[47] H. Ardavan, A. Ardavan, J. Singleton, J. Fasel, and A. Schmidt, *Spectral and polarization characteristics of the nonspherically decaying radiation generated by polarization currents with superluminally rotating distribution patterns: reply to comment*, J. Opt. Soc. Am. A, 2006, 23:1536–9.

[48] H. Ardavan, A. Ardavan, J. Singleton, J. Fasel, and A. Schmidt, *Morphology of the nonspherically decaying radiation field generated by a rotating superluminal source: reply to comment*, J. Opt. Soc. Am. A, 2008, 25:2167–9.

[49] H. Ardavan, A. Ardavan, J. Singleton, J. Fasel, and A. Schmidt, *Response to "Comment on 'Methods of handling the divergences in the radiation theory of sources that move faster than their own waves', "* 2008, ArXiv:0805.0304v1 [math-ph].

[50] Edwin Cartlidge, *Money spinner or loopy idea?* Science, 2003, 301:1463-5.

[51] M. Durrani, *Revolutionary device polarizes opinions*, Physics World, August 2001.

[52] *Lawbreakers?* The Economist, August 17, 2000.

[53] G. A. Schott, *Electromagnetic radiation and the mechanical reactions arising from it*, Cambridge University Press, 1912.

[54] A. Schmidt, H. Ardavan, J. Fasel, J. Singleton, and A. Ardavan, *Occurrence of concurrent 'orthogonal' polarization modes in the Liénard-Wiechert field of a rotating superluminal source*, in W. Becker and H. H. Huang, eds., MPE Report 291, Proc. 363rd WE-Heraeus Seminar on Neutron Stars and Pulsars, 2007, 124–127.

[55] H. Ardavan, A. Ardavan, J. Singleton, J. Fasel, and A. Schmidt, *Spectral and polarization characteristics of the nonspherically decaying radiation generated by polarization currents with superluminally rotating distribution patterns*, JOSAA, 2004, 21:858–872.

[56] H. Ardavan, A. Ardavan, J. Singleton, J. Fasel, and Andrea Schmidt, *Fundamental role of the retarded potential in the electrodynamics of superluminal sources*, 2008, J. Opt. Soc. Am. A, 25:543–57.

[57] H. Ardavan, A. Ardavan, J. Singleton, J. Fasel, A. Schmidt, *Inadequacies in the conventional treatment of the radiation field of moving sources*, J. Math. Phys., 2009, 50:103510.

[58] H. Ardavan, *Generation of focused, nonspherically decaying pulses of electromagnetic radiation*, Phys. Rev. E, 1998, 58:6659–684.

[59] I. N. Bronshtein, K. A. Semendyayev, *Taschenbuch der Mathematik*, 3. Auflage, Springer Verlag, Berlin, Heidelberg, 1997. (German)

[60] P. M. Morse and H. Feshbach, *Methods of Theoretical Physics*, McGraw-Hill, New York, 1953, Pt. I.

[61] L.C. Evans, *Partial differential equations*, American Mathematical Society, Providence, 1998.

[62] I. Stakgold, *Boundary Value Problems of Mathematical Physics*, SIAM, Philadelphia, 2000, Volume I.

[63] I. Stakgold, *Boundary Value Problems of Mathematical Physics*, SIAM, Philadelphia, 2000, Volume II.

[64] I. Stakgold, M. Holst, *Green's Functions and Boundary Value Problems* John Wiley & Sons, New York, 2011.

[65] A. Ardavan, H. Ardavan, *Apparatus for generating electromagnetic radiation*, International patent application, PCT-GB99-02943 (September 6, 1999).

[66] J. Singleton *et al.*, *Apparatus and method for phase fronts based on superluminal polarization current*, United States patent application, US 20100039324A1 (February 18, 2010).

[67] F. Burk, *Lebesgue Measure and Integration*, Wiley, New York, 1997.

[68] P. J. Duke, *Synchrotron Radiation*, Oxford Series on Synchrotron Radiation, Oxford University Press, Oxford, 2000.

[69] H. Ardavan, A. Ardavan, J. Singleton, and M. Perez, *Mechanism of generation of the emission bands in the dynamic spectrum of the Crab pulsar*, MNRAS, 2008, 388:873–883.

[70] P. Colwell, *Solving Kepler's Equation over Three Centuries*, Willmann-Bell, Richmond, VA, 1993.

[71] E. Burniston and C. Siewert, *The use of Riemann problems in solving a class of transcendental equations*, Proceedings of the Cambridge Philosophical Society, 1973, 73:111–8.

[72] N. I. Ioakimidis and K. Papadakis, *A new simple method for the analytical solution of Kepler's equation*, Celestial Mechanics, 1985, 35:305–16.

[73] L. Delves and J. Lyness, *A numerical method for locating the zeros of an analytic function*, Mathematics of Computation, 1967, 21:543–77.

[74] W. Gautschi, *Numerical analysis: an introduction*, Birkhäuser, Basel, 1997.

[75] E. Süli and D. Mayers, *An Introduction to Numerical Analysis*, Cambridge University Press, Cambridge, UK, 2003.

[76] F. B. Hildebrand, *Introduction to numerical analysis*, Dover Publications, Mineola, N. Y., 1956.

[77] C. M. Bender, S. A. Orszag, *Advanced Mathematical Methods for Scientists and Engineers*, McGraw-Hill, New York, 1978.

[78] W. H. Press, B. P. Flannery, S. A. Teukolsky, W. T. Vetterling, *Numerical Recipes in Fortran 77: The Art of Scientific Computing*, Cambridge University Press, Cambridge, UK, 1986.

[79] F.G. Friedlander, M. Joshi, *Introduction to the Theory of Distributions*, 2nd edition, Cambridge University Press, Cambridge, 1998.

[80] H. Triebel, *Hoehere Analysis*, VEB Deutscher Verlag der Wissenschaften, Berlin, 1972.

[81] S. Chandrasekhar, *Radiative Transfer*, Dover, NewYork, 1960.

[82] D. R. Lorimer and M. Kramer, *Handbook of Pulsar Astronomy*, Cambridge University Press, Cambridge, UK, 2005.

[83] A. P. French, *Special Relativity*, The M.I.T. Introductory Physics Series, Thomas Nelson and Sons, London, 1968.

[84] H. Ardavan, *Method of handling the divergences in the radiation theory of sources that move faster than their waves*, J. Math. Phys. **40**, 1999, 4331–6.

[85] H. Ardavan, A. Ardavan, J. Singleton, *Frequency spectrum of focused broadband pulses of electromagnetic radiation generated by polarization currents with superluminally rotating distribution patterns*, J. Opt. Soc. Am. A **20**, 2003, 2137–55.

[86] A. Słowikowska, A. Jessner, B. Klein, G. Kanbach, *Optical polarisation of the Crab pulsar: precision measurements and comparison to the radio emission*, 2005, ArXiv:astro-ph/0511599v2.

[87] G. Efstathiou, R. S. Ellis, and B. A. Peterson, *Analysis of a complete galaxy redshift survey – II the field-galaxy luminosity function*, 1988, Mon. Not. R. Astr. Soc., 232:431–61.

[88] A. Hewish, S. J. Bell, J. D. H. Pilkington, P. F. Scott, R. A. Collins, *Observation of a rapidly pulsating radio source*, Nature, 1968, 217:709–713.

[89] F. Pacini, *Energy emission from a neutron star*, Nature, 1967, 216:567–68.

[90] F. Pacini, *Rotating neutron stars, pulsars and supernova remnants*, Nature, 1968, 219:145–46.

[91] T. Gold, *Rotating neutron stars as the origin of the pulsating radio sources*, Nature, 1968, 218:731–32.

[92] T. Gold, *Rotating neutron stars and the nature of pulsars*, Nature, 1969, 221:25–27.

[93] W. Baade, F. Zwicky, F., *On super-novae*, Proc. Nat. Acad. Sci., 1934, 20:254–59.

[94] D. W. Richards, J. M. Comella, *The period of pulsar NP 0532*, Nature, 1969, 222:551–52.

[95] P. Goldreich, W. H. Julian, *Pulsar electrodynamics*, Ap. J.,1969,157:869–880.

[96] W. J. Cocke, M. J. Disney, D. J. Taylor, *Discovery of optical signals from pulsar NP 0532*, Nature, 1969, 221:525–27.

[97] G. Fritz, R. C. Henry, J. F. Meekins, T. A. Chubb, H. Friedmann, *X-ray pulsar in the Crab nebula*, Science, 1969, 164:709–712.

[98] H. Bradt, S. Rappaport, W. Mayer, R. E. Nather, B. Warner, M. Mcfarlane, J. Kristian, *X-ray and optical observations of the pulsar NP 0532 in the Crab nebula*, Nature, 1969, 222:728–730.

[99] D. B. Melrose, *Whence the pulses? Pulsars: Problems and Progress*, ASP Conference Series, 1996, 105:139–146.

[100] A. G. Lyne, F. Graham-Smith, *Pulsar Astronomy*, Cambridge University Press, Cambridge, 2006.

[101] J. Singleton, P. Sengupta, J. Middleditch, T. L. Graves, M. R. Perez, H. Ardavan, A. Ardavan, *Violation of the inverse square law by the observed flux-distance relationship for pulsars*, Nature Magazine (London), submitted (2009).

[102] A. Schmidt, J. Singleton, P. Sengupta, J. Middleditch, T. L. Graves, H. Ardavan, A. Ardavan, *Violation of the inverse square law by pulsars in the Parkes Multibeam Survey*, 2012, in preparation, also presented at the 119th Meeting of the AAS in Austin, TX.

[103] M. M. McKinnon, *The transition between nonorthogonal polarization modes in PSR B2016+28 at 1404 MHz*, ApJ, 2003, 590:1026–034.

[104] S. C. Lundgren, J. M. Cordes, M. Ulmer, R. Foster, T. H. Hankins, *Giant pulses from the Crab pulsar: A joint radio and gamma-ray study*, The Astrophysical Journal, 1995, 453:433–55.

[105] T. H. Hankins, J. S. Kern, J. C.Weatherall, and J. A. Eilek, *Nanosecond radio bursts from Strong Plasma Tuburlence in the Crab Pulsar*, Nature, 2003, 422:141.

[106] J. A. Eilek, T. H. Hankins, *What makes the Crab pulsar shine?*, 2007, ArXiv:0710.1891v1 [astro-ph].

[107] T. H. Hankins, J. A. Eilek, *Radio Emission Signatures in the Crab Pulsar*, 2007, ArXiv:astro-ph/0701252v1.

[108] H. Ardavan, A. Ardavan, J. Singleton, J. Fasel, W. Junor, J. Middleditch, M. R. Perez, A. Schmidt, P. Sengupta, P. Volegov, *Comparison of multiwavelength observations of 9 broad-band pulsars with the spectrum from an extended current with a superluminally rotating distribution*, 2009, ArXiv:0908.1349v1 [astro-ph].

[109] The VERITAS Collaboration, *Detection of Pulsed Gamma Rays Above 100 GeV from the Crab Pulsar*, Science, 2011, 334:69–72.

[110] A. Ardavan, H. Ardavan, J. Fasel, J. Middleditch, M. R. Perez, A. Schmidt, J. Singleton, *A new mechanism for generating pulsar-like polarization*, in proceedings of *Polarimetry days in Rome: Crab status, theory and prospects*, 2009, Proceedings of Science (CRAB2008)016, `http://pos.sissa.it`.